Aus dem Institut für Strahlenmedizin

Helmholtz Zentrum München

Direktor: Prof. Dr. med. Dr. h.c. Matthias H. Tschöp

Retrospective dosimetry with luminescence measurements on personal items for unplanned exposures

Dissertation
zum Erwerb des Doktorgrades der Naturwissenschaften

an der Medizinischen Fakultät der

Ludwig-Maximilians-Universität München

vorgelegt von

Alessia Mafodda

aus

Catania

Jahr

2021

Mit Genehmigung der Medizinischen Fakultät
der Universität München

Betreuer:	Prof. Dr. Werner Rühm
Zweitgutachter(in):	Prof. Dr. Olaf Dietrich
Dekan:	Prof. Dr. med. Thomas Gudermann
Tag der mündlichen Prüfung:	27.Juni 2022

Table of content

Zusammenfassung

Das Risiko einer unfallbedingten Strahlenexposition besteht sowohl bei kleinskaligen Unfällen, die zum Beispiel in Industrie, Technik und Medizin beim beruflichen Umgang mit Strahlenquellen passieren können, als auch bei großskaligen radiologischen Notfällen, wie sie bei schweren Unfällen in einer kerntechnischen Anlage oder gezielten terroristischen Anschlägen mit radioaktiven Materialien auftreten können. Besonders für die zuletzt genannte Art von Notfällen ist eine adäquate Maßnahmenstrategie notwendig, um Entscheidungsträger von der Frühphase eines derartigen Ereignisses bis zur Aufarbeitung der Langzeitfolgen zu unterstützen. Die vorliegende Doktorarbeit, die im Rahmen des Europäischen Forschungsprojektes CONFIDENCE („Coping with uNcertainties For Improved modelling and Decision making in Nuclear emergenCiEs“) durchgeführt wurde, zielt darauf ab, zu zwei Forschungsbereichen einen Beitrag zu leisten. Der erste dieser Bereiche umfasst wissenschaftliche Untersuchungen zur Evaluierung von sogenannten „citizen measurements“ (Bürgerbeteiligung bei Messungen). Daten zur Ortsdosisleistung im Umweltmonitoring könnten durch Laien aus der allgemeinen Bevölkerung erhoben werden, indem der Kamerasensor eines Smartphones mit dafür entwickelten Software Apps genutzt wird. In dieser Arbeit wurden zwei weit verbreitete derartige Apps, „Gammapix“ und „RadioactivityCounter“, im Hinblick auf den dynamischen Bereich einer Messung, die Messdauer, Übereinstimmung mit Referenz-Dosisleistungswerten sowie die Energie- und Richtungsabhängigkeit unter Verwendung von 13 verschiedenen modernen Geräten untersucht. Es zeigte sich, dass der Rauschpegel des verwendeten Kamerasensors den Nachweis bei niedrigeren Dosisleistungen (< 5 µGy h^{-1}) beeinflusste, wodurch Messungen der natürlichen Umgebungsstrahlung sich als schwierig herausstellten, während die App „RadioactivityCounter“ beim Nachweis höherer Dosisleistungen (> 10 µGy h^{-1}) vielversprechende Ergebnisse lieferte. Im zweiten Forschungsbereich wurden Mobiltelefone als passive Zufallsdosimeter untersucht. Die mit Surface Mount Technologie auf der Platine eines Mobiltelefons aufgebrachten Widerstände besitzen einen Keramikkern aus Aluminiumoxid (Al_2O_3), welches dosimetrische Eigenschaften aufweist und in der vorliegenden Arbeit zur Entwicklung einer neuen Methode der retrospektiven Dosimetrie genutzt wurde. Bei Messungen der Thermolumineszenz (TL) an derartigen Widerständen zeigte sich eine intensive Emission bei einer Wellenlänge von 695 nm, die auf Verunreinigungen mit Cr^{3+} zurückzuführen ist und Messungen im roten Spektralbereich ermöglichte (sogenannte rote TL oder RTL).

Im Vergleich zu früheren Messungen, die im blauen Spektralbereich unter Verwendung von etwa 10 Widerständen durchgeführt worden waren, ergab sich eine signifikante Erhöhung der Messempfindlichkeit. Dies ermöglichte die Entwicklung eines neuen Messprotokolls, optimiert für den niedrigen Dosisbereich und basierend auf nur einem einzelnen Widerstand. Der Vorteil des neuen Messprotokolls liegt unter anderem darin, dass ein einzelner Widerstand potenziell ersetzt werden kann, womit eine Zerstörung des Mobiltelefons verhindert wird. Mögliche Parameter, die die Präzision der Messmethode beeinflussen, wurden untersucht. Die Untersuchungen zeigten, dass Messungen im niedrigen Dosisbereich ($\leq$ 60 mGy) mit Widerständen aus Mobiltelefonen in einem potenziell zerstörungsfreien Ansatz wenige Stunden nach der Bestrahlung mit einer Unsicherheit von 10% möglich ist. Für Dosisbestimmungen nach einem Monat erhöht sich die Unsicherheit auf ca. 25%. Um die in einem Widerstand gemessenen Energiedosen in Organ-Energiedosen des Trägers des Mobiltelefons umrechnen zu können, wurden schließlich Strahlentransportrechnungen mit dem Monte Carlo Code MCNP6.2 durchgeführt. Für das beispielshafte Szenario eines Kernkraftwerksunfalls wurden für eine Bodenkontamination und drei ausgewählte Radionuklide (^{137}Cs, ^{131}I and ^{147}Nd) entsprechende Dosiskonversionsfaktoren berechnet. Zusammenfassend wurde in dieser Arbeit gezeigt, dass a) Laien unter bestimmten Voraussetzungen bei einem radiologischen Notfall Dosisleistungsmessungen mit einem Smartphone durchführen können, falls die zu messenden Dosisleistungen höher als der Untergrund sind, und dass b) mit dem neu entwickelten Messprotokoll Mobiltelefone bei einer unfallbedingten Strahlenexposition als Zufallsdosimeter genutzt werden können, wobei deutlich geringere Strahlendosen als zuvor rekonstruierbar sind und die Funktionalität des Mobiltelefons grundsätzlich nicht gefährdet wird.

Abstract

There is a risk for people to be accidentally exposed to ionising radiation in both, small-scale radiation accidents, for example in working environments where radiological sources are used, and in large-scale nuclear emergency scenarios, such as nuclear power plant accidents or mass-casualty terrorist attacks. Especially for the latter type of emergencies, adequate management strategies are required, in order to guide decision-makers from the "early phase" to the long-term rehabilitation.

The scientific work of the present dissertation has been carried out within the European project "Coping with uNcertainties For Improved modelling and Decision making in Nuclear emergenCiEs" (CONFIDENCE), and aimed to contribute to two research activities. The first one dealt with the scientific investigation on the reliability of so-called "citizen measurements" with smartphones. In fact, environmental monitoring dose-rate data might be acquired by laymen from the general population using the Complementary Metal Oxide Semiconductor (CMOS) camera sensor of a smartphone through dedicated applications. In particular, two widely spread applications, "GammaPix" and "RadioactivityCounter", were characterized with respect to their dynamic range, response time, dose rate response, and energy and angular dependence, for a total of 13 different and up to date devices. It turned out that the noise level of the camera sensors affected the detection at lower dose rates (< 5 $\mu Gy\ h^{-1}$), thus natural environmental radioactivity level remained difficult to determine. Nevertheless, overall the "RadiaoctivityCounter" app resulted to be promising in detecting higher levels of contamination (>10 $\mu Gy\ h^{-1}$) in most of the smartphones tested. In the second research activity, use of mobile phones as fortuitous dosimeters was investigated. The alumina (Al_2O_3) substrates of surface-mount resistors placed on mobile phone circuit boards possess dosimetric properties, which was used here to develop a new retrospective dosimetry method. Resistors showed a strong emission due to the Cr^{3+} emission at a wavelength of 695 nm, thus enabling Thermoluminescence (TL) measurements in the red detection window (RTL). The resulting strong increase in sensitivity, as compared to the earlier protocol where blue light emission and a total of about 10 resistors were used, allowed to establish for the first time a new protocol which is optimized for the low-dose region (10-100 mGy) and is based only on a single resistor. The single resistor can be potentially replaced, leaving the phone intact. Possible parameters affecting the precision of the method were explored.

In conclusion, individual dose assessments by sampling resistors from mobile phones, without irreversibly destroying the mobile phones themselves, could be possible within a 10% level of uncertainty for measurements of unknown low doses ($\leq$ 60 mGy) after a few hours after irradiation, and up to 25% for doses in the same range recovered after one month. Finally, the measured doses in the material were translated into organ absorbed doses using the general-purpose Monte Carlo radiation transport code MCNP6.2. Appropriate conversion factors were calculated for a real case scenario of ground contaminated by ^{137}Cs, ^{131}I and ^{147}Nd. In summary, the results of the present dissertation suggest that a) in a radiological emergency laymen may be able to perform useful dose rate measurements with their smartphone if the dose rates are well above background, and that b) the developed new measurement protocol allows mobile phones in general to be used as fortuitous dosimeters after a radiological emergency to reconstruct lower doses than before, potentially without destroying the mobile phones themselves.

List of figures

List of tables

1. Introduction

Nuclear emergencies that occurred in the past such as the Chernobyl accident (1986) or the Daiichi Nuclear Power Plant in Fukushima (2011), combined with the more recent hazard of potential terrorist attacks with Radiological Dispersion Devices (RDD) (Waller & Van Maanen, 2015), so-called "dirty bombs" (Woda et al., 2011), are the main reasons for an increasing public concern about accidental radiation exposures. Next to big-scale disasters, the possible occurrence of small-scale accidents at irradiation facilities or other working environments displaying radiological sources might result in overexposures of workers as well as non-monitored personnel. Especially in the latter cases independent dose reconstruction might be extremely useful. For these reasons in the latest years, the scientific community has put efforts in improving the radiological emergency management and the consequent long-term rehabilitation from such events. In particular, during the decision-making process one of the crucial point is to deal with information that is inevitably associated with uncertainties. For instance, uncertainties are intrinsic to the atmospheric dispersion parameters used as a first approach to model any accidental release of radionuclides from Nuclear Power Plants (NPP) into the atmosphere. Uncertain information can be also related to the exact location of the accident, as well as on the prevailing weather conditions. Furthermore, monitoring measurements could produce radiological data affected by a certain degree of uncertainty that can lead to a misleading assessment of the radiological situation. Thus in the presence of uncertainty, the risk of taking ineffective decisions, being either too conservative or too optimistic, might arise. The European Project "Coping with uNcertainties For Improved modelling and Decision making in Nuclear emergenCiEs" (CONFIDENCE) tried to address this issue of decision making under uncertainties in the management of a major NPP accident. The project concentrated on the „early-phase", when the emergency has just occurred, and on the „transition phase" that leads to the initial recovery, taking also into account longer-term decisions. In particular, the present work has been carried out within the Working Package 2, which aimed giving the best possible overall evaluation of the radiological situation and, consequently, of its impact on health. Especially at the early phase stage, it is critically important to obtain an accurate overview of the current radiological situation.

In order to reach this goal, the scheme represented in Fig. 1.1 summarizes all the necessary steps that could be taken in an emergency. Environmental monitoring data, early phase modelling of atmospheric transport with tools for dose calculations, and health risk assessment have to be combined in an optimal way. The first level of knowledge is represented by information at hand after passage of a radioactive plume, i.e. by data from any environmental monitoring network. Those data, complemented with atmospheric dispersion models, would be used to realize contamination maps identifying population groups potentially affected by high doses. These groups, perhaps still large, would be targeted by a specific software developed within the project, for individualized dose calculations (e.g. in emergency care centers). Such individualized calculations, supported also by information on the time spent by people in the contaminated areas, could be achieved in a relatively short time. That would help to promptly identify sub-groups of the population most affected by the exposure. The critically exposed sub-groups (with priority on children and pregnant women) would be then target by individual, and thus more accurate, dose assessments, usually limited in capacity and more time consuming. Individual dose assessment will have as final goal the health risk assessment to optimize health monitoring programs in the transition phase. Individual dose measurement strategies would imply the use of a combination of thyroid absorbed dose measurements, biological dosimetry and retrospective dosimetry methods.

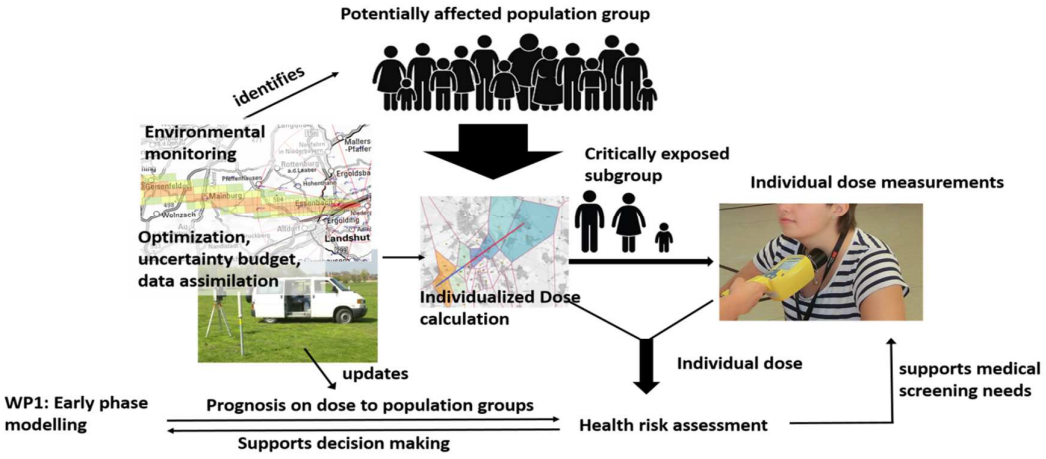

Figure 1.1: Structure and tasks interaction of the Work Package 2.

The following sections of this chapter describe in detail the different tasks of the present dissertation. Although focus is on large scale accidents and major nuclear emergencies, the method of retrospective dosimetry can potentially also be applied to smaller scale events leading to unplanned exposures of individuals.

1.1 Environmental monitoring with smartphone applications

One of the major steps to be taken to improve the awareness about possible unplanned exposures of individuals after a radiological emergency, would be to reduce uncertainties related to environmental monitoring measurements. While a large part of the research activities focus on characterizing and optimizing professional stationary and mobile environmental monitoring systems, another perspective could involve the participation of the general population themselves. In fact, the technological progress of the last years has enabled also lay people to produce monitoring data, probably not of ideal scientific quality, that might be helpful in reconstructing any individualized exposure histories.
Collaboration with citizens may be fruitful and, furthermore, people would be involved in self-protective operations in an active way. On the market many affordable devices for radiation detection are currently available, some of which have already been tested during the emergency scenario of the Fukushima accident in 2011 (Brown et al., 2016; Cervone & Hultquist, 2018; Coletti et al., 2017). An increasing number of cheap instruments are supported by smartphone technology, which does not require any particular scientific expertise. Especially the more recent models of mobile phones come along with a great variety of sensors and features that boost their usability beyond communication. Among such possibilities, mobile phones can be turned into ionising radiation detectors through:

- *External tools (plug-in or wireless)*:
  Solid state or gas detectors
- *Software tools*:
  Specific smartphone applications, based on the camera sensor of the phone

In this context, the emphasis of this dissertation is on the latter category, since their affordability (e.g. some are free or extremely cheap) might result attractive to citizens.

As reported in the CONFIDENCE Deliverable 9.8:“anyone who owns a smartphone could invest in a low-priced tool that turns the Complementary Metal Oxide Semiconductor (CMOS) camera sensor into a dose-rate detector” (Mafodda et al.,2019a).

1.2 Retrospective dosimetry

Within the context of the monitoring strategy depicted in Fig. 1.1, individual retrospective dosimetry methods based either on biological or physical techniques could play a key role once critically exposed sub-groups of population have been identified. In general, retrospective dosimetry (from the Latin retrospectare, “look back”) can be defined as “The estimation of a radiation dose received by an individual recently (within the last few weeks), historically (in the past) or chronically (over many years)” (Ainsbury et al., 2011). Aforementioned dosimetry methods are typically implemented when more conventional methods, like film badge personal dosimeters, are not available or should be independently verified (ICRU, 2002). In a radiological emergency scenario, and more general in case of an unplanned exposure, people would not be equipped with proper devices for ionising radiation monitoring. However, some personal items might possess dosimetric properties which represent both a valuable as well as challenging source of information. For everyday objects to perform as fortuitous dosimeters several requirements have to be met, as reported in Woda et al. (2012): “should show a unique and reproducible signal response to doses up to several Gy, no signal in the unexposed state, a lower detection-limit of tens of mGy and allow dose assessment with reasonable accuracy up to several days after the exposure”. In the last ten years, numerous studies targeted with different techniques a large variety of common objects that are usually worn or kept close to the body in everyday life. For example, investigations focused on clothes made of various types of fibers, cigarettes, banknotes and coins, as well as electronic devices. (ICRU, 2019). In this sense, next to the applications that actively can detect dose-rates through the smartphone CMOS camera sensors as described in section 1.1, phones can be used as an important source of individual doses in another way. The electronic components placed on the circuit boards, like surface mount resistors, inductors and capacitors, have been targeted for dosimetry applications since they contain an alumina (Al_2O_3) substrate sensitive to ionising radiation.

1.3 Thesis objectives

The present work, carried out in the framework of the CONFIDENCE European Project, aims to scientifically contribute to two tasks: the environmental monitoring performed by members of the public via smartphone applications and the development of a new retrospective dosimetry technique using surface mount resistors (SMRs) within the phone. The follow paragraphs list the main goals of the two activities.

1.3.1 Apps characterization

The first activity deals with the investigation of the reliability of the so-called "citizen measurements" carried out with a device that is extensively spread among population: smartphones. Though radiation detection through smartphone cameras is known to be attractive and inexpensive for lay people, the scientific debate on the reliability of such kind of measurements is still open. Previous studies (Tith & Chankow, 2016; Alessandri,2017; Cogliati & al.,2014; Van Hoey & al.,2016; Wagner & al.,2016) have been carried out on only a few models of mobile phones. In addition, their radiation properties likely change their specifics as newer models become available on the market. Therefore, to overcome such lack of knowledge, the present work focused on a wider variety of more up to date devices. Both the two main smartphones operating systems, Android and iOS, have been taken into account by characterizing the most promising software available for both of them. Two widely spread applications were characterized with respect to the response time, dose rate responses, energy and angular dependence of the devices.

1.3.2 Red Thermoluminescence for low dose detection and related uncertainties

The second activity deals with the development of a new dose assessment technique applicable on critically exposed sub-groups of the population as described in section 1.2. The new protocol is based on a physical dosimetry technique based on the alumina (Al_2O_3) substrates of surface mount resistors, detached from the circuit boards of different mobile phones. Luminescent properties of alumina contained in a range of different electronic component have been frequently studied in the past with different techniques, such as Optically Stimulated Luminescence (OSL) and Thermoluminescence (TL), the latter in the blue wavelength range. As reported in the CONFIDENCE Deliverable 9.10:"alumina based materials have shown a detection limit in the order of tens of mGy and a linear

dose response up to at least 10 Gy (Ademola & Woda, 2017; Lee et al., 2016; Ekendahl & Judas, 2012; Inrig, 2008)" (Mafodda et al., 2019b). From the same report: "especially for resistors, different protocols to prepare and measure the samples are nowadays well known, and inter-laboratory comparisons on reconstructing pre-delivered unknown low doses (<1 Gy), medium doses (1–2 Gy) and high doses (> 2 Gy) succeeded in about 90% of cases (Bassinet et al., 2014)" (Mafodda et al., 2019b). So far the limitation of applying this method in case of a nuclear emergency lies in the fact that in order to reach a detection limit of tens of mGy at least ten components per phone have to be sampled. In this way, the phone will be irremediably broken and, thus, the procedure would be generally not well accepted by the population. The present work potentially overcomes the mentioned issues by investigating the luminescent emission of the resistors in a new detection window (Red Thermoluminescence – RTL). In fact, preliminary spectral studies (Lee et al., 2017) have shown that the Thermoluminescence due to the Cr^{3+} (695 nm) surpasses other emissions by two orders of magnitude. Such strong increase in sensitivity was used in the present work to develop for the first time a new measurement protocol on a single resistor (sizes 1 mm x 0.5 mm x 0.35 mm), thus with the potentiality to be a non-destructive protocol. A sampling procedure on a single component might allow its replacement after measurement, thus leaving the phone operational and not damaged. Hence, the issue of general acceptability of the method by the public is taken into account. Furthermore, the reconstruction of individual doses with RTL technique was optimized in the low dose-range (10 – 100 mGy), to cover a dose range typical for the external exposure of the population following a nuclear emergency. As last step, sets of conversion factors for calculating organ absorbed doses from the doses measured in the resistors were derived with the Monte Carlo radiation transport code MCNP6.2 (Werner, 2017).

2. Fundamentals

In this chapter the theoretical basis of the two main research activities of this work are described. The first two sections 2.1 and 2.2 focus on the CMOS camera sensors and their functioning as a radiation detector with dedicated software applications. Section 2.3 aims to illustrate the luminescence phenomena and its use as a retrospective dosimetry technique. A more detailed overview on the RTL from chip resistors is then reported.

2.1 CMOS sensors

The technology that allows a smartphone to detect ionising radiations is already implemented in the device, even though it is not commonly used for this scope. In fact, what makes a normal mobile phone an actual dose-rate measurement device is its camera. Digital cameras as phone cameras create images from the interactions of light with a compound of lenses and an image sensor.

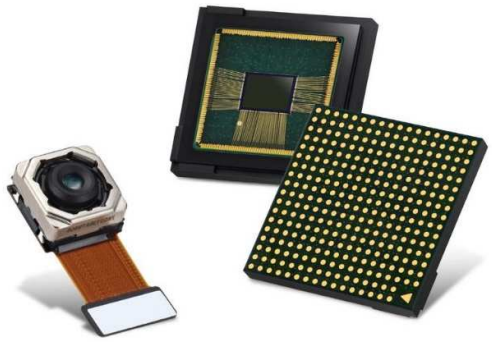

Figure 2.1: Image of a phone camera module and an image sensor (ISOCELL Slim 3P9 source: www.news.samsung.com accessed April 2021).

The two main types of digital image sensors are the Charge-Coupled Device (CCD) and the Complementary Metal–Oxide–Semiconductor (CMOS). Both are based on Silicon technologies and are sensitive in the same spectral range, from the visible to the near-IR spectrum (300 to 1000 nm) (Chouinard, 2015).

The working principle behind their functioning is the photoelectric effect that occurs when photons with a specific frequency hit a material. Electrons within the material absorb the energy of the photons and are able to escape from their orbitals. In the CCDs and CMOS the photoelectric effect takes place on their surfaces, containing millions of "photosites" also known as pixels. Each pixel is a p-n diode (photodiode) of only a few micrometers in size, actively responsible of the conversion of photons into an electric signal. The principal difference between CCDs and CMOS lies in the semiconductor element with which they transfer the charge out of the single pixels and into the electronics read out of the camera. In a CCD sensor, the charge transport occurs first "vertically" and then "horizontally", as represented in Fig. 2.2.

The conversion of charges from all the pixels takes place outside the sensor in the camera's electronics and the output is an analog pulse for which the charge is proportional to the light intensity. Disadvantages of CCD sensors are related to the process of reading out the entire chip that requires several clock cycles, so they tend to be slow as the number of pixels increases. Moreover, when adjacent pixels saturate the spread of charges causes the effect of "blooming", thus some very bright spots appear in the image. In the phones, and in general in small consumer devices, cameras integrated generally use CMOS sensors. They are usually cheaper and have lower power consumption, which makes them ideal for mobile devices. In a CMOS sensor, the charge conversion takes place in each pixel that is equipped with its own amplifier (see Fig. 2.2). In this way, the readout is much faster than in a CCD and the final output is digital.

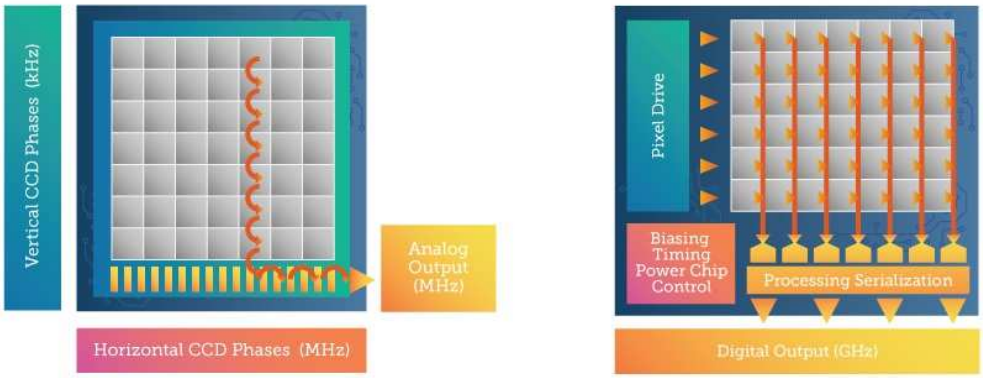

Figure 2.2: CCD (left) and CMOS (right) architecture comparison (source: www.possibility.teledyneimaging.com accessed August 2021)

Furthermore, a high image quality with high pixel homogeneity, very uniform signal with low fixed-pattern noise and usually low dark current, is achieved. To capture images in color, a color filter array (CFA) is needed, and the most common one is known as the Bayer Filter Array that consists of alternating rows of the three primary colors red, green, and blue. The filter is evident from figure 2.3 showing a close up view of a CMOS sensor.

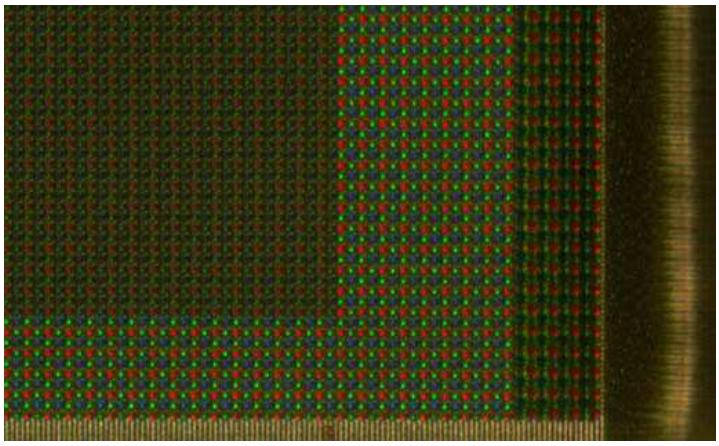

Figure 2.3: Close-up look of a typical CMOS sensor (source: www.ladingfield.wordpress.com accessed September 2021).

2.2 Applications for dose-rate detection

A CMOS camera sensor can turn a smartphone into a dose-rate meter thanks to specific software applications available on the market. The CMOS is constructed to be sensitive to visible light, as described in section 2.1, but when covered with an adhesive opaque tape, the contribution of X-ray and gamma photons becomes evident and detectable. The user may carry out a measurement by activating the camera in video mode. Interactions between photons and photodiodes are displayed as flashing bright spots on the dark background (Drukier, et al. 2011) (see Fig.2.4).

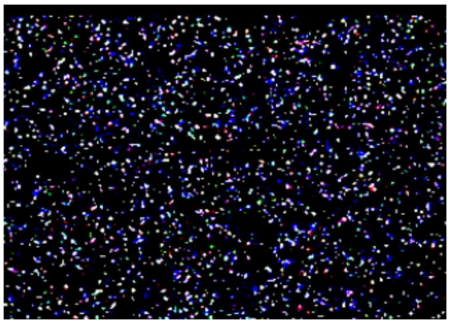

Figure 2.4: Images taken with a CMOS video camera exposed to ^{137}Cs (Drukier et al., 2011).

A dedicated software converts the recorded video into pictures (video frames), and processes them by "counting" the number of bright spots. Depending on the algorithm, the number of "counts" assigned to each group of adjacent activated pixels in selected time periods might vary (e.g. in the work of Tith & Chankow (2016), ten pixels were linked to one count). Overall, the image processing is application-dependent but this kind of software is characterized by the common feature of noise filtering. In fact, confounding signals might arise also from thermal noise, increasing with temperature, or from defective pixels that might light up periodically. Nevertheless, previous studies verified a linear increase of the counts with increase of the dose-rates (Tith & Chankow, 2016; Alessandri, 2017). It is possible to convert the counts to the actually present dose-rate through appropriate calibration factors. Since the response of the sensor varies between different phone models, such coefficients have to be determined for each model specifically. Thus, they are not always available and only in some cases, the producers list them on their websites or directly implement them within the application. Usually the applications permit the user to choose between carrying a measurement with the front or the back camera, and the choice can make a great difference in terms of radiation sensitivity.

The performance of the apps does not depend on the image resolution or on the total number of image pixels, but can be affected by the quality and the size of the sensor (Tith & Chankow, 2016). At the end of every measurement, the software stores the recorded data in a dedicated section where they remain accessible for post processing analysis. In this sense, some applications are more "open" than others, and allow to log data that can be downloaded as.csv files.

2.3 Luminescence theory

The physical phenomena of luminescence occurs in some solid materials that, subjected to radiation, have the property of converting part of the incident energy into photons. Their energy is typical of the luminescent material and completely independent from the incident radiation (McKeever, 2015). The stimulating agent used to induce photon emission gives name to the different types of luminescence. Therefore, accordingly:

Photoluminescence	Optical or UV light
Radioluminescence	Ionising radiation, e.g. α or β particles, γ-rays , X-rays
Cathodoluminescence	Electron beams
Triboluminescence	Mechanical energy
Electroluminescence	Electrical energy
Bio/Chemoluminescence	Biochemical or chemical energy
Sonoluminescence	Sound waves

Table 2.1: Different types of excitations that induce luminescence[1] (McKeever 1985)

In particular, after the absorption of the radiation, the light emission happens in a characteristic time τ_c, which can be used to distinguish between *fluorescence* and *phosphorescence*. Fluorescence happens on the scale of $\tau_c < 10^{-8}$ s , thus can be considered as a spontaneous process that takes place simultaneously with the absorption. Phosphorescence is characterized by $\tau_c > 10^{-8}$ s, therefore by a delay between absorption and emission, and it can even continue for some time after the excitation source has been removed. A further classification distinguishes short-period ($\tau_c < 10^{-4}$ s) and long-period ($\tau_c > 10^{-4}$ s) phosphorescence. The technique on which the present work is based is *Radioluminescence*, or more recently simplified to *Luminescence* (Yukihara & McKeever, 2011).

[1] The thermoluminescence (TL) method applied in this work is not listed because the luminescence is stimulated thermally but the excitation agent is the ionising radiation.

Thus, the luminescent properties of the materials investigated as dosimeters are triggered by the incidence of ionising radiations such as γ-radiation, X-rays and β-particles, relevant in the dosimetry field. In this context, ionising luminescence can be seen as a long-period phosphorescence, since τ_c can range from minutes to millions of years.

2.3.1 Energy Band theory

The mechanism of luminescence, as well as other physical and optical properties of a solid, can be readily explained by the Energy Band theory. This theoretical concept describes the states of electrons in solid materials. In a single isolated atom, the electrons in each orbital have a definite energy associated with it. In contrast, in case of a solid, all the atoms are close to each other: therefore neighboring atoms affect the discrete energy levels of outermost orbital electrons (Li, 1993). In an ideal crystal lattice, these interactions are ruled by the Pauli Exclusion Principle. This principle dictates that two or more electrons cannot occupy the same quantum state within a quantum system simultaneously. Consequently, if N is the number of identical atoms ($\sim 10^{22}$), each atomic orbital splits into N discrete molecular orbitals with different energies, which are closely spaced in energy and spread over the whole crystal. In this way an almost continuous band of energy levels is formed (Kittel, 2013). The most important energy bands in solid state are:

- *Valence band (VB)*: is formed by grouping the range of energy levels of the valence electrons of outermost orbital electrons. These electrons are loosely bound to the nucleus of their respective atom, so they are the ones involved in chemical bonding and electrical conductivity.
- *Conduction band (CB)*: is formed by grouping the range of energy levels of the free electrons.
- *Forbidden band or forbidden gap*: is the energy range that separates the valence band from the conduction band in some materials.

The energy bands are in the order of Electronvolt (eV), and depending on how they are arranged, materials might be classified in conductors, insulators and semiconductors.

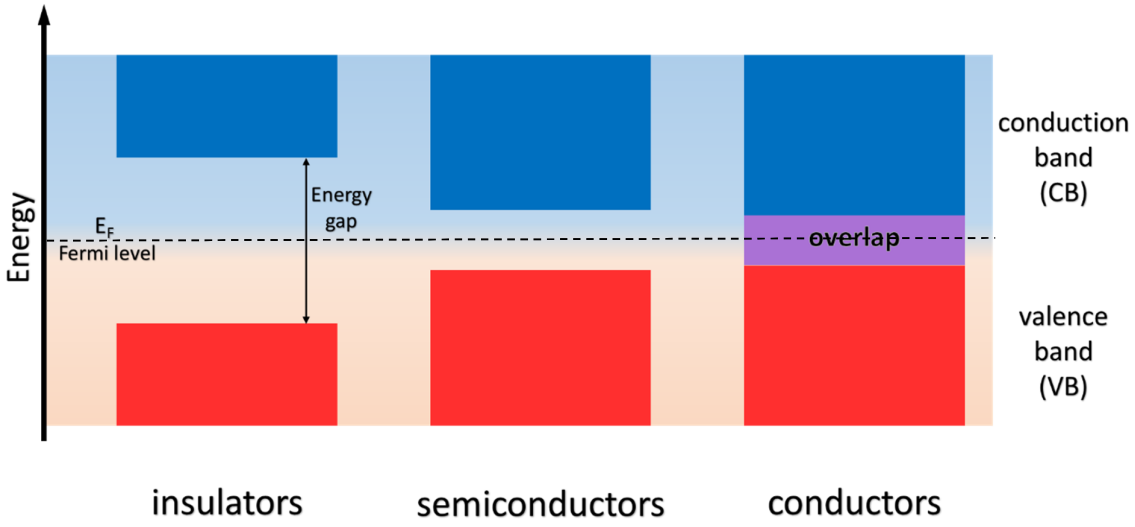

Figure 2.5: Energy band model for metal, semiconductor and insulator materials.

An important parameter in the band theory is the Fermi-Energy E_F. At the ground state of a system, i.e. at the absolute temperature of T = 0 K, all the electrons occupy the states below E_F in accordance with the Fermi-Dirac distribution, whereas all states above E_F are empty. The position of E_F with respect to the band energy levels is a crucial factor in determining the electrical properties of a material. In fact, metals are good conductors because E_F lies inside one of the bands. Therefore, an electron located in the VB does not have to overcome any energy gap to be promoted to the CB. In semiconductors, E_F lies in the forbidden band (less than 3 eV wide), implying that occupied and unoccupied states, in valence and conduction band respectively, are separated in energy. Finally, for insulators the energy gap between the two bands is large (~15 eV) and electrons from the valence band are unlikely to be promoted to the conduction band, hence such kind of materials are characterized by poor conductivity. The energy band theory is valid for an ideal crystal lattice. However, in reality, the regular geometrical arrangement of the atoms is interrupted by impurities or structural “defects”.

These can be located at single points (point defects or zero-dimensional defects), along lines (like dislocations or atoms misalignment), or on whole surfaces (planar defects). Point defects can be distinguished in intrinsic or extrinsic defects, depending on whether they are intrinsic impurities in the material or induced by external effects.

In particular, as shown in figure 2.6, intrinsic defects include lattice sites where atoms are missing, named “vacancies”, and sites where atoms usually are not present, named “interstitial”. Extrinsic defects are referred to “foreign atoms” that can replace a pre-existing atom at a specific site or at an interstitial site.

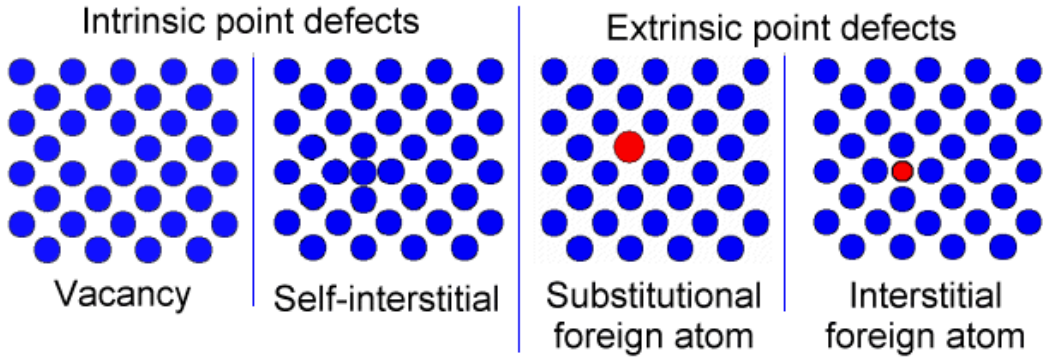

Figure 2.6: Schematic of intrinsic and extrinsic point defects.

Point defects add localized energetic levels in the forbidden gap that electrons might occupy. Acceptor levels are energy levels from defects located below the E_F and near the valence band, whereas donor levels are located above the E_F and closer to the conduction band. Therefore, the electron transitions from one energy level to another may occur between bands and localized levels. Direct transitions or band to band, involve charges that move from one band to the other without passing through any metastable energy level in the gap. Indirect transitions involve band-center or center-center transitions. A direct transition can, for instance, be caused by ionization, when electrons absorb the energy from an external source (e.g. ionising radiation) and are excited from the valence band to the conduction band (process “a” in figure 2.7).

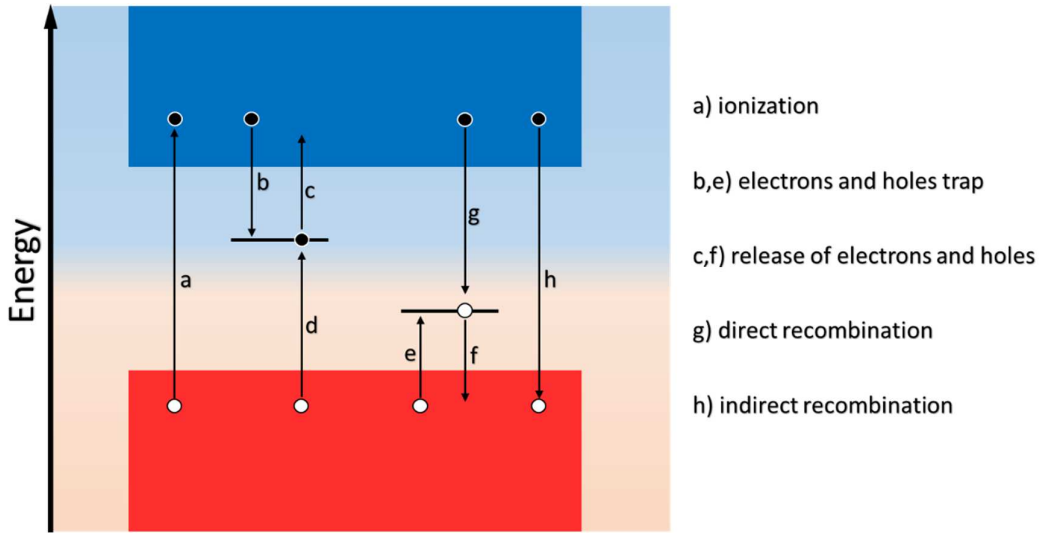

Figure 2.7: Electronic transitions in an insulator: solid circles represent electrons, open circles represent holes.

Every free electron in the CB corresponds to a free hole in the VB, so ionization creates electron-hole pairs that are free to move within the lattice until they come within the proximity of a localized defect. Then the trapping of electrons ("b" in Fig. 2.7) or holes ("e" in Fig. 2.7) occurs. Charges can be released from their traps (transitions "c" and "f" in Fig. 2.7) by thermal or optical excitation. A second option would be the recombination with a charge carrier of opposite sign either directly (transition "h" in Fig. 2.7) or indirectly with a previously trapped carrier ("d" and "g" in Fig. 2.7). The localized energy levels can act as traps or recombination centers, depending on the relative probabilities of transition. For the electron trapping center in figure 2.7, if transition "c" is more probable than "d" then the center is classified as a trap. On the other hand, if "d" is more probable than "c", the localized energy level is considered a recombination center. Similar considerations hold for the hole center and the transitions "g" and "f". In general, luminescence phenomena occur when the mechanisms of electron-hole recombination are radiative, i.e., if they are accompanied by emission of photons. Therefore, materials showing luminescence are insulators and semiconductors materials, where localized energy levels allow recombination processes within the forbidden gap. In conductors, the VB and the CB are not separated by any gap.

2.3.2 Thermoluminescence (TL)

As mentioned in section 2.3.1 charges can escape from their traps and recombine after a thermal or optical excitation. When the stimulation comes from an optical source, the Optically Stimulated Luminescence (OSL) takes place. When the stimulation comes from heating up the material, then Thermoluminescence (TL) results. The latter kind of luminescence should not to be confused, however, with the spontaneous light emission of a substance when heated to incandescence. For the TL, the material has to be exposed to radiation for some time. The simplest way to describe the Thermoluminescence process, assumes only two types of localized states: a discrete electron trap (T) located at a certain energy E_T , and a discrete recombination center (R) at a certain energy E_R (see Fig. 2.8).

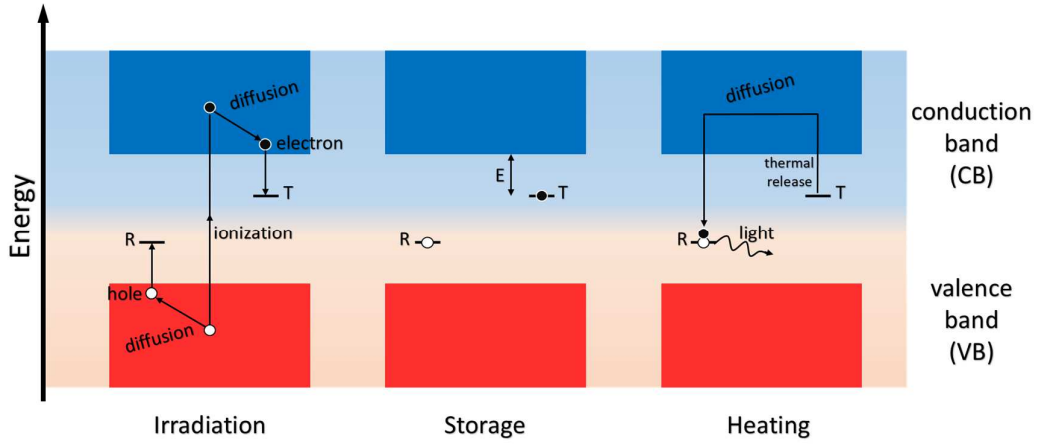

Figure 2.8: Simple two-level model for Thermoluminescence: electrons are the active carriers and are represented as solid circles whereas holes are represented by open circles.

The trap level is an electron trap as it is located above the E_F level, meaning that at the equilibrium state before the absorption of the incident radiation, it is empty. In contrast, the recombination center is situated below E_F where all the levels are full of electrons, so it is a potential hole trap. If external radiation with Energy $E = h\upsilon > E_C - E_V$ (greater than the gap energy) hits any insulator or semiconductor material, it is absorbed and causes ionization. As a result, the electrons e^- in the valence band are raised to the conduction band where they can move freely. In the valence band, the holes h^+ remain and can move as well: in this configuration free charge carriers might either recombine with each other, become trapped or remain free in their respective delocalized bands. The last case would imply that, after absorbing the radiation, the material would gain a greater

and stable conductivity than before. Such mechanism is not confirmed by observations, therefore it is not considered any further. Especially in wide band gap semiconductors and insulators, a direct recombination process involving e^- and h^+, in the two main bands across the gap, is less likely to happen compared to a recombination with localized defects. Thus, in order for recombination to occur, holes first become trapped at center R and then might annihilate with free electrons during or immediately after irradiation. If this process is assumed to be radiative, luminescence will result. This type of luminescence is called Radiofluorescence or Radioluminescence. Another possible recombination can origin from electrons trapped at level T (Fig. 2.8), only if they absorb enough energy E (Fig. 2.8) to be released back into the conduction band. In the latter case, the luminescence emission is delayed by the mean time τ that the electrons spend in the trap, given by the Arrhenius equation:

$$p(T) = \tau^{-1} = s \cdot \exp\left(-\frac{E}{k_B \mathrm{T}}\right) \tag{2.1}$$

where $p(T)$ is the probability of release of an electron from the trap per unit time, depending on the temperature of the release of an electron from a trap; E is the energy trap depth (eV); k_B is the Boltzmann's constant (eV/K); T is the absolute Temperature (K); s is a constant defined as frequency factor (Bos, 2007) in the order of $10^{12} – 10^{14}$ Hz. If the trap depth with respect to the temperature of irradiation T_0 is such that $E \gg k_B \mathrm{T}_0$, then any electrons (and consequently holes) that are trapped remain so for a long period of time even after the removal of the irradiation source. Since both the R and T levels are localized below and above the Fermi level, respectively they can be considered as non-equilibrium and metastable states. The return to equilibrium can be accelerated by increasing the temperature of the material above T_0 until $E \leq k_B \mathrm{T}$. Then, the probability of detrapping increases as well, and electrons will be released from the trap to the conduction band. Subsequently, these electrons can recombine with trapped holes resulting in Thermoluminescence. The intensity of the TL signal at any time during the heating is then proportional to the rate of recombination of trapped holes with electrons as given by the equation:

$$I(t) = -\eta \frac{dn_h}{dt} \tag{2.2}$$

Where n_h is the concentration of trapped holes (m^{-3}) and η is the radiative efficiency. If all recombination events produce photons and all photons are detected then $\eta = 1$ (McKeever & Chen, 1997). The relationship between $I(t)$ and n_h is represented in Fig. 2.9:

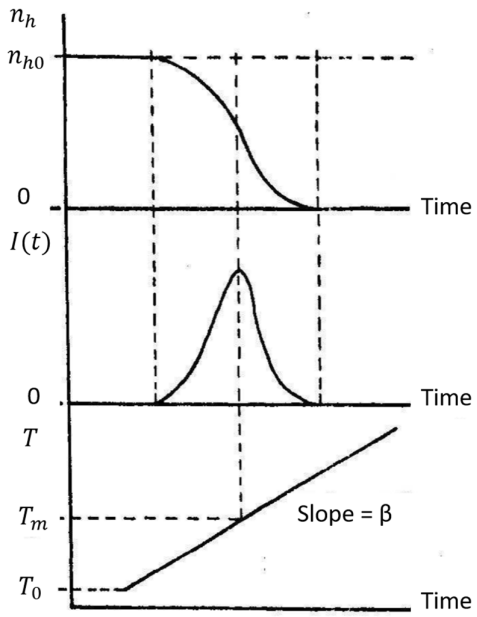

Figure 2.9: Thermoluminescence intensity I(t) and number of trapped holes n_h at the recombination centers. The linear increase of temperature with time, during heating, is illustrated in the lower plot. (McKeever, 1985).

As the temperature is raised, more electrons are de-trapped, recombination processes are more frequent, and the intensity increases. Progressively the traps are emptied, recombination processes are less probable and the intensity decreases. As a consequence, the typical TL peak signal is produced. Usually, in an experiment of this type, the temperature is raised linearly with time following:

$$T = T_0 + \beta T$$

Where β is defined as the heating rate ($K\ s^{-1}$) given by $\frac{dT}{dt}$.

Overall, the TL intensity plotted as a function of the temperature to which the sample is heated, is called “glow-curve” (an example is illustrated in Fig.2.10).

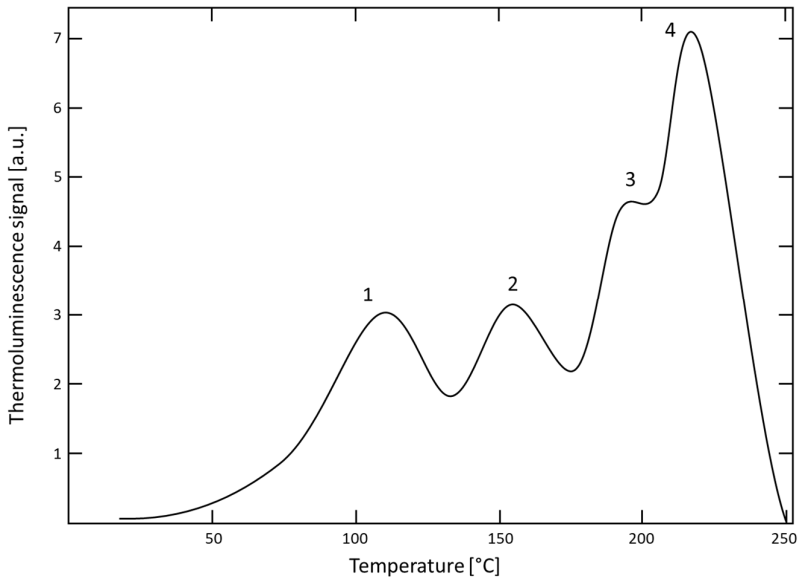

Figure 2.10: Thermoluminescence glow-curve from LiF doped with Mg and Ti after irradiation with γ-photons at room temperature and a dose of 2.5 Gy (adapted from McKeever 1985).

The process of trap emptying during heating requires some approximations in order to derive an analytical solution of the models describing luminescence. For the simple two level model, described above, two assumptions are often employed:

1. the concentration of free charge carriers in the conduction band is always much smaller than the concentration of the trapped charge carriers (m^{-3}):
$$n_c \ll n$$
2. the rate of change of the concentration of free charge carriers is always much smaller than the rate of change of concentration of the trapped charge carriers:
$$\frac{dn_c}{dt} \ll \frac{dn}{dt}$$

Thus, the concentration of free charge carrier is being approximately constant. These two assumptions together imply that the lifetime of the free charge carriers is much smaller than that of the trapped charge carriers, giving rise to a quasi-stationary free charge carrier concentration. With these assumptions, the following equation for the TL intensity can be derived:

$$I(t) = -\frac{dn_h}{dt} = -\frac{dn}{dt} = \frac{pn\,A_r n_h}{[A_r n_h + A_t(N-n)]} = \frac{pn^2}{n + R\,(N-n)} \qquad (2.3)$$

Where A_r is the recombination transition coefficient for electrons in the CB recombining with holes in recombination centers (m^3s^{-1}), A_t is the transition coefficient for electrons in the conduction band becoming trapped (m^3s^{-1}), N is the concentration of available electron traps (m^{-3}) and $R = A_t/A_r$. If the probability of retrapping is negligible compared with the probability of recombination, so that:

$$A_r n_h \gg A_t(N-n) \Rightarrow R \ll \frac{n}{N-n}$$

Equation 2.3 becomes:

$$I(t) = -\frac{dn}{dt} = pn = ns\exp\left(-\frac{E}{kT}\right) \qquad (2.4)$$

Integration from $T = T_0$, assuming a linear heating rate, gives:

$$I(t) = n_0 s\exp\left(-\frac{E}{k\mathrm{T}}\right)\left[-\left(\frac{s}{\beta}\right)\int_{\mathrm{T_0}}^{\mathrm{T}}\exp\left(-\frac{E}{k\mathrm{T}}\right)d\mathrm{T}\right] \qquad (2.5)$$

Which is the Randall and Wilkins expression for first-order (monomolecular) kinetics. (Randall & Wilkins, 1945). In dosimetric applications, the parameter n_0 is the most important one because is proportional to the absorbed dose in the material.

This parameter can be derived as the area below the glow-curve:

$$\int_0^\infty I(t)dt = -\int_0^\infty \frac{dn}{dt}dt = -\int_0^\infty dn = n_0 - n_\infty \qquad (2.6)$$

Where $n_\infty = 0$ for t→ ∞.

A different shape for the glow curve is derived, if the process of retrapping dominates during recombination:

$$A_r n_h \ll A_t(N-n) \Rightarrow R \gg \frac{n}{N-n}$$

And $n \ll N$:

$$I(t) = -\frac{dn}{dt} = \frac{n^2 s}{RN}\exp\left(-\frac{E}{k\mathrm{T}}\right) \qquad (2.7)$$

With $s' = s/RN$:

$$I(t) = n^2 s' \exp\left(-\frac{E}{k\mathrm{T}}\right) \tag{2.8}$$

In this case, the solution for a linear heating rate then becomes:

$$I(t) = n_0^2 s' \exp\left(-\frac{E}{k\mathrm{T}}\right)\left[1 + \left(\frac{n_0 s'}{\beta}\right)\int_{\mathrm{T_0}}^{\mathrm{T}} \exp\left(-\frac{E}{k\mathrm{T}}\right) d\mathrm{T}\right]^{-2} \tag{2.9}$$

Which represents the second-order (bimolecular) expression of Garlick and Gibson with R=1 (McKeever & Chen, 1997).

A second-order glow-curve arises because the probability of detrapping increases with temperature, respect to the first-order case. Therefore, a second-order curve will display more Thermoluminescence in the second half of the glow curve peak than a first-order glow curve. This can be seen in figure 2.11, in which computed glow peaks for first- and second- order kinetics are compared.

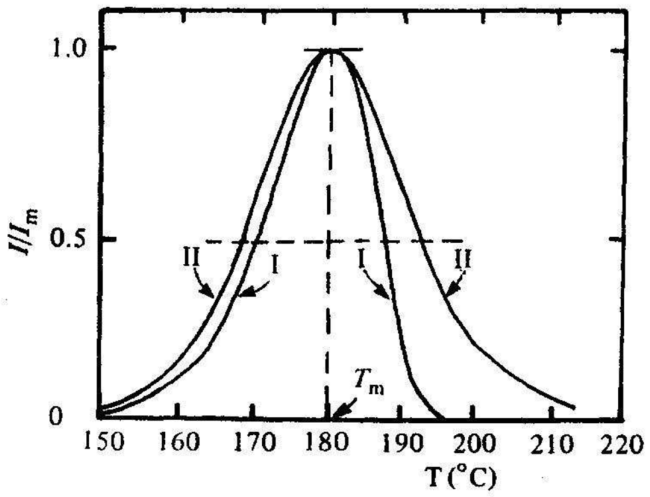

Figure 2.11: Computed Thermoluminescence peaks of first- (I) and second- (II) order kinetics. E=0.42 eV; $s=10^{10}$ s^{-1} (McKeever, 1985).

Both curves have been normalized to give the same peak height. By comparing the equations of the two types of kinetics, it can be noticed that the increasing part of the peak is

governed in both cases by terms in form of $exp(-\frac{E}{kT})$, whereas they differ for the decreasing part. The first-order peak is characterized by asymmetry, with most of the area being on the low temperature side of the maximum temperature. In some cases, a thermal detrapping that does not involve any of the above models occurs. In fact, during storage, where the trap is supposedly thermally stable, a signal loss following a temperature-independent $I \propto t^{-1}$ law can be observed. The model proposed to account for this behavior is the quantum mechanical tunneling from one site to another nearby, given by:

$$K = \nu \exp(-\phi r) \tag{2.10}$$

Where r is the electron-hole center separation (m), ν is a frequency factor (s^{-1}), and ϕ is calculated as:

$$\phi = \frac{2(2mE)^{\frac{1}{2}}}{\hbar} \tag{2.11}$$

Where m is the mass of the electron placed at the bottom of a potential well of depth E and $\hbar = \frac{h}{2\pi}$, where h is the Planck constant.

The mean lifetime of a charge carrier in a trap of depth E and escape frequency s at ambient temperature T, can be calculated from the Arrhenius equation as:

$$\tau = s^{-1} \cdot \exp\left(\frac{E}{k_B \mathrm{T}}\right) \tag{2.12}$$

Where the terms E and s are material dependent.

For many materials (e.g. quartz, feldspar, LiF, Al_2O_3:C) the lifetime of those charge carriers which are released at temperatures above 200°in the TL measurement, usually ranges from several thousands to several millions of years at ambient temperature.

However, for some materials it is often found that Thermoluminescence “fades” at room temperature at rates which are much faster than those expected from kinetic analysis.

This “anomalous fading” has serious consequences in a number of applications, including the use of thermoluminescent materials as dosimeters. A characteristic of anomalous fading due to tunneling is an initial rapid decay of the signal, followed by a slower decrease for longer storage times. Thus, the effective way of detecting anomalous fading is to perform long-term signal studies of irradiated samples, as it has been performed with resistors within this work (see chapter 4).

2.4 TL on personal items: SMRs of phones circuit boards

The TL technique is considered a successful method for radiation dosimetry since the late 1940s and early 1950s (McKeever & Moscovitch, 2003). In fact, the first application of TL in the dosimetry field was in 1953, when a specimen of LiF was used to measure radiation following an atomic weapon test (Daniels et al.,1953).

Luminescence techniques, such as TL, have proven to be powerful methods especially in the field of retrospective dosimetry after radiological accidents. In such cases, measurements can be carried out on materials accidentally exposed to ionising radiation and having the solid-state properties described in section 2.3.1. For example, the estimation of gamma dose in the dosimetry of the atomic-bomb survivors in Hiroshima and Nagasaki was performed by investigating bomb-exposed materials with TL measurements. In particular, in the early 1960s, first dose reconstructions were performed on samples from roof tiles of in the cities of Hiroshima and Nagasaki (Higashimura et al.,1963). Furthermore, bricks and tiles present as parts of buildings and other structures (e.g., brick fences) were targeted with TL measurements by Ichikawa et al. (1966) and Hashizume et al. (1967). In the 1980s a major milestone in the application of TL to atomic-bomb dosimetry was achieved through a multilaboratory study that produced a series of calibrations, intercomparisons and tests for accuracy and con- founding effects (Maruyama, et al., 1987). Also after the Chernobyl accident (Godfrey-Smith & Haskell, 1993) dose assessments were carried out by detecting the luminescence of quartz and feldspar samples extracted from bricks, tiles, pottery or porcelain items (Bøtter-Jensen & McKeever 1997). Or, in case of the Techa river contamination, occurred in 1949–1956 and caused by the disposal of liquid radioactive waste from the Mayak plutonium facility, dose reconstruction was performed using brick samples (Woda et al., 2020; Hiller et al., 2017; Jacob et al.,2003). Next to bricks, the dosimetric properties of a variety of objects, such as tiles, porcelain plumbing fixtures, tableware, flower pots (Haskell, 1993), which are mainly composed by ceramic, represent a powerful instrument for recovering information of an external unplanned exposure. Ceramic is also used as main substrates of the electrical components of surface mount technology (SMT) that is widely used for many electronic devices

(mobile phones, USB flash drives, mp3 players, etc…). This technology provides considerable advantages in terms of space saving and automated manufacture of printed circuit boards.

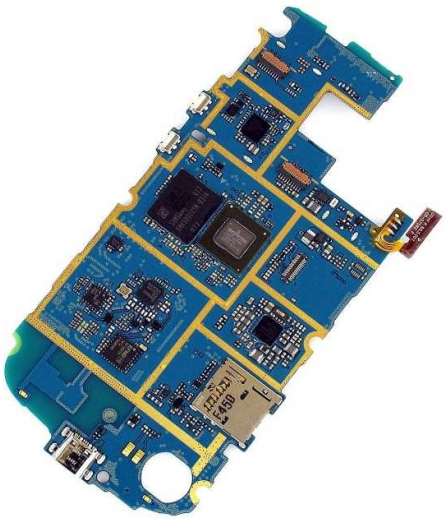

Figure 2.12: Printed circuit board (PCB) of a mobile phone model Samsung Galaxy Trend Plus (www.rounded.com accessed September 2019).

Therefore, portable electronic devices, can be classified as personal items that can be potentially used as fortuitous dosimeter (see section 1.2) (Beerten et al., 2009).
In particular, such device would allow direct measurements of individual doses. This is in contrast to bricks or tiles which can only be used to derive local doses. Nowadays, the most widespread devices used among the population is undoubtedly are mobile phones. Many of the materials found in the latter, either as part of the display (see the study on touchscreen glass of modern phones from Bassinet et al. in 2014, the study on TL from display glass by Discher et al. in 2013), or as resonators, capacitors, transistors and resistors on the circuit boards, have been subjects of several investigations. Furthermore, a phone is usually worn close to the body (e.g. in trousers pockets, shirt pockets). Thus, the doses deposited into its components can be converted to doses to body or organs. Electronic components from mobile phones and other kind of electronic devices, have been largely investigated with optically stimulated luminescence (OSL). Such method was proved to be reliable from many irradiation trials as well as from an international multilaboratory work of intercomparison (Bassinet et al.,2010). A “fast mode” and a “full mode” protocol have been validated successfully and luminescence dosimetry with OSL has

reached a certain level of maturity and standardization (Bassinet, et al., 2014). On the contrary, only few studies have examined in depth the usability of Thermoluminescence on this type of materials. This lack of knowledge might have an impact on all those national radiation protection agencies which have only ordinary TL readers available, not equipped with specific optical stimulation units.

The present work focuses on the properties of Surface Mount Resistors (SMRs) as Thermoluminescence dosimeters (see Fig. 2.13).

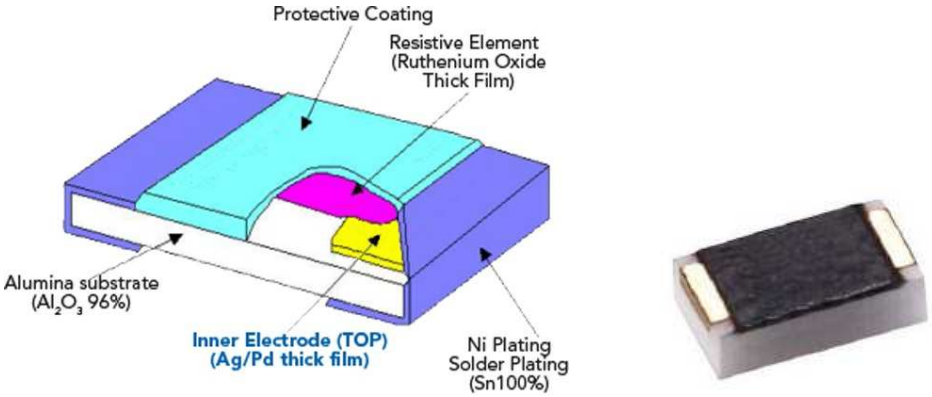

Figure 2.13: A schematic representation of a surface mount resistor (SMR) and its composition on the left (source: www.koaspeer.com accessed October 2021), and a picture of a real one on the right.

The dosimetric properties of resistors arise from the Aluminum oxide (Al_2O_3) substrate, or alumina, contained in their bulk core. In fact, depending on the manufacturing companies, resistor masses could be made up by more than 90% of alumina. The positions of the TL peaks from resistors, measured in the UV or blue detection window (Ademola & Woda, 2017), are similar to those observed from Al_2O_3:C which is used as a radiation detector for personal dosimetry mainly in the form of a ionizing luminescence dosimeter (TLD) (Bøtter-Jensen & McKeever, 1996). In particular, Al_2O_3:C produces luminescence at ~ 335 (UV emission band) and ~ 420 nm, the intensities of which are proportional to the concentration of neutral and charged oxygen vacancy centers, respectively named F and F^+ centers (Ekendahl & Judas, 2012). Expectations of similarities between the Al_2O_3 and Al_2O_3:C are the main reason why more work is required to fully evaluate the resistors potential as emergency dosimeters.

2.5 RTL on single resistor

Recent spectral studies on SMRs from Lee et al. (2017) have demonstrated that after 1 kGy of ^{137}Cs gamma ray irradiation, the TL signal from 40 resistors showed a strong emission in the red (695 nm).

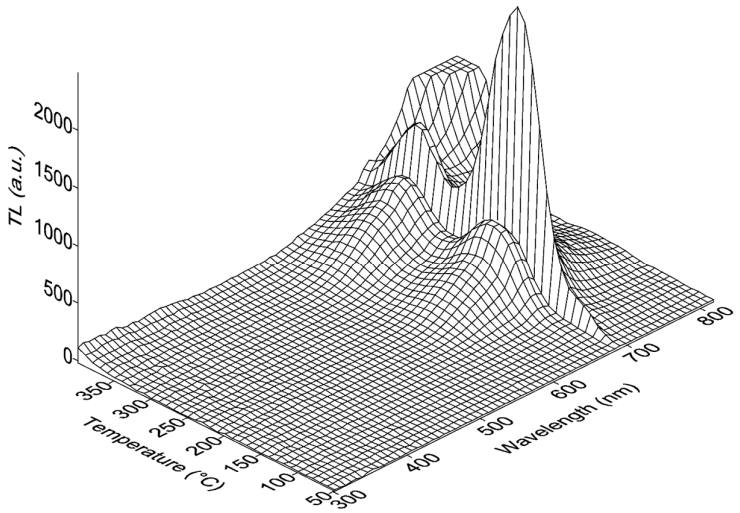

Figure 2.14: TL emission spectrum of a set of 10 resistors, irradiated with 100 Gy (courtesy of Woda C. paper in preparation).

This emission, which in un-doped Al_2O_3 had been attributed to the trace impurity of tri-valent chromium Cr^{3+} ions (Kusuma et al.,2019) surpasses in intensity the other emissions by two orders of magnitude (Fig. 2.15).

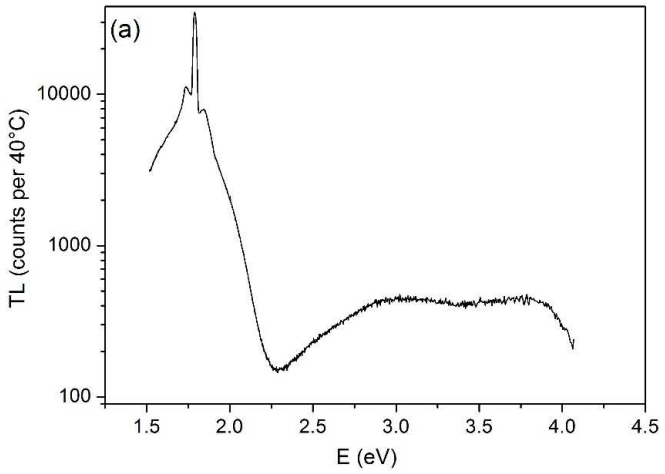

Figure 2.15: TL spectrum of a set of 10 resistors irradiated with 900 Gy (courtesy of Woda C., paper in preparation).

This dramatic increase in sensitivity should allow the development of a new retrospective dosimetry measurement protocol optimized in the low-dose region (10-100 mGy) using only a single detector (resistor of type 0402, with dimensions of 1 mm x 0.5 mm x 0.35 mm). Previous investigations on the TL signals from the SMRs reported in the literature usually referred to a multi-sample approach (groups of up to ten resistors) to get sufficient sensitivity (Ademola & Woda, 2017). This approach implied, however, that the phone would be irreversibly destroyed during the process of sample preparation, which could lead to a low acceptability of the method by the population. By developing a dose assessment method based on sampling at a single resistor level, the above mentioned issue is addressed, since a single resistor might realistically be replaced after the measurement.

2.6 Monte Carlo radiation transport calculations

In order for absorbed doses measured by fortuitous dosimeters to be useful for medical treatment or for radiation risk estimation following an unplanned exposure, it is necessary to relate the doses measured in these dosimeters to the doses that were simultaneously received by the individuals who had "worn" them. This suggests the development of specific conversion factors between dose absorbed by the materials to biological doses absorbed by human bodies, which might otherwise be naively assumed equivalent. For this purpose, the Monte Carlo-N-Particle radiation transport code was used in the present work (Version MCNP6.2, Werner, 2017). In general, radiation transport calculations represent a theoretical approach to solve complex three-dimensional problems, in which the state (location, energy, direction of movement) of a randomly selected particle is tracked on its way through any medium. From an initial state of the particle, specific algorithms (e.g. random number generators) determine the subsequent interactions with the matter (e.g. for photons, the photoelectric effect, Compton effect and pair production), including scattering processes. Calculations are performed until the particle is absorbed or it leaves the volume of interest. Then a new particle is simulated, and the whole numerical process is repeated until a maximum number of particles is reached.

The Monte Carlo-N-Particle is a well-established code for radiation transport. It has largely been employed since the 1940s in several different applications, including criticality safety, nuclear emergency, nuclear safeguards, fusion research, and medical technology. As reported in Salvat. et al. (2001): "in Monte Carlo simulations of radiation transport, the "history" of a particle is viewed as a random sequence of free flights that

end with an interaction event where the particle changes its direction of movement, loses energy and, occasionally, produces secondary particles". In order to simulate a given experimental arrangement, Monte Carlo simulation consists of the numerical generation of random "histories". Such histories are based on interaction models that comprehend sets of differential cross sections for the relevant interaction mechanism. The differential cross sections are related to the probability distribution functions (PDF) of the random variables that describe a track. Once these probability distribution functions are known, random histories can be generated using appropriate sampling methods (Salvat et al., 2001).

For example, let x be a continuous random variable in a certain interval from $x_{min} \leq x \leq x_{max}$. The probability of obtaining x in an differential interval of length dx about x_1, is given by:

$$P\{x|x_1 < x < x_1 + dx\} = p(x_1)dx \tag{2.13}$$

Where $p(x)$ is the probability distribution function of x. Since negative probabilities are meaningless and the value of x must be between (x_{min}, x_{max}), the PDF must be definite positive and normalized to unity. Any function that satisfies these requirements can be interpreted as a PDF. In Monte Carlo simulation, a PDF frequently used is the uniform distribution:

$$U_{x_{min},x_{max}}(x) = \begin{cases} \dfrac{1}{(x_{min} - x_{max})} & if\ x_{min} < x < x_{max}. \\ 0 & otherwise \end{cases} \tag{2.14}$$

Another example of a PDF for a continuous random variable x, is the cumulative distribution function defined as:

$$P(x) = \int_{x_{min}}^{x} p(x')dx' \tag{2.15}$$

This function is a non-decreasing function of x that varies from $P(x_{min}) = 0$ to $P(x_{max}) = 1$. For such distribution function, it is possible to define the inverse function $P^{-1}(\xi)$. By doing so, the transformation $\xi = P(x)$ defines a new random variable that takes values in the interval (0,1). Given the correspondence between x and ξ, the respective probability distribution functions are related through the following:

$$p_\xi(\xi) = p(x)\left(\frac{d\xi}{dx}\right)^{-1} = p(x)\left(\frac{dP(x)}{dx}\right)^{-1} = 1 \tag{2.16}$$

Therefore if ξ is a random number, uniformly distributed in (0,1), the variable $x = P^{-1}(\xi)$ is randomly distributed in the interval (x_{min}, x_{max}). The randomness of x is guaranteed by that of ξ, and x can be considered as the unique root of the so-called sampling equation:

$$\xi = \int_{x_{min}}^{x} p(x')dx' \tag{2.17}$$

Such method for random sampling is defined as the inverse transform method, and it can be applied to different types of probability distribution functions.

For example, from the uniform distribution in the interval (a, b):

$$p(x) \equiv U_{a,b}(x) = \frac{1}{b-a} \tag{2.18}$$

The sampling equation would be:

$$\xi = \frac{x-a}{b-a} \tag{2.19}$$

Which leads to:

$$x = a + \xi(b-a) \tag{2.20}$$

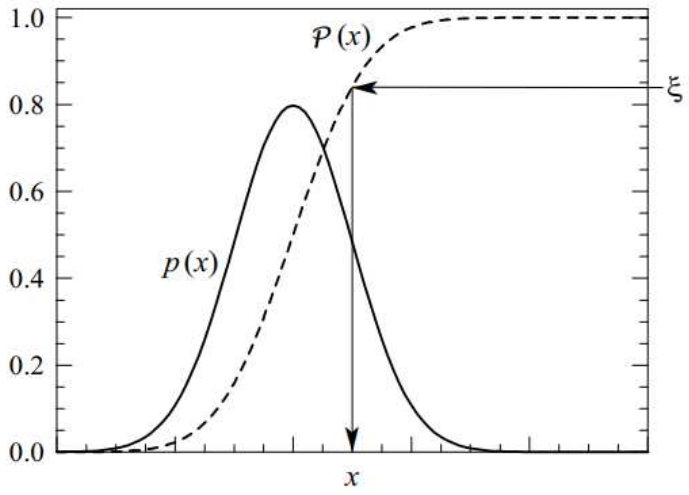

Figure 2.16: Random sampling from a distribution $p(x)$ using the inverse transform method (Salvat et al., 2001).

Another common application of the inverse transform method regards the exponential distribution of the free path s of a particle between interaction events:

$$p(s) = \frac{1}{\lambda}\exp\left(-\frac{s}{\lambda}\right) \; with \; s > 0 \tag{2.21}$$

Where the λ represents the mean free path. In this case, the sampling equation obtained by applying the inverse transform method would be:

$$s = -\lambda \ln(1 - \xi) \tag{2.22}$$

As for the length s of the free path, also the random variables associated to the involved scattering mechanism, the change of direction and the energy loss, are sampled from the corresponding PDFs. From these, Monte Carlo generates particle random tracks. In fact, according to the characteristics of the source, a particle starts from a specific location in space, with a certain direction of movement and energy. After any interaction, the consecutive states of the particle are described by its new coordinates $\boldsymbol{r} = (x, y, z)$, energy E, and direction cosines of the direction of flight. As a result, in every problem a large number of histories are generated and the overall accuracy of the Monte Carlo results is ruled by the laws of large numbers. From Salvat et al. (2001) :"if the number of generated histories is large enough, quantitative information on the transport process may be obtained by simply averaging over the simulated histories".

Any quantity of interest Q is evaluated as the average over a large number N of simulated individual q_i results:

$$\bar{Q} = \frac{1}{N}\sum_{i=1}^{n} q_i \tag{2.23}$$

and it approaches the real solution if the number of histories N tends to infinity.

The relative error of the estimate, named variance, can be approximated as the mean of the square of the scores subtracted by the mean score:

$$Var(q_i) = \frac{1}{N}\sum_{i} q_i^2 - (\bar{Q})^2 \tag{2.24}$$

The Monte Carlo method in general, and therefore also the MCNP code, thus does not give answers but statistical estimates of the mean value of a distribution.

In particular, Monte Carlo estimators are classified in four different classes: surface estimators, collision estimators, next-event estimators and track-length estimators. Surface estimators calculates currents, e.g. the number of particles crossing a surface. They can be used to estimate energy deposition by considering the energy crossing a surface into a region and subtracting the energy leaving the region through the surface. Collision estimators scores at collisions in the volume of interest with a functional that takes into account the weight of the particle, the track length, the cross sections and the particle properties (location in space, direction and energy). The next-event estimators calculate the flux at a certain point as the density function for particles to reach that point as the "next event" after being emitted from the source or from a collision event. In the present work, track-length estimators were used to derive dose estimates. These estimators are based on the fundamental definition of fluence as the number of particle-track lengths per unit volume. Therefore, they score all particle tracks in the designated time and energy range within a geometric space; then the flux is converted to energy deposition when multiplied by a kerma factor (heating number). The process of scoring the parameters of interest is called "tallying", and each tally is coded by an F_n:a number, where "n" is a unique number dedicated to a specific function and "a" is the type of particle to consider ("n" for neutrons, "e" for electrons, "p" for photons). All tallies are normalized to be per source particle. Energy depositions in the target volumes (for example the ceramic cores of resistors) were scored with the track length estimator F6 tally. In some cases the *F8 tally was also used, which estimates the energy deposition via an energy balance of particles crossing surfaces to enter or leave a volume. Energies are expressed in MeV and masses in g, hence doses are given in units of MeV/g^{-1} and can be converted to $Gy=J\ kg^{-1}$ by multiplying the result with a factor $1.602 \cdot 10^{-10}$. Calculations were carried out both in kerma approximation, thus assuming equilibrium in the generated secondary charged particles, with photon-only transport ("mode p"), as well as taking into account secondary electrons ("mode p e"). The geometries of the simulations presented in this work were set up using the software Visual Editor Version 25, based on the same radiation transport code MCNP6.2. The geometric structures can be filled with different materials by specifying the relative elemental composition: Appendix A reports on the compositions employed for modelling a real-sized surface mount resistor and realistic models of the NOKIA 6300 and NOKIA 1 mobile phones.

3. Materials and Methods

The following chapter describes the instruments and the protocols used to carry out the measurements of the dose-rates with CMOS camera sensors and the dose assessments with Red Thermoluminescence (RTL) on resistors. Section 3.1 is entirely dedicated to the smartphone applications selection and in particular, to "Gamma Pix" (full version) and "RadioactivityCounter". Section 3.2 reports on the RTL measurement protocol used for the experiments as well as on the Lexsyg Research Luminescent reader, which is part of the equipment of the Luminescent laboratory at the Institute of Radiation Medicine. In section 3.3 the radiation sources of the radiation facilities of the Helmholtz Zentrum München are described.

3.1 Dose-rate measurements with smartphone applications

A market research on the two major application online stores (Google Play Store and App Store) allowed to find smartphone applications for detecting ionising radiation currently available for Android and iOS systems.

Name	Developer	# of downloads	Rating	Price	Availability
Radioactivity Counter	Rolf-Dieter Klein	> 10.000	4.1	3.49 €	Android/iOS
GammaGuard	Environmental Instruments Canada	> 5.000	3.6	free	Android/iOS
GammaPix Gamma Radiation Detector	Image Insight Inc.	> 1000	3.4	3.79 €	Android/iOS
GammaPix Lite Gamma Radiation Detector	Image Insight Inc.	> 50.000	3.3	free	Android/iOS
Radioactivity-Meter	SpitConsult	> 100	3.3	3.56 €	Android
RadSensor (Geiger counter)	Zhang Hong	> 1000	3.2	free	Android

Table 3.1: Radiation detection applications and their specifications categorized in developer, number of downloads, ratings from users, prize and system availability, from CONFIDENCE Deliverable 9.8 (Mafodda et al.,2019a). Data retrieved in May 2018.

Some of the software characterized in past studies, like “WikiSensor” and “iRad” (Van Hoey, et al., 2016) were no longer available or not available on both operating systems, while some others have changed features. For instance, “GammaGuard” used to allow dose-rate detection with the camera sensor, but currently requires an external plug-in equipment. Therefore, it was rejected as object of the present study. The application “Rad Sensor” was discarded as well because it generally assesses a qualitative level of danger by taking a picture before and after irradiations. Thus, this was not in line with the real-time requirement that the present investigation wanted to be met. A non-reliable trend was detected by preliminary checks on “RadioactivityMeter” software, therefore, at the end, only two applications were considered as useful for further testing: “GammaPix” (full version) and “RadioactivityCounter”.

The main criteria for this selection were the latest updates, interface and instructions in English language, the compatibility with both Android and iOS systems, and the number of downloads, to focus on the most widely spread software (see Tab. 3.1). Information on “Gamma Pix” and “RadioactivityCounter” can be found on their respective websites www.gammapix.com/sites/ and www.hotrayinfo.de. Both “GammaPix” (full version) and “RadioactivityCounter” applications were downloaded in May 2018 and installed on 13 different mobile phones listed in Table 3.2:

Brand	**Model**	**Back Camera Resolution [Mp]**	**CMOS Sensor**	**Price when released**
APPLE	iPhone 6S	12	No info	700 € (December 2015)
ASUS	Zenfone2 Z00AD	13	No info	200 € (June 2016)
ASUS	Zenfone3 ZE520KL	16	SONY IMX298 Exmor S 5.22 x 9,92 mm 0,26 inches	200 € (November 2018)
HUAWEI	P8 lite 2017PRA-LX1	13	OV13850 Size 1/3.06”	160 € (November 2018)
HUAWEI	P10 lite WAS-LX1A	12	Size 1/2.8"	200 € (November 2018)

HUAWEI	Mate 10	20 + 12	LEICA 1/2.9"	450 € (December 2018)
KODAK	Ektra	21	Sony IMX230	300 € (November 2018)
LENOVO	K6	13	Sony IMX258 Exmor RS 4,71 x 3,49 mm 0,23 inches	200 € (November 2018)
MOTOROLA	E4	8	No info	120 € (November 2018)
NOKIA	1	5	No info	99 € (November 2018)
WIKO	Lenny3	8	No info	150 € (December 2016)
XIAOMI	Mi A1	12	OV12A10 5,11 x 3,84 mm 0,25 inches	160 € (November 2018)
ZTE	Blade L5 plus	8	No info	170 € (December 2016)

Table 3.2: List of smartphones tested and their characteristics. As reported in the CONFIDENCE Deliverable 9.8: "In most cases, manufacturers did not provide information on type of camera sensor and sensor size, therefore this can be only shown for a few models. No information is given for front cameras, since most tests were performed on the back cameras only." (Mafodda et al., 2019a).

By choosing such a variety of models, it was possible, first, to explore how the camera sensors might vary in sensitivity, and second, to evaluate the quality of the calibration factors employed by the applications. Most of the tested phones were chosen among the recent models from the most popular brands sold in 2017, belonging to different price ranges. In both apps, the user can select to carry out a measurement either with the front or with the back camera, but most tests were performed on the back camera (Mafodda & Woda, 2020). After some preliminary tests on selected models, the front camera resulted to be less sensitive, although it is difficult to assess that as a general statement in every case. Only in the case of the energy dependence study, reported in section 4.1.3, the relative response of both the front and the back CMOS sensors was directly compared for four phone models. "GammaPix" and "RadioactivityCounter" are based on the same working principle already described in section 2.2.

In the CONFIDENCE Deliverable 9.8, the following is reported: “they enable the CMOS sensor, sensitive to visible light, to detect ionising radiation when shielded with adhesive black tape. After covering the camera, the user may run a measurement that consists of a video record where every interaction of radiation (photons) with the chip is observed as an intense signal in a certain pixel (bright spot). The dedicated software analyses each video frame by counting the number of spots, at a frame rate depending on the smartphone model. The sum of detected particles in selected time periods is given as number of counts that can be further converted to dose-rates if appropriate calibration factors are available.” In the following paragraphs, the two selected applications are described more in detail.

3.1.1 “Gamma Pix” (full version)

After installation, the application “GammaPix” did not provide proper calibration values for all the tested models. A message of “Calibration Not Found” (see Fig. 3.1 - left) was displayed and an “approximate” one was used instead. Immediately afterwards, an automatic initialization consisting in a three-step procedure starts, assesses the background and sets an approximate calibration value (see Fig. 3.1 - right).

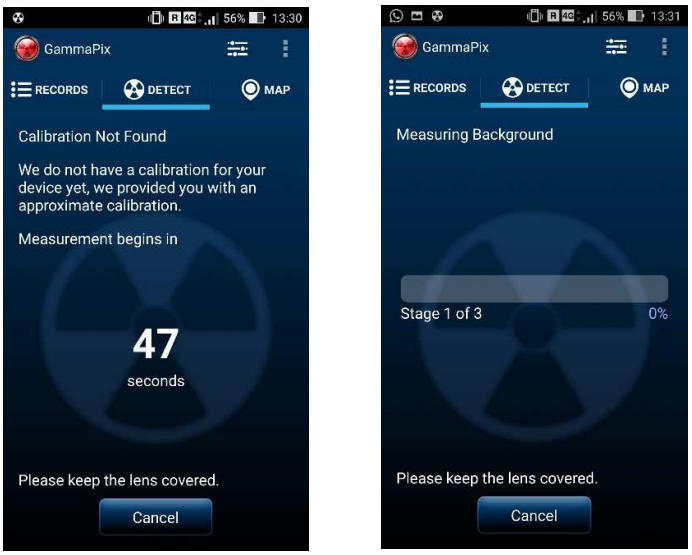

Figure 3.1: On the left, display of “calibration not found”. On the right, background assessment. CONFIDENCE Deliverable 9.8 (Mafodda et al., 2019a).

This process cannot be modified afterwards, but on the developer's website (accessed October 2021), a table lists how well the app performs on some devices by classifying their sensors from "one star" (associated to not recommended phones) up to "four stars" (associated to recommended phones) (see: http://gammapix.com/devices/).

Users are then enabled to run a measurement in two different modes: "Real Time" or "Three Stage". In "Real Time" mode, the dose-rate measurement can be watched while it is carried out, whereas the "Three Stage" mode quickly gives a warning of danger if dose rates are high. In the present work, the "Real Time" mode was selected. Left Fig. 3.2 illustrates an actual measurement displayed as a series of dots. Every dot is associated to the mean value of the dose rate registered in the specific range of time. The final value of dose rate assessed is visualized as a single line in a colour-coded, log-scaled bar chart (Fig. 3.2 right).

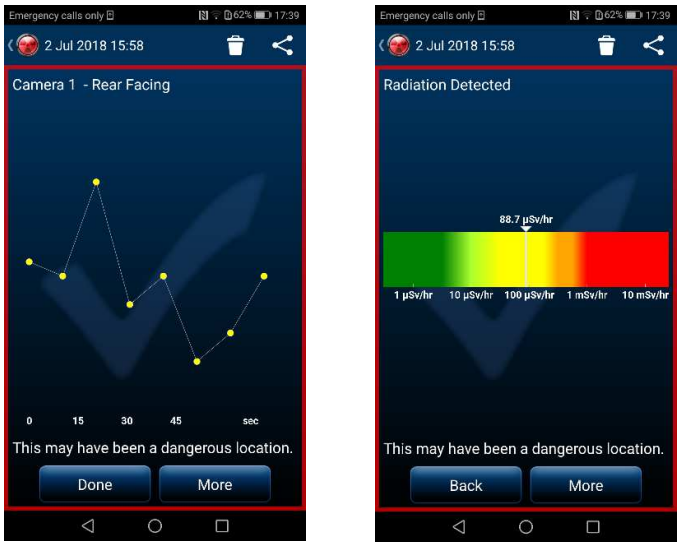

Figure 3.2: On the left, display of a measurement while it is ongoing; on the right, display of the results after the measurement is finished. CONFIDENCE Deliverable 9.8 (Mafodda et al., 2019a).

At the end of every measurement session, depending on the colour, three different "alert messages" may be displayed:

- ***Reading Unclear***: associated to a low level of ionising radiation.
- ***All clear***: associated to the absence of ionising radiation, meaning the area is safe.
- ***Radiation detected***: associated to an highly contaminated area

The level of danger, along with other information, as the dose-rate detected and the camera used (front or back), are saved and stored in a specific section of the software.

The lack of precision in the approximate calibration assessed at the beginning, lead to the following results reported in Mafodda & Woda (2020): "an underestimation of the nominal reference values on most of the phones by at least an order of magnitude. The same issue also affected the system of warning messages displayed at the end of a measurement". Moreover, from the same paper: " "Unclear reading" message was shown usually after a short measurement time (5 min), in agreement with the minimum exposure time between 10 and 25 min recommended in the literature (Van Hoey, et al., 2016)".
Reference dose-rates of 50 μGy h^{-1} were classified as "No radioactivity detected", potentially leading to dangerous misinterpretations. Therefore, more efforts were put into the characterization of "RadioactivityCounter" app.

3.1.2 "RadioactivityCounter"

As soon as "RadioactivityCounter" is launched on a device, it assesses the noise level "*n*" of the CMOS sensor through an automatic procedure.

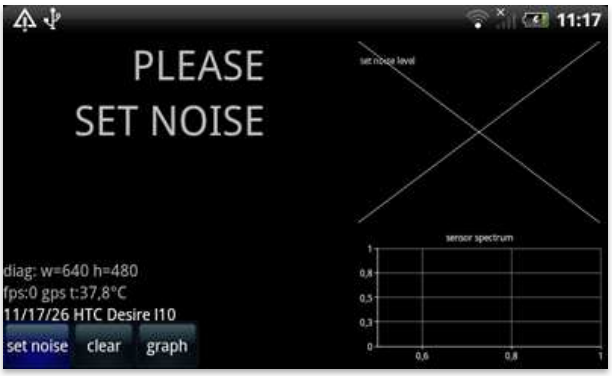

Figure 3.3: Noise assessment step with "RadioactivityCounter".

The *n* value can be considered as a threshold above which any event is classified as such and therefore registered. A default value of 70 nSv h^{-1} is stored as "background dose-rate", but it might be easily modified by the user in the "Adjust" menu of the app. When detected count rates are lower than the threshold value, such stored "background" value is returned as a result. Moreover, the app is not limited only on counting the number of pixels activated by the interaction with photons, but it evaluates the difference in pixel values between two consecutive video frames (setting the camera in a greyscale).

Thus, after the interaction with photons takes place, the contribute of every pixel to the final number of counts detected in time is weighted depending on its level of brightness. Figure 3.4 represents a real measurement visualized as a series of histograms. Each histogram is built up by the counts detected in a one-minute time interval.

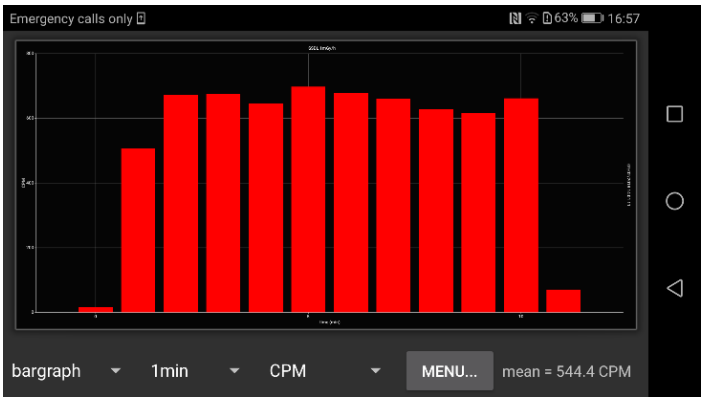

Figure 3.4: Example of a "RadioactivityCounter" measurement performed with a HUAWEI P8 Lite irradiated with ^{137}Cs at 1 mGy h^{-1}.

In contrast to "GammaPix", "RadioactivityCounter" offers the users to perform their own calibration by manual input of calibration factors that convert Counts Per Minute (CPM) to dose rates. On the website of the developer (accessed October 2021), users can access a list of conversion factors for different phone models. However, since then, such a list has not been updated with reference to the more recent devices available in the market.
Through a "Start log" function, "RadioactivityCounter" also allows to log data that can be downloaded as.csv files. The latter enclose information on date and time of the measurement, sensor temperature, and count-rate (or dose-rate if the device is calibrated) recorded in every minute.
For the present thesis, results refer to mean values of counts that have been calculated from the log data. In particular, the initial and final two minutes of every measurement were excluded, but always ensuring a minimum integration time of ten minutes. As in the paper of Mafodda & Woda (2020): "This was necessary as the app could not be operated remotely but had to be started before the source could be opened and stopped after the source had been closed. Such asynchronism in source and app operation was a reason suspected by Van Hoey et al. (2016) for an observed initial underestimation of counts."

As uncertainty of the single measurement, the standard error of the mean was taken into account. In fact, when an adequately large number of events are recorded, the average can be considered to be normally distributed, regardless the underlying distribution of the one minute events recorded. In this respect, count-rates are assumed to be statistically independent (uncorrelated). The dose rate response of all the cameras was tested by irradiating the phones in free in air conditions: the phone to test was fixed to a special harp holder and irradiations were performed with a ^{137}Cs source at air kerma rates ranging from 2 μGy h^{-1} to 1000 μGy h^{-1}. The "RadioactivityCounter" app had been precalibrated by the developer with two test sources of ^{137}Cs and ^{60}Co (see following section 3.3) in terms of air kerma. Furthermore, the app returns as output the dose-rate in (μ,m)Gy h-1, both automatically for iOs based models and after a proper calibration for the Android based ones. Therefore, the air kerma was maintained as reference quantity for the dose-rate response study.

3.2 RTL Measurements

The new retrospective dosimetry method developed within this work is based on the red thermoluminescence emission from surface mount resistors. In particular, measurements were carried out on a single chip type "0402", characterized by dimensions of 1 mm x 0.5 mm x 0.35 mm, extracted from electronic circuit boards of different phone models and brands. The whole procedure of sample preparation was entirely carried out in dark room conditions, to avoid any light-induced transfer of charges into deep traps. The resistors were extracted from different models of mobile phones, under a microscope and with the aid of a scalpel and tweezers.After the extraction, the samples were cleaned and prepared following a protocol specifically designed for the present work. The samples were placed in the stainless steel cups of the Lexsyg luminescent reader with the ceramic side facing upwards, as depicted in Fig. 3.5, since the luminescent material is the white alumina porcelain substrate. Before placement of the samples, the cups (ø = 10 mm) are sprayed lightly with silicon oil to ensure that the components do not move or fall off in the process of movement.

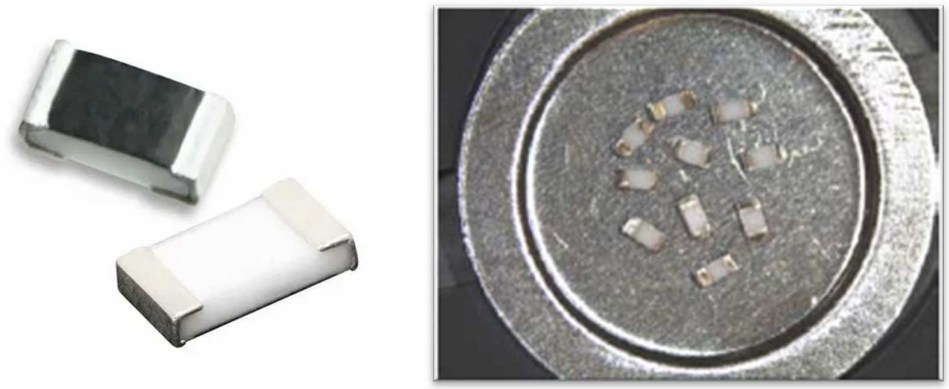

Figure 3.5: On the left, representation of a resistor in its standard position on the circuit board (top) and with ceramic facing upwards (bottom); on the right, a picture of a measurement cup with 10 resistors.

Samples were preheated at 120°C for 10 s in order to remove the lower temperature TL peak at ~ 80°C (Beerten et al., 2009). For the determination of the signal values, the TL glow curves were integrated from 125°C to 180°C.

3.2.1 LEXSYG Luminescence reader

In the present work, the RTL measurements were carried out with the "LEXSYG Research" luminescence reader developed by Freiburg Instruments shown in Fig.3.6.

Figure 3.6: Picture of the "LEXSYG Research" luminescence reader by Freiburg Instruments (source: www.lexsyg.com accessed November 2021).

The reader consists of a modular system (see Fig. 3.7) designed to perform investigations on the luminescence of materials using either Thermoluminescence or Optically Stimulated Luminescence techniques. In comparison to other existing luminescence readers, the LEXSYG Research is more versatile and flexible, since it allows the user to carry out luminescence stimulation and measurement without modifying the instrumentation during or between measurements (Richter et al., 2013).

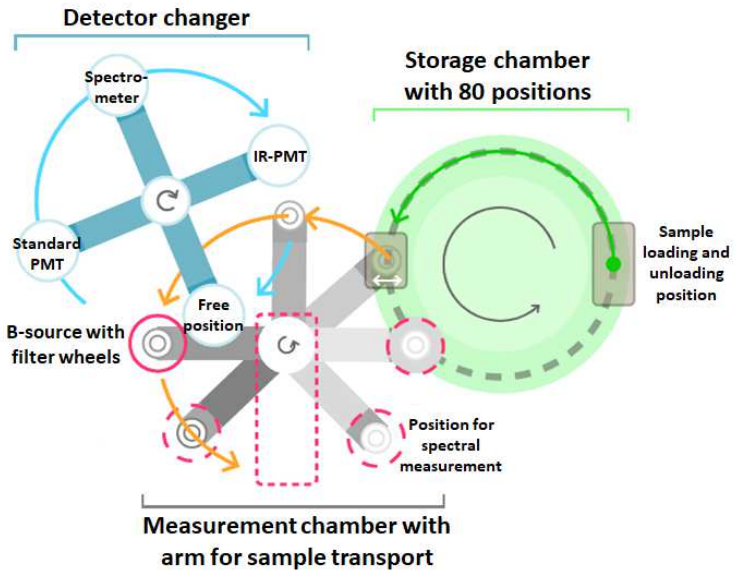

Figure 3.7: Schematic representation of the LEXSYG Research components (Richter et al., 2013). PMT stands for photomultiplier tube and IR-PMT for infrared – photomultiplier tube.

- **Storage chamber**

Represented in green in the figure above, it consists of a wheel with 80 positions where the aliquots are stored within cups of Ø=10 ± 0.1 mm. The wheel is controlled via the Lexsyg software installed in the PC of the system, and rotates each time a sample has to be measured. In this way, samples are transported by a pneumatic handling system from the storage position directly to the measurement chamber. It is important to mention that the storage wheel and the measurement chamber are two different environments separated by a rubber seal. The latter is mechanically opened and closed during the sample transfer. Therefore, at any time during a measurement sequence it is possible to load and unload the aliquots.

- **Measurement chamber**

At the beginning of every TL measurement, a vacuum pump evacuates the chamber and the atmosphere is filled with Nitrogen. In this way, the Oxygen level inside the chamber is reduced and the risk of oxidation of the heating plate is minimized.

- **Radioactive source**

The irradiation unit consists of a β-source of ^{90}Sr / ^{90}Yr placed in the measurement chamber. The source design is a ring, providing a homogeneous irradiation field of about ±2% at 8 mm diameter of the irradiation area (Richter & al., 2012). Its design also allows to perform radiofluorescence measurements during beta irradiation. The irradiation unit opens and closes by a pneumatically driven system.

- **Detection unit**

The LEXSYG research is equipped with a detector changer unit that can select four different kinds of detectors placed in four different positions. Currently, the reader of the TL/OSL laboratory of the Helmholtz Zentrum München is equipped with three detectors. One is the Thorn-EMI 9235Q Photomultiplier tube with a bialkali photocatode (Products for Research, Inc.) that according to the manufacturer has a quantum efficiency of up to 30% between 160 and 630 nm (ET Enterprises, 2014). The second one is the spectral measurement unit: a glass fiber transports the light signal into a Shamrock 163 Spectrometer and an iDus 420 CCD Camera from Andor Technology. The third detector is a Hamamatsu H7421-40 Photomultiplier tube having a GaAsP/GaAs photocathode, which offers a high sensitivity in wavelength from 300 nm to 720 nm. The H7421-40 is equipped with a thermoelectric cooler that reduces thermal noise generated from the photocathode, leading to a high quantum efficiency and allowing measurements with a good S/N ratio even at very low light levels. The latter has been specifically used in this work for detecting the luminescence in the red detection window.

- **Detection filters**

In luminescence applications, filters in the light path of detection are commonly used in order to restrict the detection window. In particular, inside the LEXSYG research reader, for each detection module there are up to two filter wheels. In each wheel there are six filter positions that can be selected via the software. The TL and OSL signals can be then recorded with a combination of glass filters (e.g. Schott KG3, Schott BG3, Schott BG25, Schott BG39 and Hoya-340) and interference filters (e.g. 280 nm, 330 nm, 380 nm, 410 nm and 620 nm). For the RTL measurements a combination of a glass short pass filter Schott KG3 (3 mm thickness) and a long pass filter type Schott OG 570 is used (see Fig.3.8). The first one is characterized by high transmission in the visible (transmittance above 80% for 365 nm < λ < 600 nm) and high absorption in the IR range (transmittance below 10% for λ ≥ 800 nm). On the other hand, the Schott OG 570 has a high transmission in long wavelength ranges (transmittance of 92% for λ > 640nm).
The detection with the Hamamatsu H7421-40 Photomultiplier in combination with the above mentioned filters gives the best S/N ration for the RTL signal.

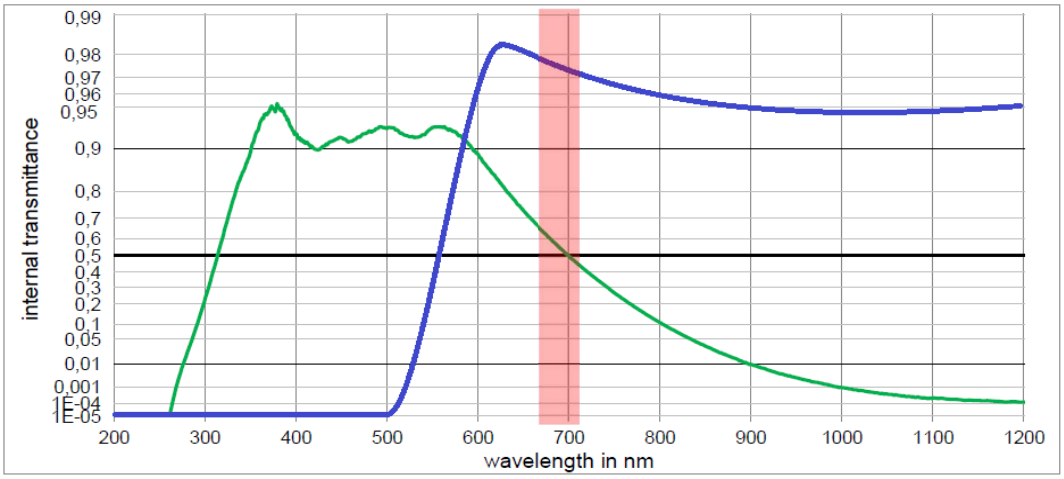

Figure 3.8: Optical transmittance of the combination of filters employed in this work: green line is referred to glass short pass filter Schott KG3, blue line to the long pass filter Schott OG 570. The red area represents the main emission range of the resistors (695 nm – see section 2.5), target of the RTL.

- **Thermal stimulation**

For the Thermoluminescence signal a thermal stimulation of the sample is required. The heating plate is integrated in the sample arm which moves between the different detector positions and the source. The heating plate consists of a metal plated dielectric heater that can reach a T_{max}=700°C. The temperature calibration is obtained with a Pyrometer and a closed loop gas flow system allows to control the heating and the cooling at any specified rates. The heating rate used for RTL measurements was set to 2°C/s up to a temperature of readout of 350°C, as it will be explained in detail in the results section.

3.3 Radiation sources

For the present work, the Gamma source and the X-ray sources present at the radiation facilities of the Helmholtz Zentrum München (HMGU) were employed for both activities, the dose-rate smartphone app characterization and the retrospective dosimetry protocol with RTL measurements on chip resistors.

3.3.1 X-Rays sources MG160 and MG320

In the radiation facilities of the HMGU, two X-Ray sources from PTW Freiburg with 320 kV Philips and 160 kV are available. The sources are placed one in front of the other and they are separated by a calibration bench of seven meters (see Fig.3.9).
Each unit is characterized by: two fixed and three pairs of circular apertures of diverse radii, a shutter, a control system connected to a computer, and a wheel equipped with high purity metal filters (Greiter, Denk, & Hoedlmoser, 2016). Through a dedicated software, it is possible to select the attenuation filters that the beam has to pass through to obtain a specific energy. For the present work, a series of ISO-Norm (4037-1, 1996 and 4037-3, 1999) of narrow spectrum qualities from N30 (mean energy of 24 keV) to N300 (mean energy of 250 keV) was used. The narrow spectrum qualities correspond to mean energies in the range between 24 keV to a maximum of 250 keV: maximum air kerma rates vary depending on the radiation quality. In general, the radiation field diameters at one meter distance are 5, 10.5 or 16.5 cm with the appropriate pair of apertures.

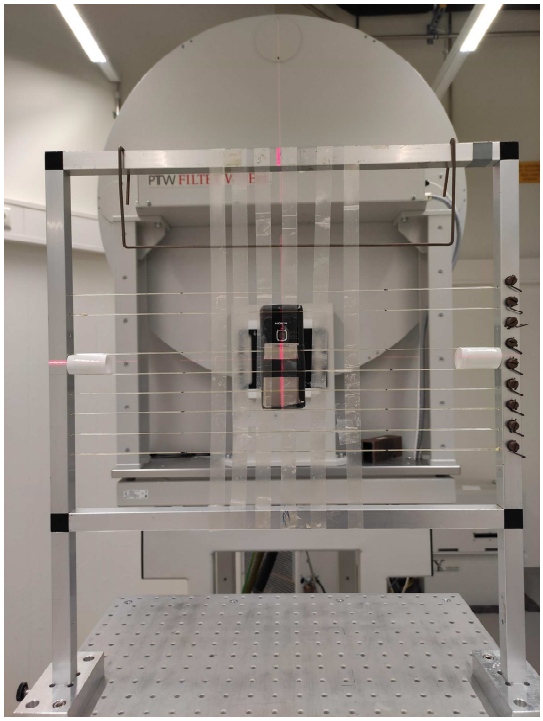

Figure 3.9: Experimental setup for a mobile phone frontal irradiation with X-rays source MG160 at the Helmholtz Zentrum München radiation facility.

3.3.2 Buchler Gamma source OB20

The radiation facilities of the Helmholtz Zentrum München are also equipped with an Amersham Buchler OB20 gamma irradiator (see Fig.3.10). The irradiator unit consists of seven ^{137}Cs and five ^{60}Co sources with different activities and dose-rates. A software allows to control the opening time of the selected source, which is transported to the irradiation position through a pneumatically controlled system. The samples can be placed in front of the shutter on a calibration bench which is 8 meters long. The fixed collimation results in a circular radiation field with a diameter of 35 cm at one meter distance (Greiter et al. 2016), The calibrated air kerma rates include the rates from 4 mGy h^{-1} to 20 mGy h^{-1} for ^{60}Co and 4 mGy h^{-1} to 2 Gy h^{-1} for ^{137}Cs at one meter distance.

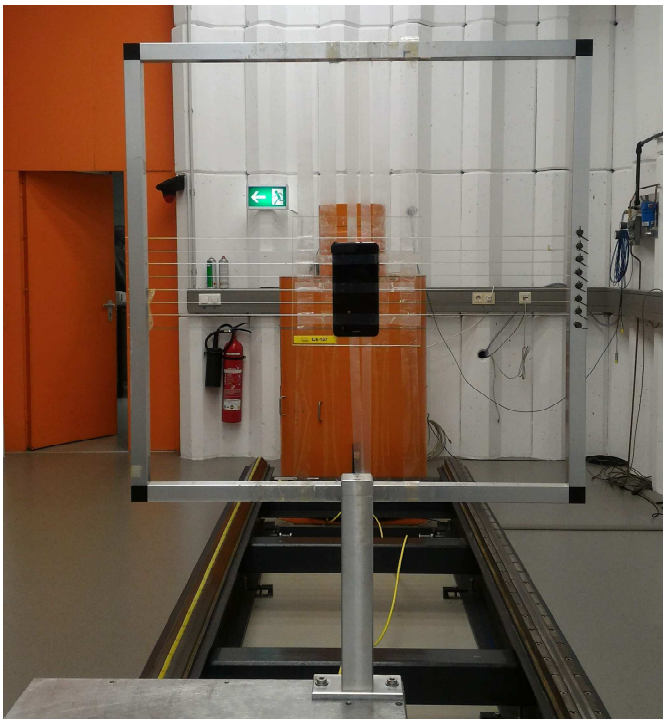

Figure 3.10: Experimental setup for a mobile phone frontal irradiation with gamma irradiations at the Helmholtz Zentrum München radiation facility.

4. Experimental results and discussion

The fourth chapter reports on the experimental procedures, results and data analysis for both research topics of the present work. In particular, section 4.1 and subsequent subsections are related to “RadioactivityCounter” characterization measurements, necessary to assess the quality of its performances in detecting dose-rates. Studies on dose-rate response, estimation of background radiation when using different devices, and energy and angular dependence were performed. Section 4.2 and following subsections refer to the experimental development of the new RTL protocol on single extracted resistor and the overall process of validation of the protocol for reconstructing doses below 100 mGy.

4.1 Characterization of the App “RadioactivityCounter”

Before starting the application, the sensor of a phone was completely light shielded by fixing induct tape and aluminum foil on top of the sensor, as shown in Fig. 4.1.

Figure 4.1: XIAOMI Mi back camera shielded from visible light with black tape.

As reported in subsection 3.1.2, when "RadioactivityCounter" is launched on a device for the first time, an automatic procedure for determining the noise level "*n*" is initialized. From the study of Gröber & al. (2014) , the *n* level is set in such a way that the amount of events due to ionising radiation is optimal compared to the amount of events due to the thermal noise of the CMOS sensor.

Therefore, the app provides the noise *n* of a device as a threshold above which any events are recognized and classified as radiation-induced. The higher the *n* level, the higher the number of counts above the threshold required to attribute an event to ionising radiation exposure. As a result, the noise value actually affects the dose-rate sensitivity of the camera of a device. In a first step, the procedure of assessing the *n* value was carried out under no special conditions, as people would normally do. Considering that *n* is device specific, a clear distinction was observed among phones equipped with cameras of different image qualities. Inexpensive models showed *n* values close to 10, whereas for more pricey phones in the range above 200 €, equipped with higher quality CMOS sensors, a threshold value below ten was assessed. Such *n* value differences suggested differences in terms of sensitivities. Consequently they were explored with the dose-rate responses study described below.

4.1.1 Dose-rate responses

As was anticipated from the noise level considerations described above, from the paper of Mafodda & Woda (2020): "phone models with $n < 10$ showed a linear trend in dose-rate response starting from 5 μGy h^{-1} for an integration time of 10 min. Moreover, extending the integration time resulted in an overall enhancement of the performance at low dose-rates.". Measurements that were integrated over one hour resulted in a linear dose response starting already from 2 μGy h^{-1}. As an illustrative example, Fig.4.2 shows the dose rate response of an iPhone 6S, characterized by a noise level value of 2.5.

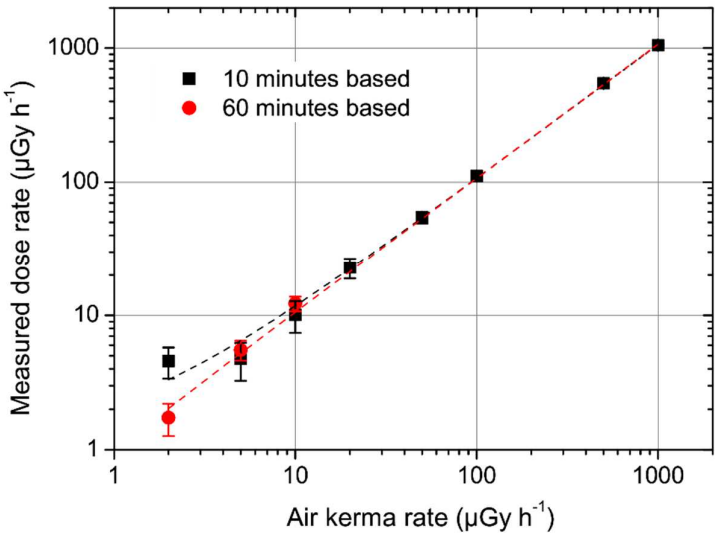

Figure 4.2: Measured dose rate using an iPhone 6S. Error bars represent standard errors. (Mafodda & Woda, 2020).

In the figure, the black line represents a straight line fitted to the ten minutes measurement, using the individual uncertainties as weights. The red line refers to a straight line fitted to the sixty minutes measurements up to a dose rate of 10 µGy h^{-1} and to the ten minutes measurements for higher air kerma rates, again using the individual errors as weights. Note that for dose rates above 20 µGy h^{-1} 10 minutes of integration time were sufficient from a statistical point of view, thus 60 minutes based measurements were not performed.

The fit equation is:

$$y = (1.067 \pm 0.04)x - (0.1 \pm 0.3) \tag{4.1}$$

Where x denotes the nominal and y the measured dose rate. Only for iPhone models the app "RadioacitivityCounter" has a built-in calibration and therefore permits to directly compare measured and nominal dose rates. However, overall also for all other models with n<10, extending the integration time up to one hour improved the performance down to 2 µGy h^{-1}. Count-rate responses, in terms of counts per minute, of other phone models are reported in Fig. 4.3.

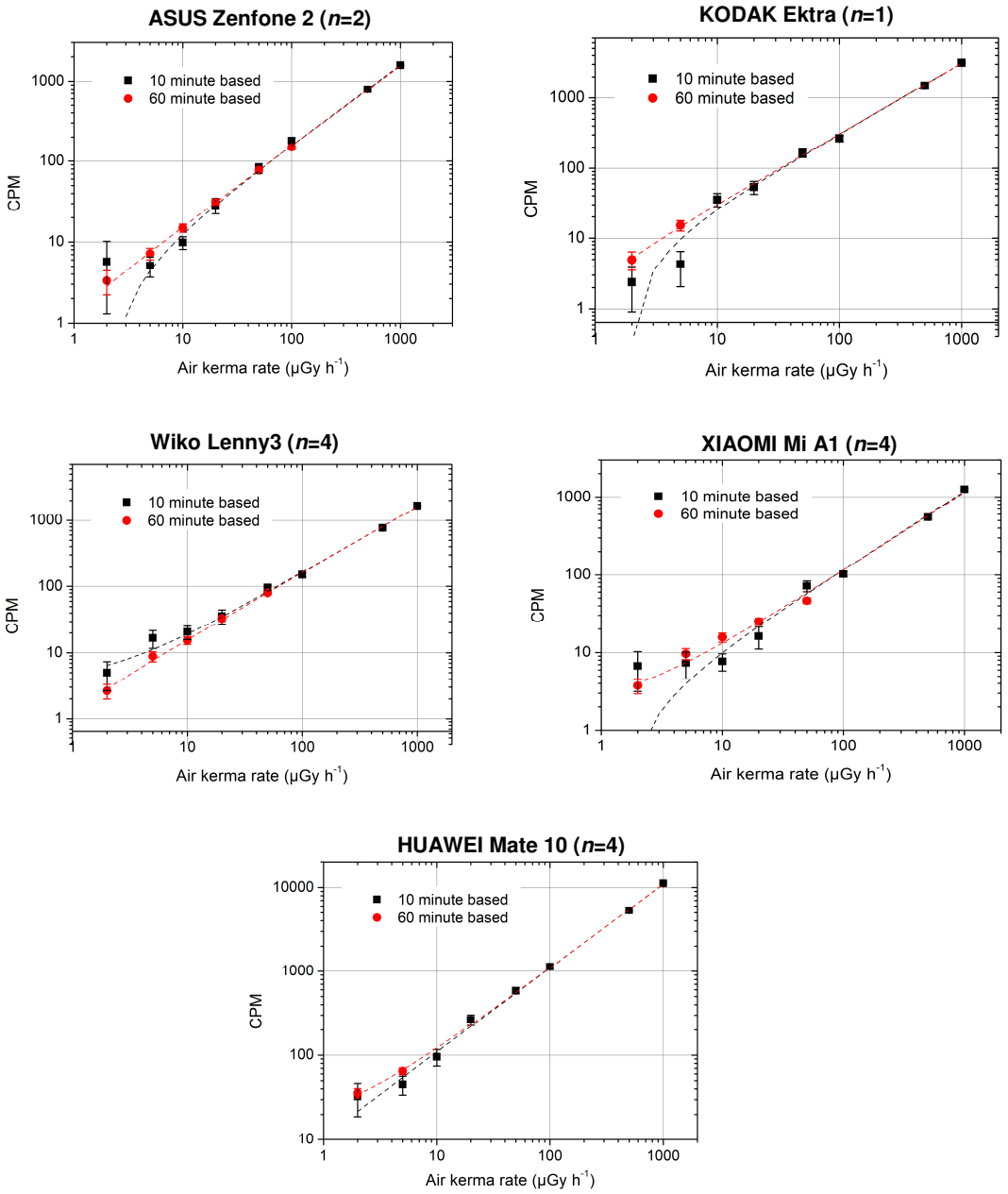

Figure 4.3: Dose rate response of different phones characterized by a low *n* level. They were all Android based models, therefore on the y-axis are represented their "Counts Per Minute" (CPM). (Mafodda & Woda, 2020)

During extended measurements, the distribution of counts per minute displays a skewed shape due to a pronounced number of "zero" events and only a few count rates above zero being registered. This is shown in Fig. 4.4 for an iPhone 6S and iPhone 7, irradiated at 2 μGy h^{-1} for one hour.

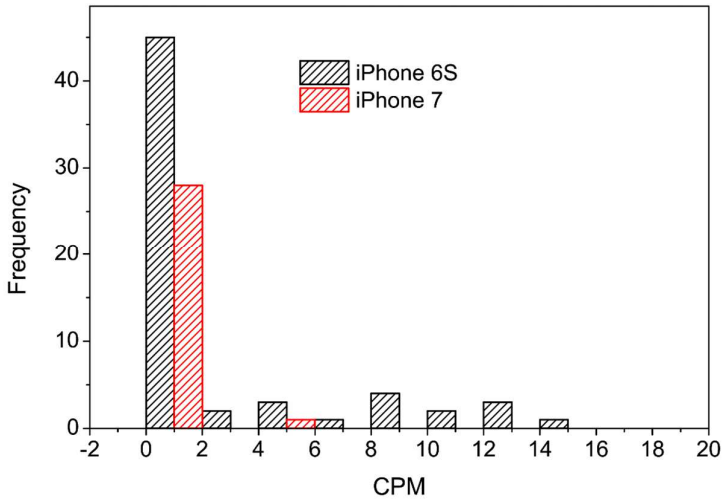

Figure 4.4: Distribution of count rates detected with iPhone 6S and iPhone 7 at 2 μGy h^{-1}; CPM – counts per minute (Mafodda & Woda, 2020).

A possible reason for this behavior can be the software implemented in the smartphone for correction of images. The software compares signal intensity in adjacent pixels. If an exceptionally high signal in one of the pixels is observed, this is identified as an error and the value in that pixel replaced by the values of the neighboring pixels. In the case of several events occurring in adjacent pixels, the error identification is unsuccessful explaining the few bins with higher count rates that can be seen in the histogram of Fig. 4.4. As stated in Mafodda & Woda (2020):"For sufficiently high dose rates the algorithm cannot cope with the pixel pattern of the camera and gives the uncorrected (true) values as output… For phone models with noise level higher than 10, a linear trend in dose-rate response was only observed above 20 μGy h^{-1}, suggesting that optical specifications of the sensor are not optimized for detecting ionising radiations at lower dose-rates."

In Fig. 4.5, the black and red lines represent straight lines fitted to the ten and sixty minutes measurement, respectively, using the individual uncertainties as weights.

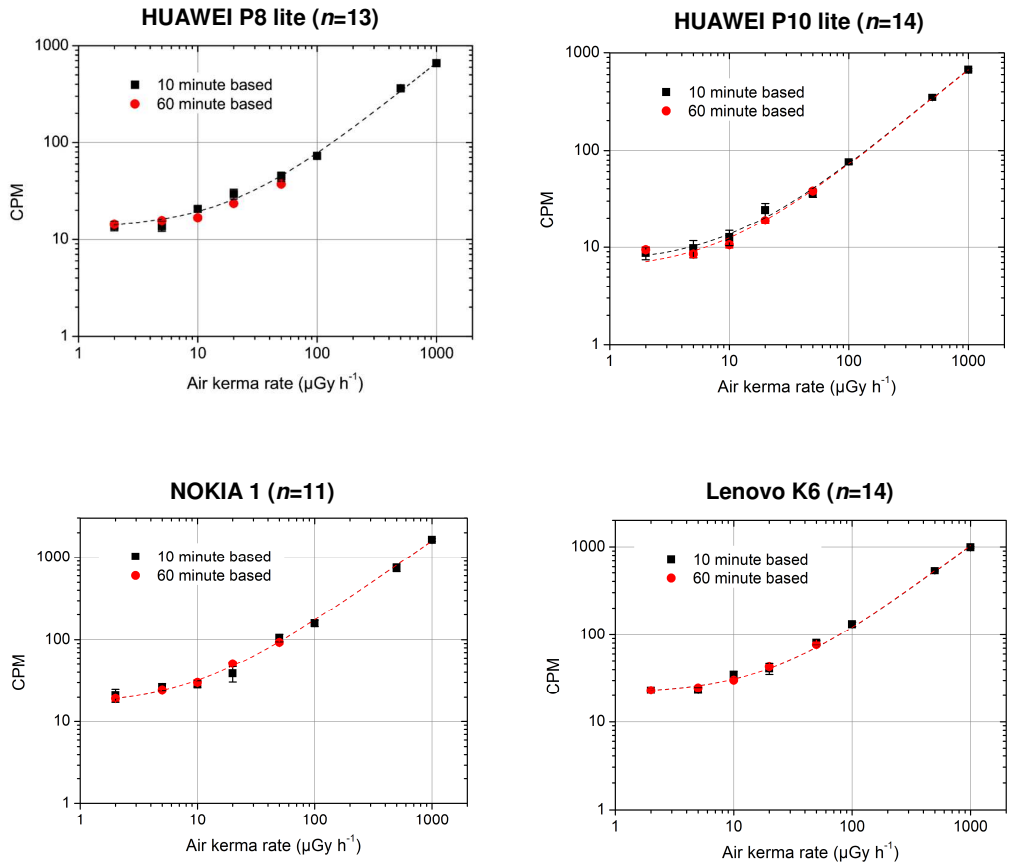

Figure 4.5: Dose rate response of different phones characterized by a high *n* level. Again, on the y-axis are represented "Counts Per Minute" (CPM). (Mafodda & Woda, 2020)

In this case, sensor noise dominates the count rates in the dose rate region below the threshold value leading to an approximately normal distribution , as depicted in Fig. 4.6. The latter represents counts detected with a HUAWEI P10 lite (*n*=14) irradiated at 2 µGy h^{-1} for one hour.

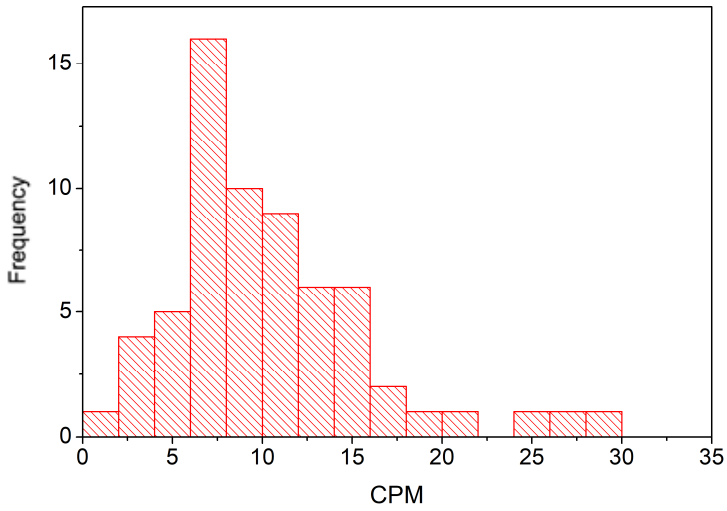

Figure 4.6: Distribution of count rates detected with HUAWEI P10 lite at 2 µGy h^{-1}; CPM-counts per minute (Mafodda & Woda, 2020).

Therefore, for this category of phones, increasing the integration time to sixty minutes overall does not improve the measurement of lower dose rates with this application. Furthermore, another factor that might affect the sensor noise, is the sensor temperature. Thus the reliability of the app performance likely depends on whether and how much the sensor overheats during a measurement.

For one phone model tested, the ASUS Zenfone 2, detected count rates were recognized to exponentially increase with time, as shown in Fig. 4.7.

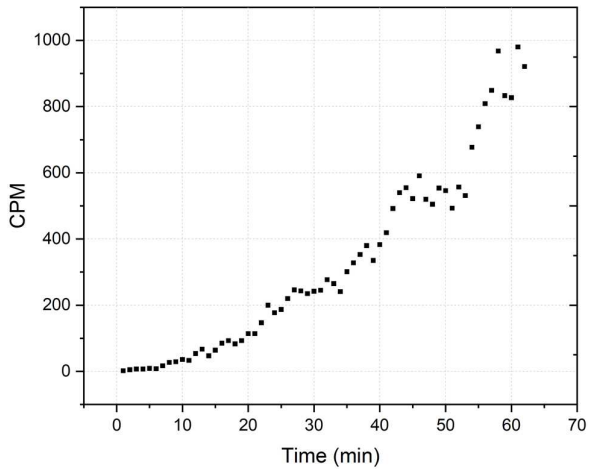

Figure 4.7: ASUS Zenfone 2 counts detected at background level when sensor temperature rises.

In this specific case, the recorded temperature of the sensor also increased by 10°C during the measurement. Since the output file produced by the software for Android based phone models contains also information about the sensor temperature, in principle, any faulty tendency can be identified and eventually corrected.

4.1.2 Background assessment

In light of the previous results, the measurement of lower dose-rates (< 20 μGy h^{-1}) required long integration time up to one hour, which represents a limitation for practical applications. An alternative approach to potentially improve the performance of the software at such low dose rates in a more reasonable measurement time (e.g. ten minutes), could be a quantitative noise assessment in an environment where the level of natural radioactivity is reduced. To achieve this, five selected models were put in a "custom-made lead shielding, with additional inner layers of electrolytically refined copper and plastic (dose rate of ~ 20 nGy h^{-1}) while running the noise assessment procedure" (Mafodda&Woda, 2020; see Fig. 4.8).

Figure 4.8: Lead shielding of the Luminescence laboratory at the Institute of Radiation Medicine of the Helmholtz Zentrum München used to achieve a reduced background dose-rate during the noise assessment procedure.

A new measurement of the different dose rates was performed afterwards. As illustration, the results obtained with the iPhone 6S are depicted in Fig. 4.9.

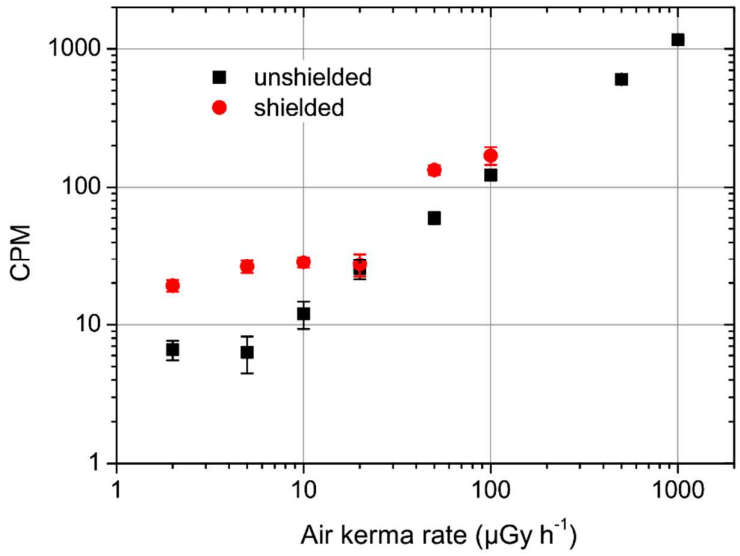

Figure 4.9: iPhone 6S CPM (counts per minute) "detected at different air kerma rates after assessing the background in shielded (n=1.3) and unshielded conditions (n=2.5)" for integration times of 15 minutes (Mafodda & Woda, 2020).

Figure 4.9 demonstrates that the performance in the lower dose rate region does not improve compared to the unshielded measurements. As reported in Mafodda & Woda (2020): "Shielding the phone from the natural radioactivity leads to a lower noise level (counting threshold) being assessed and thus to an increase of the registered counts per minutes for the same nominal dose-rate. However, the performance in the lower dose rate region does not improve compared to the unshielded measurements. For phone models phone models with an initial higher noise level (n >10) at normal environmental background, count rates are already dominated by the sensor noise." Consequently, the background assessment in the lead shielding gave similar results as the previous dose-rates response study.

4.1.3 Energy dependence

A previous study from Van Hoey et al. (2016) on the same "RadioactivityCounter" app installed on four different iPhone 4 models, showed a pronounced dependence of the signal on the energy of the ionising radiation. In particular, the relative responses to ^{60}Co showed an over response varying from 4 for 24 keV up to about 10 for 65 keV.

The reason is that a CMOS sensor is made of non-tissue equivalent materials. In this work, a systematic energy dependence study was completed on a total of ten phone models. Responses of the sensors were converted from air kerma to ambient dose equivalent H*(10) using conversion coefficients tabulated in ISO (1999). The latter unit is the reference quantity used in environmental monitoring. Moreover, responses were normalized to the response at a photon energy of 662 keV for the same air kerma-rate of 1 mGy h^{-1}. Regardless of the specific model and type of CMOS sensors, all smartphones displayed a relative response of up to a factor of 11 at photon energies around 60 keV.
This corresponds to an over-response of a factor of ~18 with respect to air kerma. See Fig.4.10 for an example.

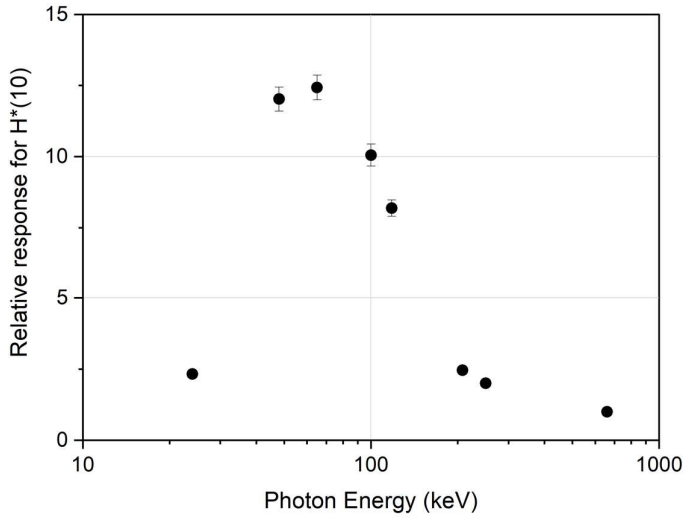

Figure 4.10: Energy response in terms of H*(10) relative to ^{137}Cs for one representative phone model, iPhone 6S, showing the highest over response at 60 keV photon energy (Mafodda & Woda, 2020).

Figure 4.11 compares the relative response for H*(10) for two phone models (ASUS Zenfone 3 and Lenovo K6) using the same sensor type.

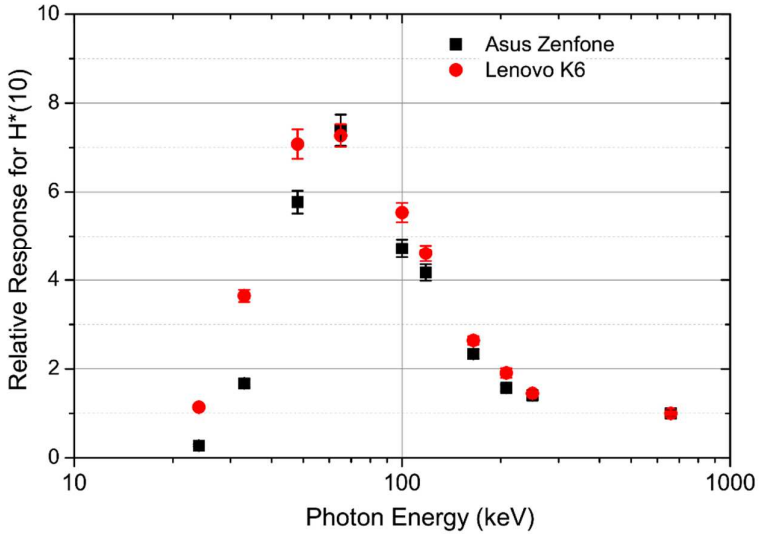

Figure 4.11: Energy response in terms of H*(10) relative to ^{137}Cs for the ASUS Zenfone 3 and Lenovo K6, mounting the same type of sensor.

A similar response was observed, which was to be expected. Another study regarded the direct comparison of the photon energy response of the front and back cameras of the iPhone 6S. The cameras in question did not show any substantial difference when irradiated frontally ("facing the source" configuration), as shown in Fig. 4.12.

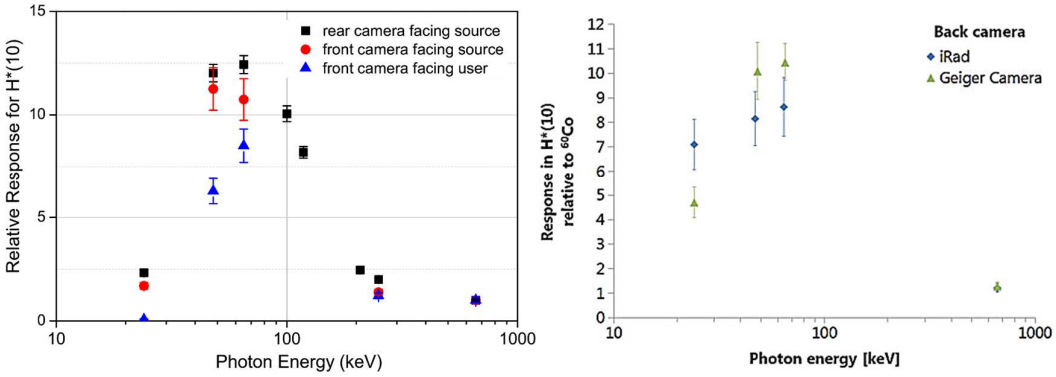

Figure 4.12: On the left, energy response in terms of H*(10) relative to ^{137}Cs for iPhone 6S using back and front cameras (Mafodda & Woda, 2020); on the right, energy response in H*(10) relative to ^{60}Co of different applications installed on iPhone 4S by Van Hoey (2016). Camera facing user corresponds to an angle of 180° with respect to the radiation source.

As stated in Mafodda & Woda (2020): “When the front camera was turned away (180°) from the source, a slightly improved (i.e. reduced) energy dependence was observed, due to shielding effects. However, for the models tested, this advantage is compensated by the disadvantage of a reduced sensitivity of the front camera sensor. For the back camera, the peak over-response observed is somewhat higher but still similar to the range of values reported in Van Hoey et al. (2016). For the front camera, both the degree of over-response as well as the overall shape of the response curve are markedly different between both studies, possibly due to developments in sensor types and lens thicknesses”. It is noted that in case of unplanned exposures due to a nuclear power plant accident, the major gamma-emitting radionuclides released and deposited would emit photons with energies >350 keV, for which the energy response is close to unity. However, on the short time scale after an incident, radionuclides with a short half-life and emissions below 300 keV could also contribute to the radiation dose (IAEA 2017; UNSCEAR 2008). As an additional factor, surface roughness could result in scattered and backscattered radiation, leading to a notable contribution of photons with lower energies (Petoussi-Henss et al.,2012). For any such as scenario where photons of lower energy can be expected, figures such as Figs. 4.10, 4.11 and 4.12 can be consulted to see if a correction has to be applied.

4.1.4 Angular response

In order to assess the performance of “RadioactivityCounter” on the direction from which the ionising radiation comes from, four phones were irradiated at the radiation facilities of the Helmholtz Zentrum München with photons of 662 keV of a ^{137}Cs source from different incident angles (Fig. 4.13). More specifically, an orientation of 0° corresponded to the back camera facing the source, while the orientation of 180° was associated to the configuration of the camera turned away from the source. In the paper of Mafodda & Woda (2020) the following is reported: “in good agreement with previous studies (Cogliati et al., 2014; Van Hoey et al., 2016), the data showed an overall variation of the measured signal with a maximum variation of about 10%”. A sharp decrease in the counts recorded by the CMOS sensor resulted when the phone was irradiated from an angle of 90° due to the shielding effects of the smartphone structure itself as well as due to the reduced exposure condition of the sensor’s active area.

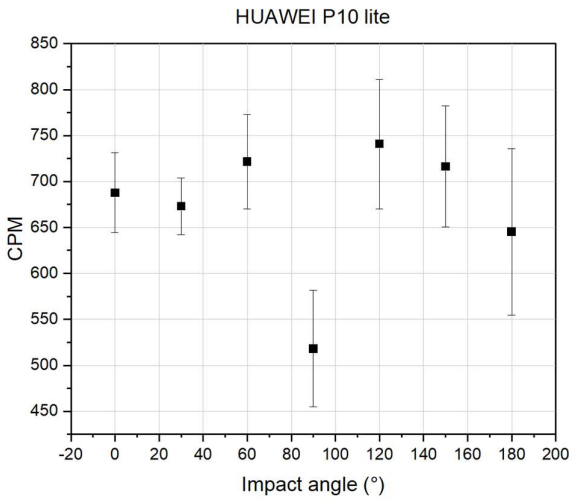

Figure 4.13: Illustrative example of a HUAWEI P10 lite phone model irradiated from different incident angles at 1 mGy h^{-1} with ^{137}Cs source. Measurements were integrated over 10 minutes (Mafodda & Woda, 2020).

4.1.5 Calibration factors

As stated in section 3.1.2, the Android version of "RadioactivityCounter" app can be calibrated by using appropriate calibration factors listed on the developer's company website. However, the list published there (accessed November 2021) included phone models mainly out of date, and values for modern smartphones, as the ones tested in the present work, were in November 2021 not available. In this respect, the present study contributed to add new calibration factors that can be helpful for the future use of the app in real cases. In fact, through a menu section named "Adjust", the user might manually insert calibration coefficients that allow the conversion from Counts Per Minute (CPM) into doserates values (Fig. 4.14).

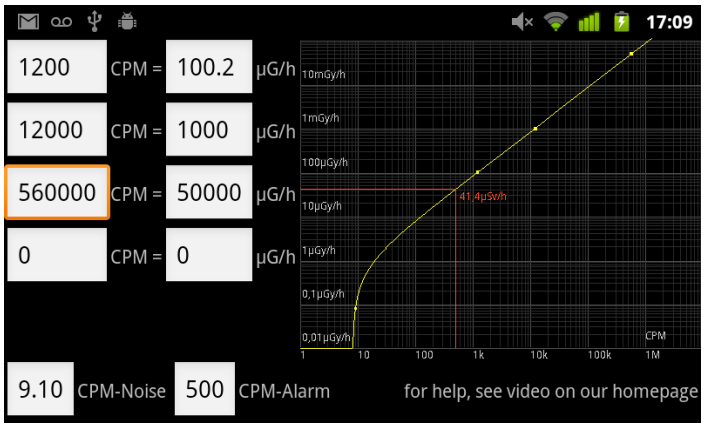

Figure 4.14: "RadioactivityCounter" "Adjust" menu and calibration curve.

All the coefficients produced in the present thesis are reported in Table 4.1, except for the ones of two models (Motorola E4 and ZTE Blade L5 plus) which showed a malfunction during the tests and did not did not guarantee the same data quality.

Brand	Model	CPM for 50 μGy h^{-1}	CPM for 500 μGy h^{-1}	CPM for 1000 μGy h^{-1}
APPLE	iPhone 6S	60	603	1165
ASUS	Zenfone2 Z00AD	476	1865	3620
ASUS	Zenfone3 ZE520KL	82	791	1577
HUAWEI	P8 lite 2017 PRA-LX1	45	363	660
HUAWEI	P10 lite WAS-LX1A	36	345	671
HUAWEI	Mate 10	585	5311	11229
KODAK	Ektra	166	1491	3148
LENOVO	K6	80	531	993
NOKIA	1	105	749	1640
WIKO	Lenny3	95	770	1672
XIAOMI	Mi A1	72	548	1256

Table 4.1: List of conversion factors obtained in the present study that can be used to produce calibration curves. Counts per minute (CPM) at 50, 500 and 1000 μGy h^{-1} are given (CONFIDENCE Deliverable 9.8, Mafodda et al., 2019a).

4.2 Experimental results of RTL

The following sections report on the experimental work aimed at developing a new retrospective dosimetry protocol based on the red Thermoluminescence emission from surface-mount resistors. In particular, investigations focused on evaluating the dosimetric properties of the alumina substrates of a single resistor extracted from the circuit board of mobile phones. Results from sample preparation procedures for protocol optimization in recovering low doses (< 100 mGy) are hereby presented and discussed. Further objective of this thesis was to identify possible source of uncertainties, such as confounding signals intrinsic to the material (zero-dose), signal loss with time (anomalous fading), and uncertainty related to the instrumentation used.

The protocol was then tested on intact mobile phones irradiated at doses from 20 mGy to 100 mGy with a ^{137}Cs gamma source to reproduce the scenario of an unplanned exposure.

4.2.1 RTL measurement protocol

Most of the studies found in the literature state that surface-mount resistors analyzed with the optically stimulated luminescence (OSL) technique do not require any preparation with special chemical treatment. In contrast, the paper of Ademola and Woda (2017) indicates that for Thermoluminescence in the blue wavelength range, samples have just to be cleaned in an ultrasonic bath with acetone for 20 minutes after the extraction in order to remove any residual of the adhesive mask used by the manufacturers to secure the components on the boards. Such a process of cleaning, avoids that other substances present on the surface of the target material might affect the resulting TL signal. In fact, in the specific case of resistors, adhesive leftovers on the alumina substrates can oxidize during the heating process of the sample and might generate dark zones leading to a loss in sensitivity. The fact that measurements are carried out in a highly enriched N_2 atmosphere (see chapter 3) minimizes this effect but cannot completely avoid it. In a first approach, the recommended cleaning procedure with acetone was followed. In order to check for the cleaning efficiency, preliminary measurements of the reproducibility of the RTL signal were carried out on two types of components: resistors extracted from circuit boards of mobile phones, possibly characterized by the presence of soldering mask residuals, and resistors from a commercially available sample kit, alumina substrates of which are adhesive free. Several cycles of irradiations either at 1 Gy or 400 mGy and subsequent RTL measurements were performed.

TL signals were integrated between 125°C and 180°C, and a systematic and continuous decrease in sensitivity was observed as shown in Figs. 4.15 (a) and (b).

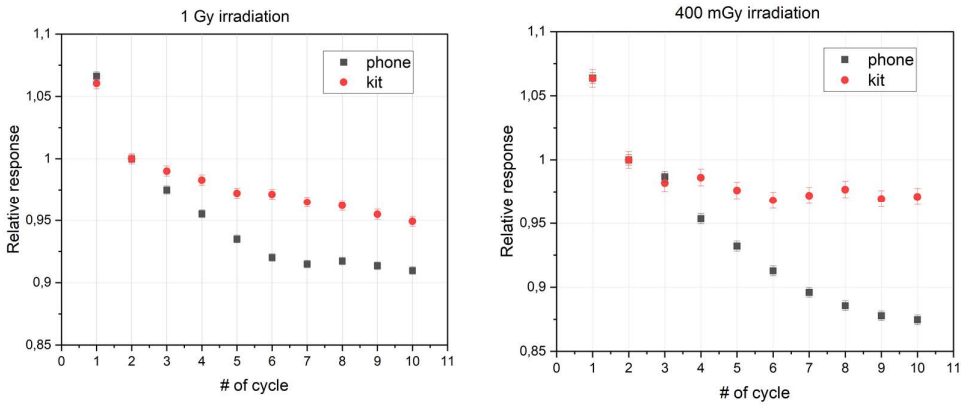

Figure 4.15: Change in RTL signal sensitivity with repetition of the cycles "irradiation - RTL signal measurement" performed on resistors extracted from phones (black dataset) and from commercial sets (red dataset). The applied dose was 1 Gy (left panel) and 400 mGy (right panel) and data are normalized to the second cycle.

The decrease in sensitivity was more pronounced for samples extracted from the phones (up to 10%), which is attributed to a possible ineffectiveness of the cleaning procedure used at that time. Therefore, new cleaning procedures were explored, such as leaving the extracted samples in acetone for a longer time (durations 40 and 60 minutes).

This approach did not lead to any consistent improvement, as the sensitivity continued to decrease with the same trend as observed before (up to a maximum of 13%). Beside acetone, other solvents were considered as well. The choice fell on Methyl Ethyl Ketone (MEK) and propanol, since both are commonly used in printed circuit board (PCB) cleaning and rework. In addition, the reproducibility tests shown in Fig. 4.15 highlighted that the most pronounced sensitivity change (5-6%) occurred after the first readout. A similar observation was made for resistors measured with blue Thermoluminescence (Ademola & Woda, 2017), and for inductors (Woda et al., 2011), where the effect was attributed to a possible phototransfer from deeper traps when samples are exposed to white light (Beerten et al., 2009). Therefore, the following sample preparation was performed in subdued red light conditions. This change in lightning combined with the cleaning procedure with new solvents, lead to the results shown in Fig. 4.16:

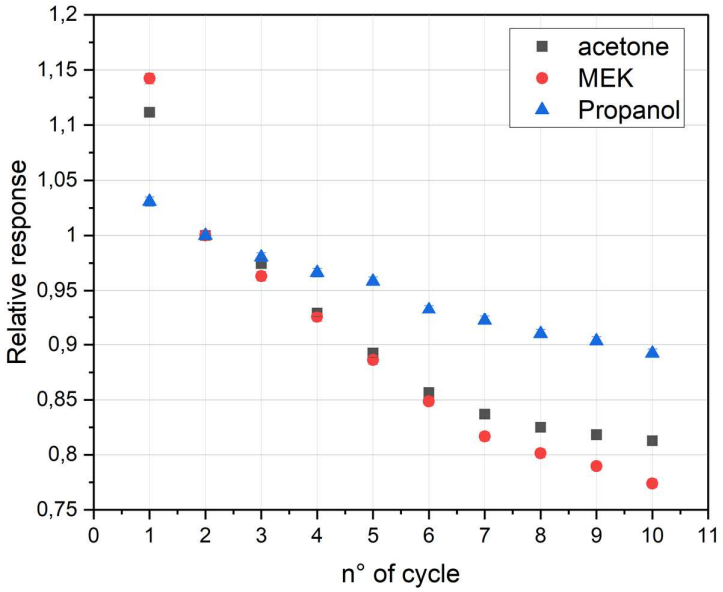

Figure 4.16: Change in RTL signal sensitivity with repetition of the cycles "irradiation - RTL signal measurement" performed on resistors extracted from phones and cleaned with different solvents: acetone (black squares), Methyl Ethyl Ketone (MEK - red dots) and propanol (blue triangles). The applied dose was 1 Gy. Data are normalized to the second cycle.

As it can be seen from Fig. 4.16, cleaning with propanol resulted in the least decrease in sensitivity during the repeated cycles of irradiation and RTL measurements. On the other hand, propanol did not prevent the sensitivity decrease observed during the repetitions of the cycles. From literature, studies on other materials (e.g. quartz) (Zhi-Young et al., 2000) highlighted how changes in sensitivity might also be attributed to the temperature of read out of the luminescent signal. Thus the RTL measurement protocol was further modified by lowering the read out temperature of the TL signal from a previous value of 400°C down to 350°C. Figure 4.17 illustrates the results of the protocol assessed for single resistors, with the combination of the subdued red light conditions during all the phases of sample preparations, the cleaning procedure with propanol and the RTL signal read out at a maximum temperature of 350°C.

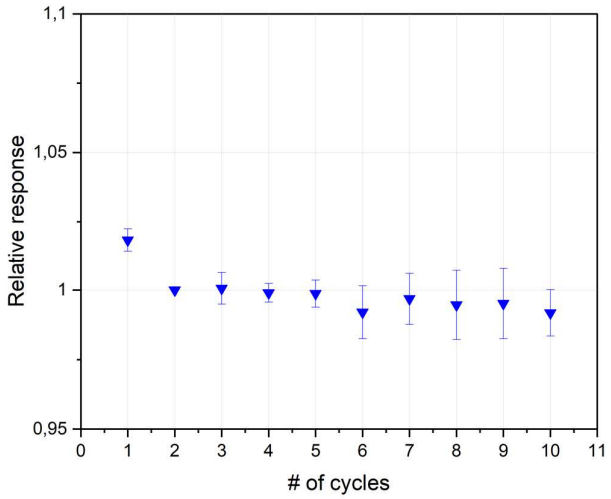

Figure 4.17: Reproducibility test performed after preparing extracted resistors in subdued red light conditions, cleaned with propanol and read out by heating the samples up to T=350°. Samples were irradiated at 1 Gy. Error bars represent standard deviations from three sets of data. Data are normalized to the second cycle.

The first signal read out swill shows a variation in sensitivity in the order of 2%, but the subsequent cycles are rather constant. Any other minor variations observed from the 7th cycle on, might be ascribed to internal processes occurring in the material. A first evaluation of the protocol was performed through several dose recovery tests using single resistors extracted from the circuit board of Samsung phone model of 2011. For those tests, the built-in beta source of the reader was used for irradiation with both, the doses to be reconstructed and the calibration doses (Table 4.2).

Given Dose [mGy]	Recovered dose [mGy]	Error
1200	1170.37	±3,36
500	533.59	±6.16
200	216.50	±5.64
120	123.87	±6.58
80	85.65	±2.35
60	86.76	±3.90
40	50.72	±3.19

Table 4.2: Doses reconstructed with RTL measurement on single resistor. Errors are assessed by choosing the larger value provided by weighted and unweighted linear fit (see text and Appendix B).

Individual errors on doses were calculated from both the scatter of the data respect to the calibration curve and by the error propagation of the parameters of the linear fit (see Appendix B). An example of a calibration curve is given in Fig. 4.18.

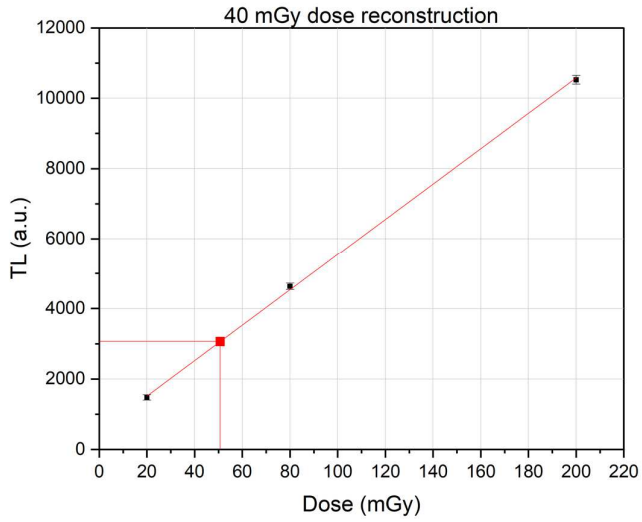

Figure 4.18: Example of calibration curve for reconstructing the 40 mGy dose shown in Table 4.2.

For the dose region from 1.2 Gy down to 80 mGy (Table 4.2), the average difference between nominal and given doses is 3.8%. In contrast, as reported in the CONFIDENCE Deliverable 9.10:"for the lowest two doses tested (40 and 60 mGy), the deviation increases up to ~50% or, in absolute terms, to ~25 mGy. The comparison of the calculated errors with the observed deviation in table 4.2 implies that the true uncertainties are underestimated" (Mafodda et al., 2019b). One possible reason for the large overestimation of lower doses will be explored in the following section.

4.2.2 Offset time of the beta source

In order to optimize the RTL measurement protocol for the dose assessment of low doses with one resistor, the origin of a possible confounding effect was investigated. Every RTL measurement of an unknown dose is derived from a linear fit of a calibration curve, as shown for the example in Fig.4.18.

Every point of the curve corresponds to a given dose to the sample, irradiated with the built-in calibration beta source of the luminescence reader characterized by a dose-rate of approximately 20 mGy s^{-1}. Therefore low doses of 20, 40, and 60 mGy are equivalent to short irradiation times of 1, 2 and 3 seconds respectively. The mechanical action of opening/closing the beta source is not instantaneous: the circularly arranged $^{90}Sr/^{90}Y$ source capsules are "opened up" by the shutter in a step-by-step process. Thereby, the sample might already be exposed before counting of the "irradiation time" starts. In this work, the additional dose due to such an offset time of the beta source intrinsic to the instrumentation was evaluated and taken into account in the dose reconstructions described in the following sections. Specifically, the irradiation time offset of the reader was estimated as the intercept of the calibration curves for very short irradiation times (e.g. 1, 2, 3 s), by carrying out experiments on both resistors from commercially available kits and crystalline dosimeters made of A_2O_3:C (TLD-500). An illustrative example is shown in Fig. 4.19. Overall an average value of (0.27±0.11)s was assessed, in line with the value assessed by Kalchgruber et al.,2002, corresponding to an offset dose of (5.4 ± 2.3)mGy.

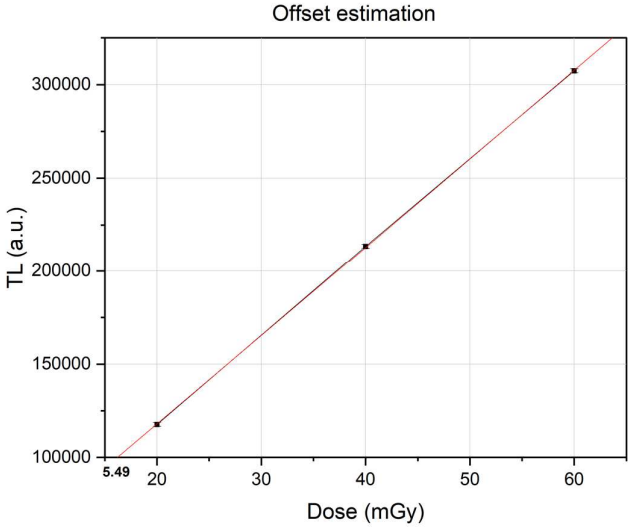

Figure 4.19: Illustrative example of the offset time reconstruction performed within this work. As stated in the text, the calibration curve is related to irradiations on a TLD-500.

4.2.3 Zero dose

One of the dosimetric properties of the alumina substrates of resistors is the existence of a strong native signal measured in unexposed samples, the so called “zero dose” signal. The latter was observed for the first time by Beerten at al. (2009), who performed TL measurements on resistors extracted from a Sony flash drive. Ademola and Woda (2017) reported similar observations after investigations carried out on resistors extracted from a variety of mobile phones. A possible explanation for this signal is stated in Ademola & Woda (2017) as the following:”lies in the black overcoat of the thin film resistors, which is made up to 75% of an epoxy resin”. From the same paper: “if the epoxy is cured by UV light, similar to the transparent encapsulations of chip cards (Woda et al., 2009), then this exposure might also generate electron-hole pairs in the ceramic itself and thus lead to the formation of latent TL signals”. The zero dose signal is present in the high temperature range (250°C- 400°C) of the TL glow curve (Fig. 4.20). Although the radiation-induced TL signal continues beyond 200°C, the existence of such a confounding factor limits the possibility to calculate the TL signal by integrating up to 200°C.

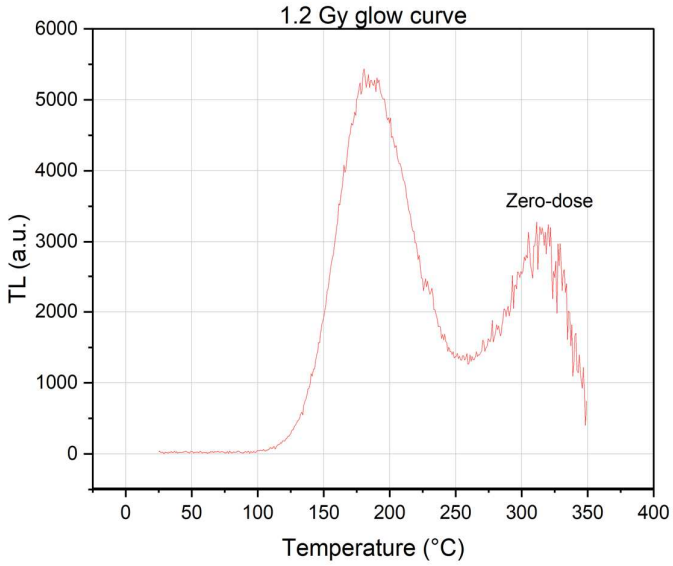

Figure 4.20: Glow curve of a single resistor irradiated with 1.2 Gy with the built-in beta calibration source of the luminescence reader (heating-rate of 2°C s^{-1}). The dosimetric signal peaks at 180°C, whereas the zero dose signal peaks at 320°C.

The presence of the zero dose signal could affect the measurement protocol developed within this work. If the relative intensity of the zero dose signal is not homogeneously distributed among the resistors in a phone, sampling at a single resistor level could result in accidentally picking a component characterized by a high intrinsic background signal. Previous TL investigations in the literature were carried out on groups up to 10 aliquots at a time, where non-homogeneities are expected to average out.

Therefore, efforts were made in this thesis to evaluate the distribution of zero-dose within the same phone model and between different phone models. First, the homogeneity among components extracted from different positions of the same circuit board was assessed on a Samsung Galaxy Trend Plus. A total of 16 samples were extracted from the top, middle and bottom part of the circuit board, depending on the availability of components in those parts (Fig.4.21).

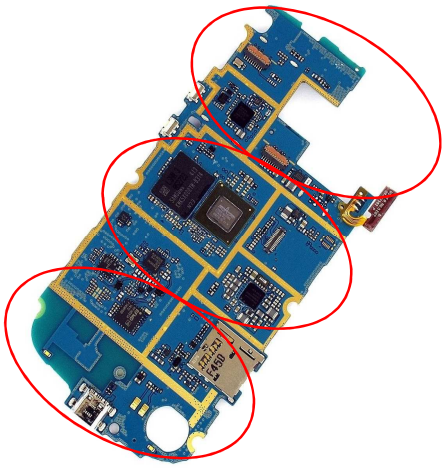

Figure 4.21: Samsung Galaxy Trend Plus circuit board.

Position	Zero dose [mGy]	Error [mGy]
top	2.02	±2.87
	-1.27	±4.95
	2.15	±3.51
	2.05	±4.96
	7.38	±3.39
	8.31	±12.67
	72.27	±3.21
middle	-1.66	±6.54
	-7.65	±4.26
	-7.89	±3.67
	7.47	±6.16
	-0.32	±3.34
down	1.38	±3.82
	4.12	±4.39
	10.10	±3.60
	61.75	±3.33

Table 4.3: Results of the zero doses obtained for the three regions shown in Fig. 4.21.

The zero doses in table 4.3 were calculated from the intercepts on the x-axis of the calibration curves, while the errors were estimated from the unweighted linear fits (see Appendix B). A bias induced by the instrument required a specific correction, which is discussed in more detail at the end of the chapter.

The offset value of (5.4 ± 2.3) mGy reported in section 4.2.2 was added to all zero doses. Overall, two samples showed a zero dose of (72.27±3.21) mGy and (61.75±3.33) mGy. For the remaining 14 samples the difference between measured dose and zero was statistically not significant, and lead to an average of (1.91± 5.53) mGy. Furthermore, zero doses from resistors extracted from four different phones were also evaluated. For this, other 23 samples in total were picked from a ZTE Blade L5, a NOKIA 5250, a Samsung Galaxy Fame and a HUAWEI. Results were in line with the previous experiment, and only one sample from the HUAWEI model showed a strong zero dose of (181±12) mGy. Therefore, for the majority of samples possible zero dose were below the detection limit (2σ ~ 10 mGy) and thus considered negligible, but the possibility of sampling resistors with a strong native signal cannot be fully excluded. Consequently, the retrospective dosimetry method on one single resistor developed within this work might not be considered as a standalone standard but as a part of a multi-technique approach.

4.2.4 Fading

The TL dosimetric signal from resistors has been observed to be subject to a pronounced fading with time (Beerten et al., 2009). In most of the case of unplanned exposures dose assessment will take place days or even weeks after the accident (ICRU 2019). Hence, the knowledge of how the signal fades with time is crucial for a proper dose reconstruction. The origin of the time-dependent loss of signal is the phenomena of anomalous fading already addressed in chapter 2. For chip cards and electronic components the functional relationship between intensity and time since irradiation is described by the following equation (Huntley & Lamothe, 2001):

$$I = I_c \left[1 - \frac{g}{100} \log_{10}\left(\frac{t}{t_c}\right)\right] \tag{4.2}$$

Where I_c is the intensity of luminescence at some time t_c, and g is the percent decrease in intensity per decade (i.e. per tenfold increase in t/t_C). As part of the present thesis, a fading experiment was performed on 11 resistors of type 0402 (1 x 0.5 x 0.35 mm) and eight samples type 0201 (0.6 x 0.3 x 0.26 mm) extracted from circuit boards.

Samples were first annealed by a TL run up to 400°C to erase any native signal, irradiated with a beta dose of 1 Gy and then stored at room temperature in the dark for periods ranging from five minutes up to four weeks before the RTL measurement. As an example, Fig. 4.22 displays the decay curves of two resistors extracted from a Samsung Fame model.

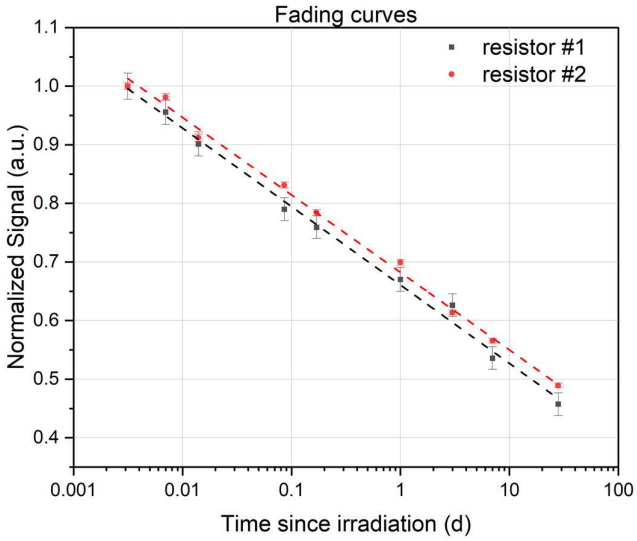

Figure 4.22: Fading of RTL signals of two resistors for different storage time at room temperature. The lines were obtained by fitting the Eq.4.2.

The percent decreases per decade g and luminescence intensity at time t_c=8.3 h are reported in table 4.4.

sample	g	I_c
Resistor #1	17.67±1.02	0.73
Resistor #2	18.64±1.15	0.75

Table 4.4: Percent decrease per decade and luminescence intensity Ic at time t_c=8.3 h for RTL integrated between 125°C-180°C.

On all samples an average value and standard deviation for g of 17.54 ± 2.74 was observed (see also Fig.4.23). This is consistent with previous blue TL study reporting a value of g = 17.63 for an integration window 125°C-200°C (Ademola & Woda, 2017).

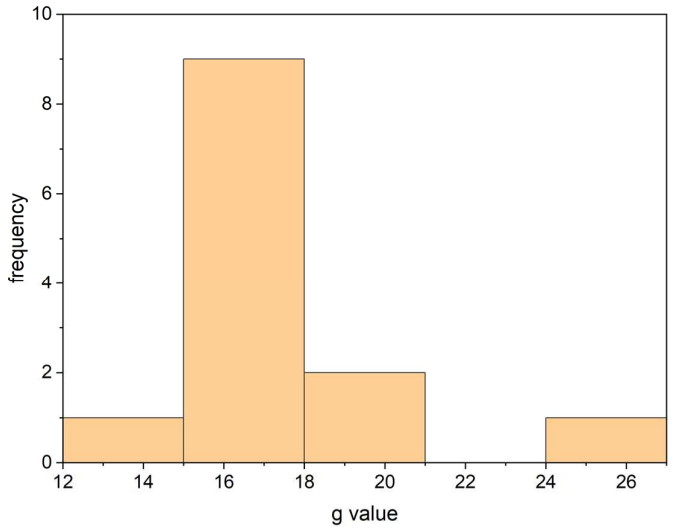

Figure 4.23: Distribution of g values among all samples

From the calculation of g, a fading correction factor and relative error for the final recovered dose were calculated following the EURADOS review paper on uncertainty assessments (Ainsbury et al., 2017).

From the Eq.4.2, introducing $k = \frac{g}{100}\ln(10^{-1})$:

$$I = I_c\left[1 - k \ln\left(\frac{t}{t_c}\right)\right] \tag{4.3}$$

The fading correction factor can be calculated as follows:

$$F = \frac{I(t_{acc})}{I(t_{cal})} = \frac{1 - k\, ln\left(\frac{t_{acc}}{t_c}\right)}{1 - k\, ln\left(\frac{t_{cal}}{t_c}\right)} \tag{4.4}$$

Where $I\,(t_{acc})$ is the signal measured after the time of the accidental exposure t_{acc}, and $I\,(t_{cal})$ is the signal obtained from a given calibration dose for a certain time t_{cal}. The fading correction factor and its relative error (see Appendix B) calculated specifically for the RTL signal, are taken into account in the dose recovery tests performed after irradiation on intact phones described in the following section.

4.2.5 Whole phone irradiations

The RTL measurement protocol on a single resistor described in the previous sections, was applied for recovering doses in trial irradiations of intact mobile phones. Different phone models were irradiated at the radiation facility of the Helmholtz Zentrum München with a ^{137}Cs gamma source with doses from 20 mGy up to 5 Gy (air kerma values). As in Fig. 3.10, phones were fixed with adhesive tape to plastic strings of a metal frame, with the frame not being in the radiation field. A 2 mm thick Perspex plate was used for build-up and the front side of the display glass faced the source. The circuit board of the mobile phones were located at one meter distance with respect to the source. After irradiations, the phones were disassembled in the laboratory (under dark room conditions), and resistors were extracted, cleaned, dried and measured at different times after the exposures, from a few hours to almost one month later.

The RTL measurements were performed with a preheat at 120°C for 10 s, and a TL readout up to 350°C using a heating rate of 2 °C/s. Then a background correction was applied, and an apparent unknown dose D_{TL} was first measured with several dose calibration points. The corrected dose was then calculated via:

$$D_{TL,C} = \frac{D_{TL}}{F} + D_{offset} \tag{4.5}$$

Where F is the fading correction factor and D_{offset} is the dose due to the offset time of the beta source assessed in section 4.2.1. The error in $D_{TL,C}$ was derived from the errors of D_{TL}, and the standard deviations of D_{offset} and F. Results are shown in Fig. 4.24.

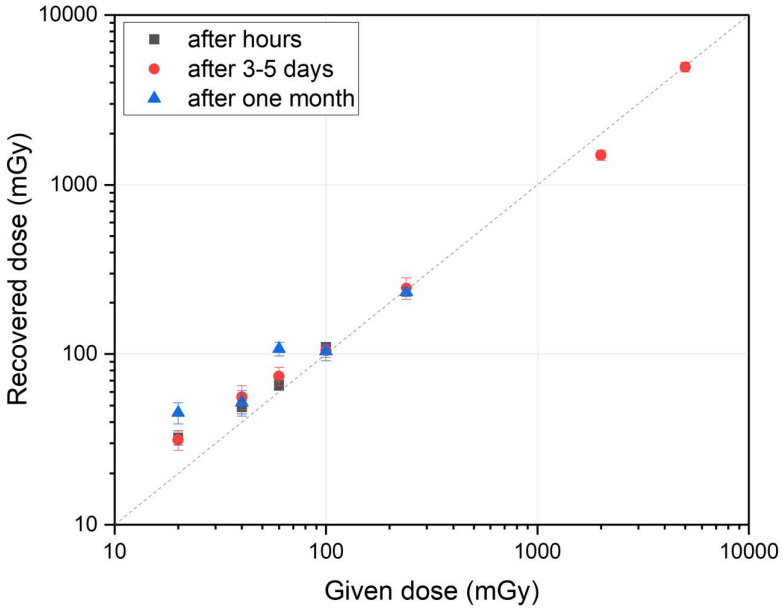

Figure 4.24: Results of trial irradiations on intact phones. Given doses are recovered with the RTL measurement protocol after different storage times.

An overestimation between 10 - 40 mGy is observed for given doses below 100 mGy, with the largest discrepancies occurring for doses recovered after one month of storage. Further investigations to address such overestimation of low doses were performed, and are described in the following subsection.

4.2.6 Background assessment

The intensity of a TL signal measured from resistors is composed of dark current, the dosimetric signal and thermal radiation.

The regions where one of the three dominates are:

- T < 100°C: dark current of the Photomultiplier Tube
- 125°C< T< 180°C: dosimetric signal
- T > 250°C: thermal radiation

After every TL measurement, a second one was performed on the same sample. The second signal read out is typically composed only of the dark current and the thermal radiation, since the traps related to the dosimetric signal had already been emptied by the first measurement.

The background correction of a TL measurement is then realized by simply subtracting the second TL signal from the first one. In Fig. 4.25, an example of a glow curve after background correction is illustrated.

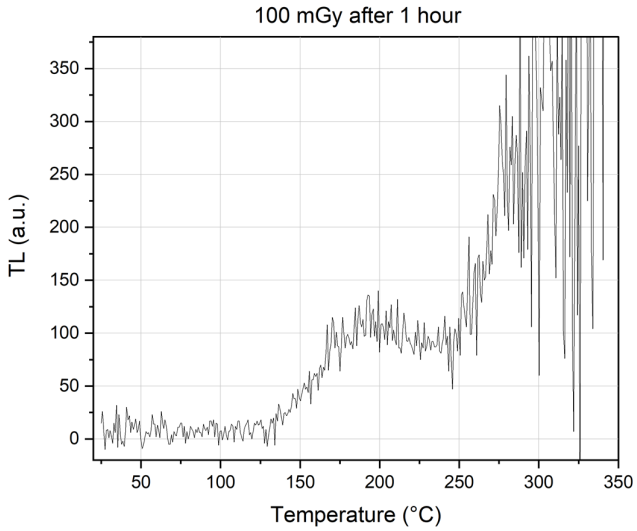

Figure 4.25: RTL glow curve of a resistor measured one hour after irradiation of an intact phone with 100 mGy. Negative counts are due to the process of background correction described above.

By analyzing the initial dark current counts of the PM tube of the reader from several RTL glow curves, a non-constant signal baseline was noticed. As depicted in Fig. 4.26, counts showed to be higher than zero at the beginning of the first signal read-out, in a real case corresponding to an accident dose, and stabilized only from 100°C on. This implies that the background could not be fully removed by subtracting the second measurement from the first one, thus leading to a positive bias likely relevant for low doses reconstruction.

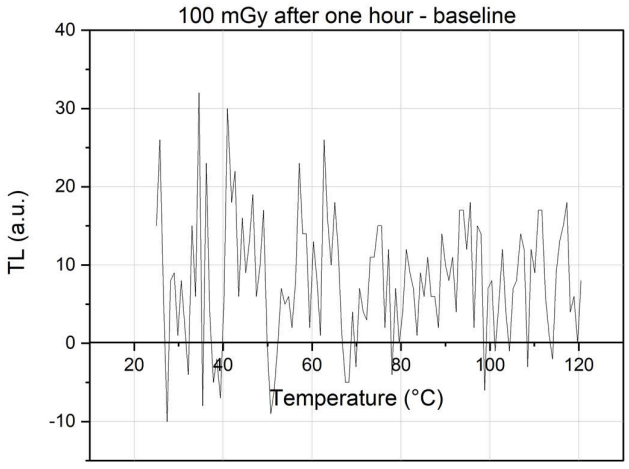

Figure 4.26: Detail of the fluctuating baseline of the same TL signal of Fig. 4.25.

The observed deviations might be attributed to the fixed operational mode of the Photo-multiplier Tube of the luminescent reader, which cools down to -20°C before and warms up to room temperature after every measurement. Such an instrumentation-specific aspect might have a stronger effect, as compared to higher doses, when recovering low dose signals especially later in time (~ one month later). As in the case of the 40 mGy dose reconstruction after one month from the intact phone irradiation, the dark current counts of the first measurement are in the order of the hundreds. The background correction is not sufficient to remove the positive bias observed in initial part of the glow curve, as illustrated in Fig. 4.27.

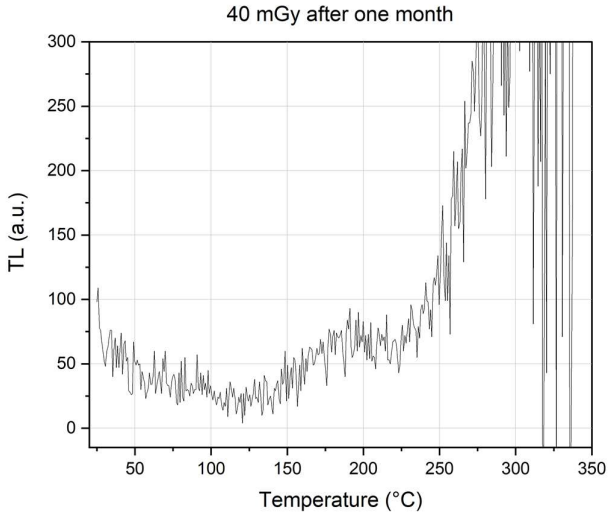

Figure 4.27: RTL glow curve of a resistor measured after one month from intact phone trial irradiation at 40 mGy. Initial dark current counts of the photo multiplier tube (PMT) are as high as 109 (at about 40°C).

In the light of these considerations, data analysis for the lowest measured doses (20-60 mGy) was revised introducing a modified background correction. In addition to the initial procedure of subtracting from the first TL signal a second one performed on the same sample, at the first readout the average of the counts recorded in the first 95 channels (from 25°C to 100°C) is further subtracted (see Fig.28).

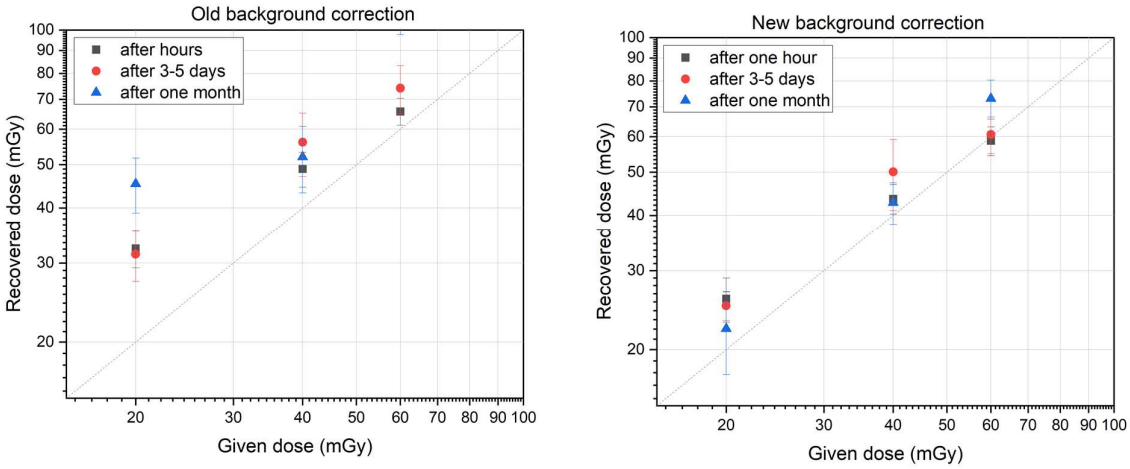

Figure 4.28: Comparison of the results of trial irradiations on intact phones after different storage times: on the left panel data are referred to the previous background correction (same as in Fig.4.26), whereas data on the right panel are assessed with the new background correction. For details see text.

This approach lead to the results reported in Table 4.5:

After 3-5 hours				
Given dose [mGy]	**Old BG correction Recovered dose [mGy]**	**Err [mGy]**	**New BG correction Recovered dose [mGy]**	**Err [mGy]**
20	31.78	±3.51	25.70	±3.42
40	49.18	±3.23	41.90	±3.72
60	66.38	±4.37	60.98	±4.54
After 3-5 days				
Given dose [mGy]	**Old BG correction Recovered dose [mGy]**	**Err [mGy]**	**New BG correction Recovered dose [mGy]**	**Err [mGy]**
20	31.37	±4.13	24.20	±3.86
40	58.64	±6.64	50.81	±5.76
60	68.44	±10.22	58.03	±9.56

After one month				
Given dose [mGy]	Old BG correction Recovered dose [mGy]	Err [mGy]	New BG correction Recovered dose [mGy]	Err [mGy]
20	45.32	±21.81	21.40	±19.20
40	49.70	±10.65	40.56	±8.72
60	107.48	±17.97	75.33	±12.50

Table 4.5: Results of dose recovery test performed with RTL on single resistors extracted from intact phones frontally irradiated with a ^{137}Cs source. Doses were recovered after different storage times, and data were processed with the two approaches of background (BG) corrections.

The errors attributed to the final recovered doses were assessed by choosing the uncertainties from either the weighted or unweighted linear fit, depending on which approach provided the larger uncertainty value (see Appendix B), in order to provide a conservative estimate. Overall, the data analysis employing the new background correction improved the results of the recovered doses. Limitations of the method arose when recovering the lowest dose of 20 mGy after the longest period of time of one month. In this case, the recovered dose was not statistically different from the detection limit (~ 10 mGy).

4.2.7 Energy dependence of resistors

In order to assess the usability of a material as dosimeter, it is important to investigate its response with respect to different radiation energies. The detected TL output, for a fixed dose, depends on the energy dependence of the material's radiation absorption coefficient. For irradiations with photons this is defined in terms of the mass energy absorption coefficient of a specific material, namely μ_{en}/ρ.

The photon energy response is defined as:

$$S_E(E) = \frac{\left(\mu_{en}/\rho\right)_m}{\left(\mu_{en}/\rho\right)_{ref}} \tag{4.6}$$

Where the subscripts refer to the material of the dosimeter ("m") and to a reference material (usually air) ("ref"). Energy loss of photons can be due to pair production, Compton scattering or the photoelectric effect.

Which process dominates depends not just upon the energy of the incident photon but also upon another parameter material-dependent, such as the effective atomic number Z_{eff}. The photoelectric component of the mass absorption coefficient varies approximately as Z_{eff}^3; the Compton component is proportional to Z_{eff}/M where M is the molar mass of the dosimeter material; the pair production component varies as Z_{eff}^2 (McKeever et al., 1995). Photoelectric effect dominate at low photon energies, whereas the Compton effect becomes the main type of interaction at higher photon energies. At last, pair production becomes relevant for energies above several MeV. The exact energy ranges for which all the above mentioned effects predominate are determined by Z_{eff}. The photon energy response is often defined with respect to the response from a given energy (e.g. ^{137}Cs and ^{60}Co). In this work, the red Thermoluminescence energy response of resistors was tested respect to photons with different mean energies from 25 keV to 250 keV from X-ray sources described in chapter 3, and compared that after irradiation using a ^{137}Cs source. A previous study conducted on OSL signals from 19 resistors extracted from different positions of a NOKIA 6300 circuit board, showed an over response up to a factor of 5 when samples were irradiated with photons of low energies (below 65 keV) (Dürr, 2011). For the investigations carried out within this work, ten resistors from a commercially available sample kit were placed in a Polymethylmethacrylat (PMMA) holder depicted in Fig. 4.29:

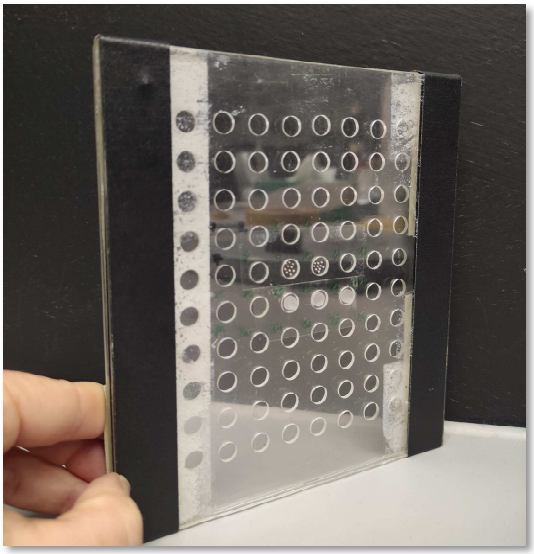

Figure 4.29: PMMA holder.

Results of the RTL measurements, and from past OSL measurements (Dürr, 2011), are shown in Fig. 4.30:

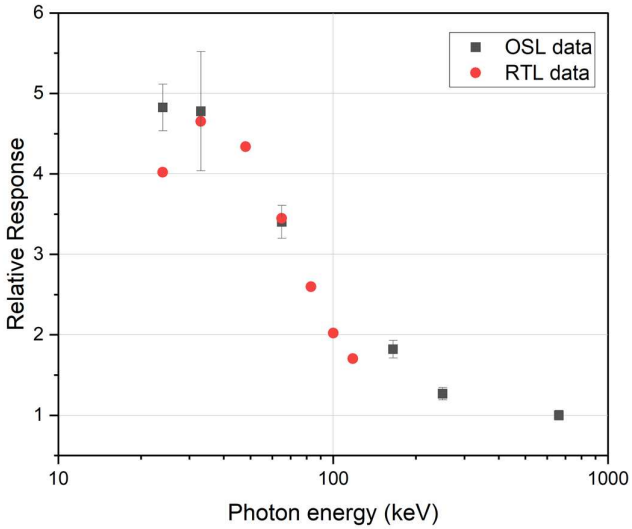

Figure 4.30: Photon energy response of RTL signals from extracted resistors (red dots) compared to that from a previous study on OSL (black dots). Data are normalized with respect to irradiations with same air kerma value using a ^{137}Cs source. Uncertainties of the RTL data were smaller than the red symbols.

The photon energy response, measured by the RTL signals, resulted to be in line with that described by the previous OSL data, down to an energy of 33 keV. The origin of the discrepancy of the two datasets at a photon energy of 24 keV is still unclear. To estimate the homogeneity of dose deposition for different radiation qualities and to have a full understanding of the energy dependence of resistors, not only in the extracted state but also when they are mounted inside of actual phones, MCNP simulations were performed as described in the following chapter.

5. Radiation transport simulations with MCNP

This chapter reports on the MCNP simulations carried out in support of the experimental work on the RTL retrospective dosimetry method developed in this thesis. After validating the MCNP environment as described in section 5.1, section 5.2 illustrates the results of the simulations of the energy dependence of an extracted resistor. The aim of such modelling work was to better understand the experimental results reported in subsection 4.2.7. Section 5.3 deals with simulations of a more realistic case, where resistors are placed on the circuit board of a phone, as this was the case in the experiments of frontal irradiations of an intact phone (Dürr, 2011). Therefore, a real-sized phone geometry was built up in MCNP in order to evaluate any possible shielding effect due to the layers of different materials in the phone surrounding the fortuitous dosimeter. The study of the energy dependence of the resistors, either simulated free in air or placed inside a phone, was indispensable to provide a preliminary background knowledge for the subsequent conversion factors calculations. As already stated in chapter 2, such coefficients correlate the dose to the material (the resistors) with the organ absorbed dose and are important for providing a more reliable dosimetry of radiation risk for individuals, when using a phone as a fortuitous dosimeter. As an application of the methodology, the MCNP code was employed to simulate a test exposure scenario described in section 5.4, where an individual is standing on a soil contaminated by a radionuclide (scenario which might be realistic for example after a Nuclear Power Plant (NPP) accident). For this specific case, the differences in sizes between the source (e.g. the contaminated ground ~ m^2), and the electronic component (~ mm^2) which is used as dosimeter, has an impact on the efficiency of the simulation and on the precision of the conversion factors obtained. Hence, for comparison, simulations were also performed with an anthropomorphic voxel phantom equipped with a complex geometry of resistors inside a phone as well as with a simplified dosimeter geometry (thin cylinders of pure aluminum oxide). The two configurations were tested for two of the most relevant radionuclides that might be released in a nuclear emergency with photon emissions in the high- to medium- energy range (^{137}Cs at 662 keV and ^{131}I at 364 keV, respectively) and for a radionuclide with photon emissions in the low energy range (^{147}Nd at 91 keV).

5.1 Validation of the simulations

A simulation model is valid only if it is an accurate representation of an actual system, and in order to verify that, a validation process is required. In this work, the environment of the radiation transport code MCNP6.2 was validated by reproducing the simulations reported in Discher et al. (2015). In the latter, the energy dependence of a glass display of a mobile phone (NOKIA 5250) was simulated using the radiation transport code MCNP5, and the results were compared to the previous experimental data (Discher et al.2014). The same geometry of the mobile phone reported in the above mentioned paper, was built here as a set of rectangular layers of different materials, and a squared piece of glass from the display with sizes 0.5 x 0.5 x 0.05 cm^3 served as detector.

The source was modelled as a disc of radius 10 cm emitting monoenergetic photons at different energies (662 keV for ^{137}Cs and mean energies corresponding to the N30 to N300 X-ray narrow beam series). The energy deposition in the volume associated to the glass detector was scored with an energy deposition F6 tally. The simulated over response up to a factor of 4.76 for photon energy of 48 keV obtained in the present thesis resulted in line with the values simulated by Discher et al. (2015) and the validation was considered successful (Fig.5.1).

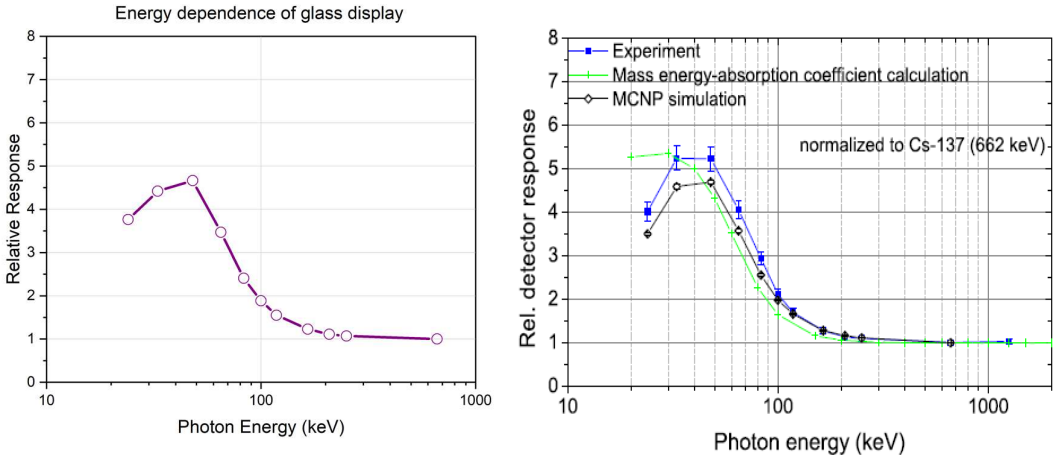

Figure 5.1: Results of the validation process on the left, and the published data (Discher et al.,2015) on the right. Responses are normalized to ^{137}Cs.

5.2 Simulations of the energy dependence of extracted resistors

The experimental study carried out on extracted resistors irradiated at different photon energies (see subsection 4.2.7) highlighted an over response up to a factor of 4.7 when measuring with the RTL technique. The MCNP radiation transport code version 6.2 was used to reproduce the same experimental conditions, with a real-sized and detailed model of a SMR from Bourns (model CRT0402) (Fig. 5.2). The code was based on photon cross-section libraries MCPLIB04 (Colin J.L., 2017) and it was run on a PC mounting an Intel(R) Core(TM) i7-8700K processor with six cores up to 3.7 GHz.

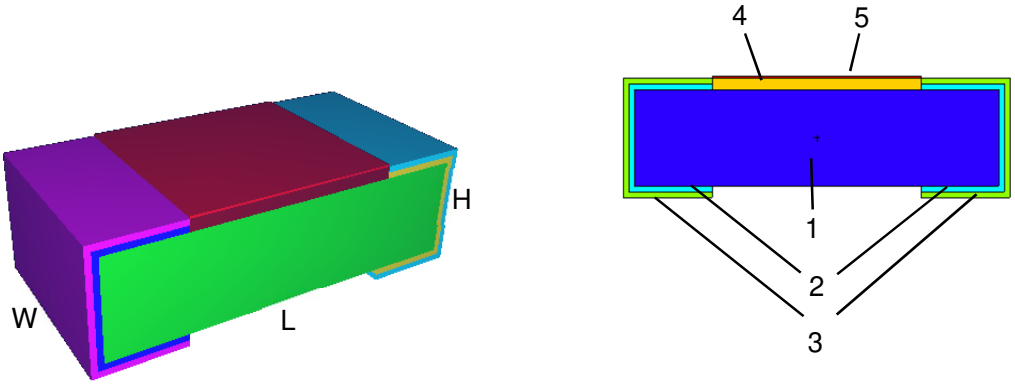

Figure 5.2: 3D view (left) and sectioned side view (right) of resistor modelled in MCNP. W: width; L: length; H: height (see Table 5.1 for dimensions). 1: ceramic core; 2 and 3: metal contacts made of tin and nickel respectively; 4: resistive layer; 5: thin layer of resin.

The elemental composition of the resistor is reported in Appendix A, while its dimensions are listed in Table 5.1.

	Dimensions (cm)		
Part	**L**	**W**	**H**
Al_2O_3	0.094	0.05	0.024
Resistive layer	0.054	0.05	0.003
Resin	0.054	0.05	0.0005
Nickel	0.0215	0.05	0.0015
Tin	0.023	0.05	0.0015

Table 5.1: Components and dimensions of the resistor modelled in MCNP.

For the model, the resistor was placed inside a PMMA cylindrical holder of radius 0.5 cm and thickness 0.1 cm, as was the case for the measurements (see Fig.4.30). The X-Ray source was simulated as a disc of 1 cm radius frontally located at 0.07 cm distance from the edge of the PMMA to enhance the efficiency of the simulation. The photon spectra of the N-series narrow beam filters, from N30 (24 keV) up to N300 (250 keV) were approximated by a histogram with a resolution in energy of 0.5 keV. The latter was directly implemented in the section of the code including the characteristics of the source. The corresponding central-axis spectra for each filter specification according to ISO 1996 (4037-1, 1996), were calculated with the software SpekCalc V1.1 (Poludniowski, 2009). Results were normalized to ^{137}Cs, modelled as monoenergetic source with a photon energy of 0.662 MeV. The radiation transport mode selected was the mode (p e), thus the energy deposition in the cell describing the ceramic core of the resistor was scored with the *F8 tally. The latter, divided by the cell mass, represents the absorbed dose from photons and electrons, as stated in chapter 2. As from theory tally *F8 should match with tally F6, representing dose deposition into a target volume in kerma approximation conditions. A systematic comparison between the two tallies showed that the equilibrium was not fully met, thus F6 results were less precise than *F8 up to a maximum deviation of 20%. This discrepancy among the two quantities was partially ascribed to the thin detector sizes with respect to the secondary electron ranges, as well as to the neighboring volumes of the ceramic core characterized by a different atomic number Z.

The *F8 tally was finally considered more accurate and chosen for both the geometry described here (extracted resistor) and for the ones of the following sections (resistor inside the phone). In a first step, simulations were run with the ceramic core of the detector purely composed of Al_2O_3. Such configuration lead to a considerable discrepancy between simulated results and measured data. To reduce such discrepancy and thus to better match modelled and experimental data, an alternative approach was considered.

In particular, as a kind of sensitivity analysis, the elemental composition of the resistor ceramic was modified by adding various concentrations of chromium (3-4-5-6-10%) not explicitly reported by the manufacturer datasheet but supported by the red luminescent emission. A second option was to add Calcium, since its presence in the alumina matrix was confirmed by a SEM EDX analysis reported in the literature by (Koroukla, 2015).

The best agreement between simulated and experimental data was found when the elemental composition of the targeted ceramic core was modified with either 4% of Chromium or 6% Calcium (see Fig.5.3).

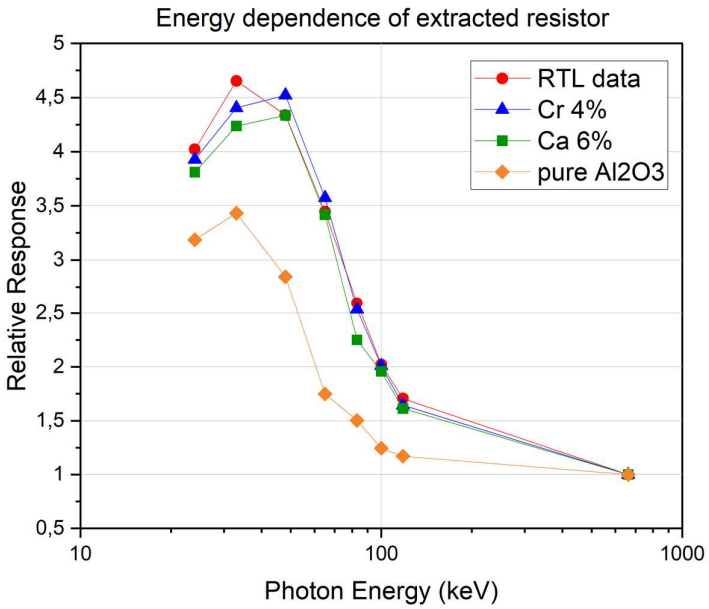

Figure 5.3: Energy dependence study on extracted resistor configuration: comparison between experimental (red data points) and simulated data (blue, green and yellow datasets). Statistical uncertainties on the simulated data are in the order of 3% and therefore smaller than the symbol size. Also uncertainties of the experimental data are smaller than the symbols. Responses are normalized to ^{137}Cs.

To investigate whether the assumed concentrations were realistic, in collaboration with the Department of Earth and Environmental Sciences at the Ludwig-Maximilians-Universität München (LMU), a trace element analysis with a Cameca SX-100 Electron Probe Microanalyter (EPMA) was performed on 20 resistors from commercially available kits (details in Appendix B). Next to the main presence of Aluminum (51.19±0.19)wt% and Oxygen (47.13±0.06)wt%, the measurements showed on average: (18.55±1.19) ppm of Ca, (18.15±0.99) ppm of Mg, (21.70±1.34) ppm of Si and (26.88±1.32) ppm of Cr. Therefore, presence of Chromium and Calcium in the order of wt% used in the simulations described above were not supported by the EPMA measurements. The observed mismatching between the RTL experimental data and the simulated ones in the energy dependence study might be due to the fact, as highlighted in the study

of Gasparian et al. (2012) on Al_2O_3:C single crystals detectors (TLD-500), that their energy response was not only determined by the energy of the photons absorbed in the detector, but also by how the ionization density affected the concentrations of defects.
In particular, an increase in ionization density caused by photon fields below 48 keV, resulted in an increase of F-center concentrations in the material and, consequently, lead to different TL and OSL properties with higher relative response to ^{60}Co. This finding is also in agreement with a previous experimental study by Jain et al. (2007), who reported that the Al_2O_3:C higher relative response to ^{60}Co gamma irradiations depended not only on the material that constitutes the detector, but also on the defects involved in the luminescent processes. Since the bulk cores of electronic components are composed mainly of alumina, the proposed mechanism to explain the TLD data might be applicable. Then it would be reasonable to attribute their properties also to micro-dosimetric effects, which could explain the enhanced efficiency when converting the absorbed dose into a luminescent signal that is not reproducible in the MCNP code environment.

5.3 Simulations of the energy dependence of resistors in phones

Concerning the understanding of the process of dose deposition in the resistors for different radiation qualities, a step forward was made by considering the more realistic case in which the fortuitous dosimeter is located inside an actual phone. In this respect, results of the simulations were compared with experimental result from an earlier study by Dürr (2011). Even though the latter included OSL measurements on an out-of-date phone mode, it was used for comparison because, due to time constraints, it was not possible to perform measurements with RTL method developed within this work. The geometry of the phone model NOKIA 6300 used in the experiment of Dürr (2011), was reconstructed here in MCNP as a set of rectangular volumes of different materials and dimensions (specifications listed in Table C.2 of Appendix A) stacked on top of each other (see Fig. 5.4). Starting from the front side of the phone model, the elements (with the approximated thickness in brackets) were: a glass display module (2.2 mm), an aluminum layer (0.15 mm), a printed circuit board (1.12 mm), three resistors (0.35 mm), another aluminum layer (0.15 mm) and the battery (4.5 mm).

The stacked components in the front were surrounded by a plastic cover of 1 mm, whereas on the backside of the phone the case was partially metallic (0.5 mm). The three resistors, serving as detectors, were simulated with the realistic thickness and structure described in section 5.2, but with the ceramic core with a fictitious enrichment of 4% Chromium (see Fig.5.3) and enlarged in length and height (1 cm x 0.5 cm).

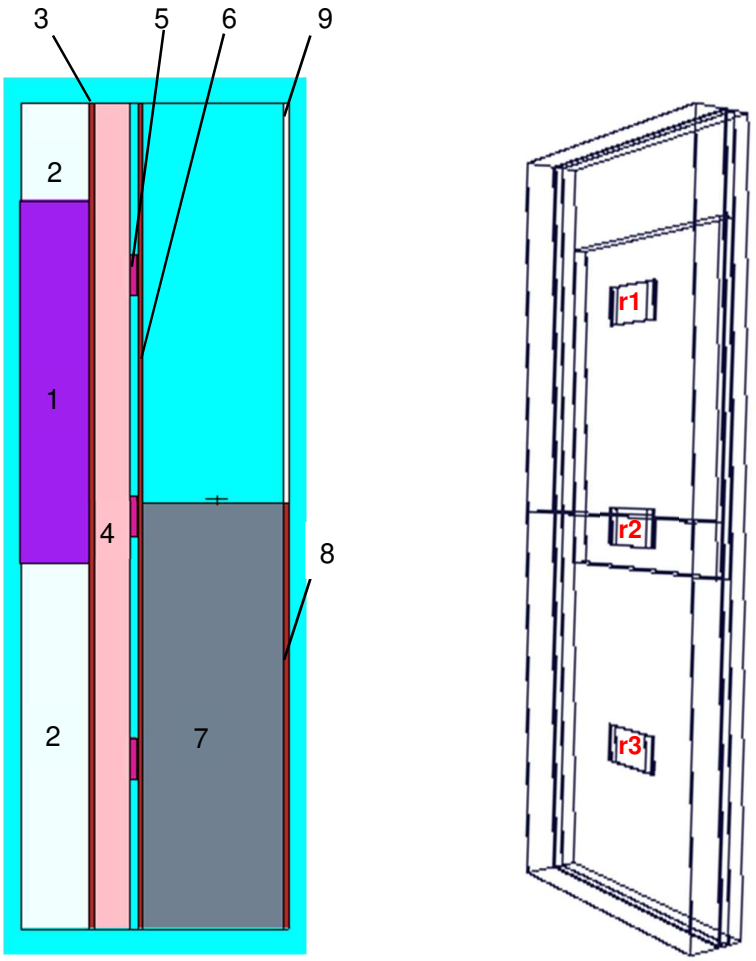

Figure 5.4: Sectioned side view (left) and wireframe view (right) of the simulated NOKIA6300 used by Dürr (2011). The sectioned view shows the elements of the phone: 1: display glass; 2: polyamide plastic frontal cover; 3 and 6: aluminum layer; 4: circuit board; 5: resistors; 7: battery; 8: aluminum back cover; 9: polyamide plastic back cover. The wireframe representation shows the exact locations of the three detectors (resistors r1, r2 and r3) on the circuit board.

The three different locations of the resistors on the circuit board allowed to explore any difference in dose deposition arising from the shielding due to the display glass (resistor 1), to the plastic cover (resistor 3), and to the combination of the two (resistor 2).

Moreover, the increased target volumes of the resistors helped to reduce the computation time and to improve the efficiency of the simulation. In this respect, another configuration was also tested. The three resistors were replaced by a rectangular target volume of the same thickness but with length and height of the printed circuit board (4.05 cm x 10.25 cm). Also in this case, the elemental composition was maintained of alumina enriched with 4% Chromium, and the resistive and epoxy layers were enlarged accordingly. The side terminations were excluded, because enlarging them proportionally would have implied a false representation of where the part of ceramic covered by the metal contacts was located inside the phone. The source was modelled as a disc of radius 6 cm placed in front of the phone at a distance of 1 cm, emitting monoenergetic photons at different energies: from 24 keV of the N-30 X-ray filter up to 0.662 MeV of ^{137}Cs.

Energy deposition was scored with the tally *F8. Results normalized to Cesium are showed in Fig. 5.5.

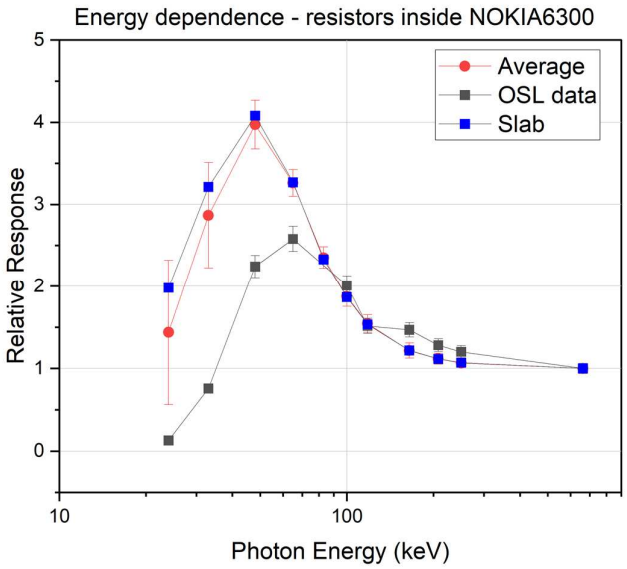

Figure 5.5: Energy dependence study on resistors inside phone NOKIA6300 (as Fig. 5.4). Dataset in red represents the results averaged among the simulated three resistors; black dataset is from Dürr (2011); blue dataset represents simulations with one big slab of Al_2O_3 with 4%Cr as the same size of the phone (for details see text). Responses are normalized to ^{137}Cs.

Figure 5.5 demonstrates that the simulated data are 16% higher than the experimental ones for energies in the range 250 keV<E<165 keV. The discrepancy becomes more pronounced at energies below 65 keV, where the simulated data are more than 60% higher than the corresponding experimental data. With regard to the three-resistors configuration, the dose deposited in r3 shows a difference of up to 15% as compared to the dose deposited in r1, which is fully shielded by the display glass. Such difference becomes more than 60% for the two energies of 33 keV (N-40) and 24 keV (N-30), where the 2.2 mm of glass strongly attenuates the dose deposition in r1: this is translated in higher standard deviations represented in Fig. 5.5. Results for r3 are more in line with those of r2 (2-6%), for which the partial shielding by the plastic case mitigates the pronounced shielding of the glass. The simplified slab geometry provided results consistent with those obtained for the three-detector configuration (see Fig.5.5) and allowed to reduce the computational time from the order of hours down to the order of minutes for the same simulated number of particles. However, the discrepancy with experimental data is still present. A possible explanation for the difference between experimental and simulated results could be an incorrect simulation of the physical and chemical properties of both the circuit board and the display glass. Thus, different elemental compositions found in the literature for glass (Bassinet C. , et al., 2014) as well as for the printed circuit board (Holgersson et al.,2017; Yamane et al.,2011) seemed possible and were explored. In addition, the density of the circuit board, previously set at a value of 1.8 g/cm^3 (see Appendix A) as supported by literature, was modified with values ranging from 3 g/cm^3 up to a hypothetical value of 5 g/cm^3. The former was rounded based on a value of 3.23 g/cm^3 assessed by measuring the dimensions and mass of the NOKIA 6300 after removing all the surface-mount electronic components.

Fig. 5.6 reports the results of the two most representative cases.

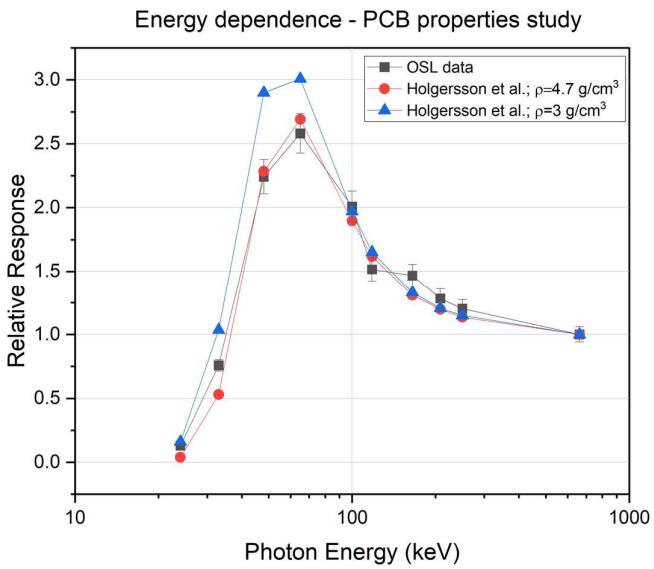

Figure 5.6: Energy dependence study on resistors inside a NOKIA6300: shielding effect due to circuit boards with same elemental composition as mentioned in Holgersson et al.,2017 and two different densities. OSL data reported in black are from Dürr (2011). Uncertainties of the simulated data are smaller than the symbol size. Responses are normalized to ^{137}Cs.

The best agreement with the experimental data was found for a circuit board composed by the elements reported in Holgersson et al. (2017) and with a hypothetical density of 4.7 g/cm^3. It becomes evident that, when a whole phone structure is simulated, not only the resistor elemental composition but also other unknown parameters might affect the results. To have more updated insights into the shielding effects of more modern phone models (NOKIA 6300 was released on the market as early as in 2006), an energy dependence study was also performed using a NOKIA 1 (2018). Time constraints limited the possibility to repeat the entire study with red TL on resistors. Instead, as an alternative, TLD-500 Al_2O_3:C single crystals were used as detectors. In fact, TLDs are characterized by high sensitivity and stable signals, properties that allow carrying out measurements in a shorter time. The decision to pursue this approach was supported also by the evidence that, for NOKIA 6300, data acquired with TLDs were in agreement (within 10%) with the OSL data from resistors. Three TLDs (TLD1, TLD2 and TLD3) were placed inside the old phone model (NOKIA6300) and few frontal irradiations with an X-ray source narrow beam filter N40 (33 keV), N80 (65 keV) and with ^{137}Cs were repeated. The results were compared to those reported by Dürr (2011).

Results are presented in Fig. 5.7 as the ratio between the luminescent signals detected inside the phone to the signals obtained outside.

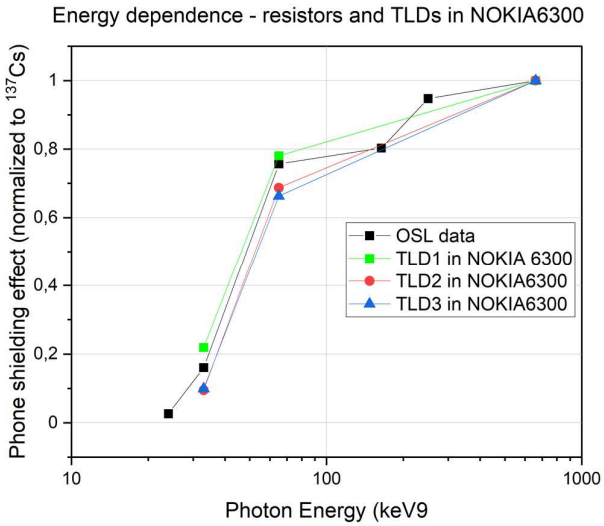

Figure 5.7: NOKIA6300 shielding effects assessed with resistors (OSL data by Dürr (2011) in black) and the three TLDs (TLD1, TLD2 and TLD3). Uncertainties are smaller than the symbol sizes.

The same three TLD-500 were used to quantify the shielding effects of the NOKIA 1, where they were located on the circuit board as shown in Fig. 5.8:

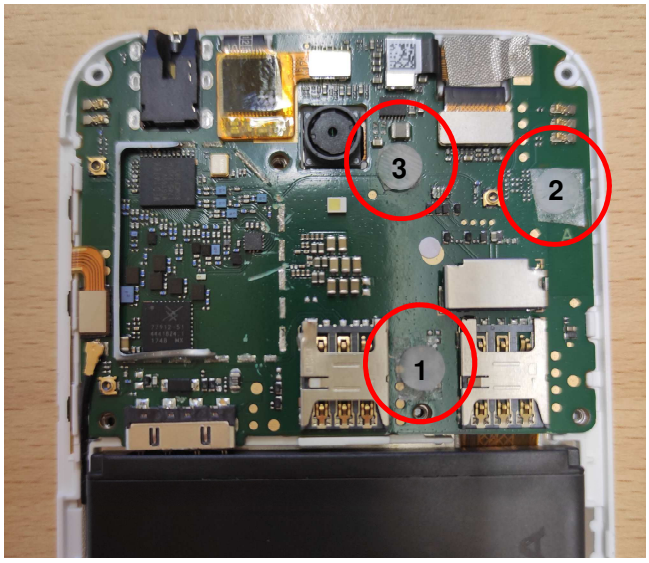

Figure 5.8: TLD-500 attached at three different locations on the printed circuit board of NOKIA1 mobile phone.

The NOKIA 1 geometry was built in MCNP as for the previous NOKIA 6300 model, as a set of rectangular shapes of different volumes depicted in Fig. 5.9:

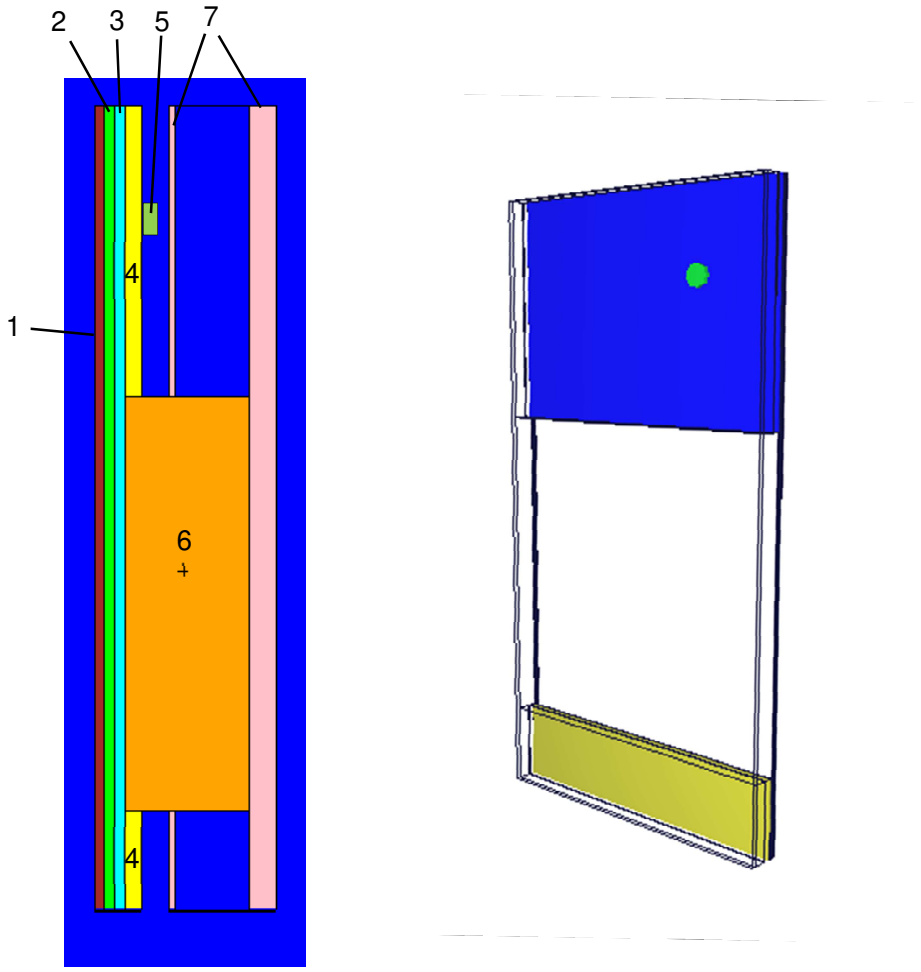

Figure 5.9: Sectioned side view (right) and wireframe view (left) of the simulated NOKIA1. The sectioned view shows the elements of the phone: 1: outer display glass; 2: touch-screen module; 3: inner display glass; 4: circuit board; 5: TLD-500 detector; 6: battery; 7: plastic inside layer and outside cover. In the wireframe representation is showed the exact location of the detector on the circuit board, chosen as an "average" position of the experimental three ones.

Starting from the front side of the phone model, the elements are: a display module composed of two identical glass plates (front and back side glass, 0.7 mm) with a touch-screen module with a 100 nm ITO (indium tin oxide) layer in between them, the printed circuit board (0.63 mm) surrounding the battery (4.6 mm) and covered by a thin layer of plastic (2.3 mm).

The backside of the phone is covered by a plastic case of 1 mm thickness. Materials characteristics are listed in table A.3 in Appendix A. The detectors were modelled as a single cylinder of pure Al_2O_3, 5 mm in diameter and 0.9 mm thick, located on the upper part of the circuit board in an equal distance to the actual three TLDs (TLD1, TLD2, and TLD3). Experimental results and simulated data are presented in Fig. 5.10:

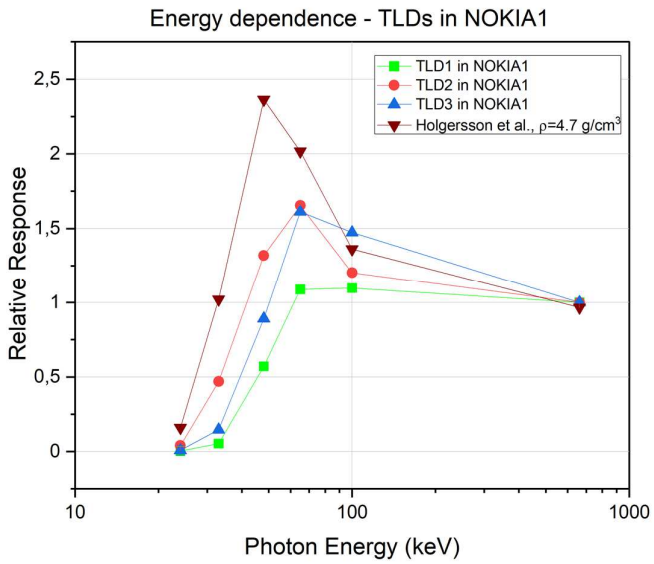

Figure 5.10: Energy dependence study carried out with three TLD-500 placed inside a NOKIA1 phone. Simulated dataset is represented in dark red. Uncertainties are smaller than the symbol sizes. Responses are normalized to ^{137}Cs.

The parameters of the simulated circuit board were based on the experience with the previous NOKIA6300 simulations that showed the best agreement with the data when using the elemental composition from Holgersson (2017) with a density of 4.7 g/cm^3. However, in this case, simulated data for energies below 100 keV showed a consistent discrepancy with respect to the measurements performed with the TLDs. Again, obviously, the phone model built in the MCNP code includes unknown parameters related to physical and chemical properties that do not allow to accurately reproduce the measurements.

On the other hand, the measurements carried out with the TLDs allowed to assess the differences between the shielding effects of the two phones. Fig. 5.11 shows the results of the ratio between doses detected inside the two phones and the doses outside, for the same selected energies:

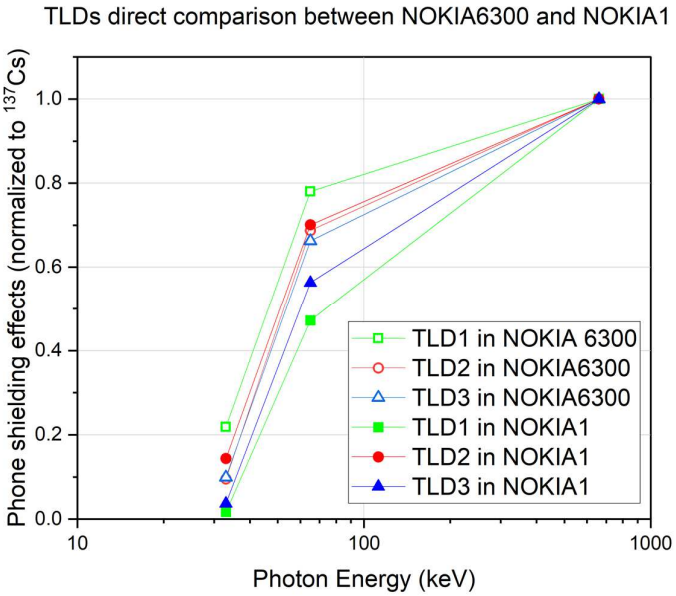

Figure 5.11: Comparison between the results of the energy dependence of TLDs placed inside the old NOKIA6300 (open symbols) and the newer NOKIA1 (full symbols). Uncertainties are smaller than the symbol sizes.

Two out of the three detectors placed in the newer phone model (NOKIA1) demonstrated a more pronounced shielding effect compared to when they were placed in the old one (i.e., TLD1 and TLD3 in Fig. 5.11). Such a discrepancy is due to the characteristic structure of the modern phones, for which the glass display covers the whole front side.
In addition, the different phone structure might also have an impact on back irradiations, since the circuit board of most of the new phones surrounds the battery compartment. Therefore, the fortuitous dosimeter would not be accidentally shielded by the battery, as for previous models. To study the energy dependence also for back irradiations of the phones will require further investigations.

5.4 Voxel Phantom simulations: nuclear emergency scenario

The radiation transport code MCNP was used to derive sets of appropriate conversion factors between physical doses and the concurrent biological doses to individuals. The overall approach, was, as stated in the CONFIDENCE Deliverabile 9.10:"to build a model of a realistic exposure scenario of relevance to accident dosimetry, and position an anthropomorphic phantom within that environment" (Mafodda et al.,2019b).

A scheme representing the geometry is shown in Fig. 5.12:

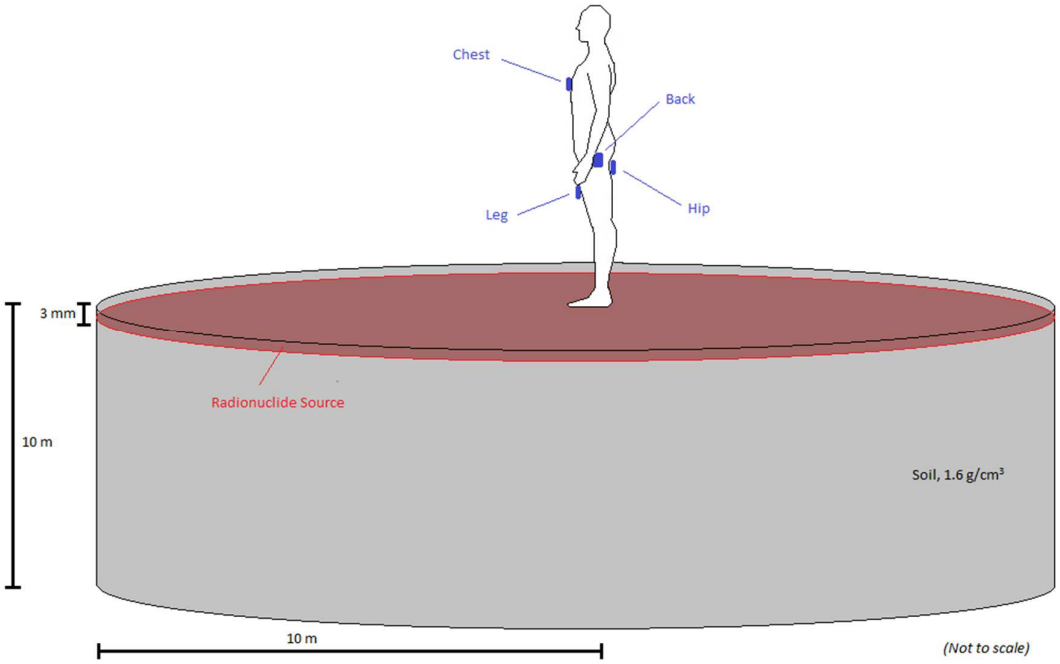

Figure 5.12: Scheme of simulated exposure scenario (not to scale) (CONFIDENCE Deliverable 9.10, Mafodda et al.,2019b)

The soil was assumed to have a density of 1.6 g/cm^3 and a chemical composition as defined in Table 5.2 (Eckerman, 1993). It was modelled as a homogenous cylinder of radius and depth of ten meters each.

Element	H	C	O	Al	Si	K	Ca	Fe
Mass fraction	0.021	0.016	0.577	0.050	0.271	0.013	0.041	0.011

Table 5.2: Composition of soil used in the modelling (Eckerman, 1993). Table reported in CONFIDENCE Deliverable 9.10, Mafodda et al., 2019.

In order to calculate the doses to the individual, the ICRP Reference Male voxel phantom (ICRP, 2008) was placed at the center of the modelled cylindrical geometry (Figure 5.12). As a reasonable approximation, such a wide cylindrical geometry from the point of view of an individual standing on top of the rotational axis, can be considered "infinitely deep" in terms of photon backscatter. Although wider cylinders could potentially lead to incrementally larger doses, the addition would approximately reduce with $E_1(\mu h/\cos\vartheta)$, where μ is the linear attenuation coefficient for photons in air, h the height of the dosimeter (phone), ϑ the angle under which the rim of the cylinder would be seen from the point of view of the dosimeter, and E_1 the exponential integral, leading to vanishingly smaller contributions. Moreover, because the conversion coefficients are calculated from ratios between doses, "missing" contributions are cancelled anyway.

To explore any difference in the dose received depending on the locations of the phone (Bossin, 2019; Discher et al.,2015; Eakins & Koroukla, 2015; Kim et al. 2019)
the phantom "wears" the dosimeters at four different points on his body. As reported in the CONFIDENCE Deliverable 9.10 (Mafodda et al.,2019b):"the four configurations cover the most likely places for mobile phones to be worn by the person when not in use:

1. "Chest", i.e. with the phone centered close to the location of the heart.
   This configuration is representative of a phone positioned in an inside jacket or breast pocket.
2. "Leg", i.e. with the phone centered just in front of the left thigh.
   This configuration is representative of a phone positioned in a trouser front pocket.
3. "Back", i.e. with the phone centered just behind the left buttock.
   This configuration is representative of a phone positioned in a trouser back pocket.
4. "Hip", i.e. with the phone centered close to the left hip.
   This configuration is representative of a phone positioned either in the outside pocket of a jacket, or held in the left hand, or inside a handbag or shoulder bag with its strap over the left arm".

From the same work :"only locations on the left side of the body were considered, since a left-right symmetry of the body may reasonably be assumed when subsequently applying the conversion coefficients".

In the model, the soil was assumed to be contaminated by the most relevant gamma sources for nuclear emergency scenarios (IAEA, 2017), ^{137}Cs and ^{131}I. While ^{137}Cs was assumed to emit monoenergetic photons at 662 keV, for ^{131}I an energy distribution with a main energy of ~360 keV was assumed (Radiological Safety Guidance, 2018). In addition, a case of ground contamination due to ^{147}Nd was explored, a radionuclide listed by the IAEA among the ones contributing to the external exposure in a NPP fallout.

^{147}Nd is characterized by a main emission of gamma photons at 91 keV, representing the best candidate to investigate the fortuitous dosimeter responses, and consequently the calculations of the conversion factors at a low energy. In the model, the radionuclide of interest was assumed to contaminate uniformly the soil until a depth of three millimiters (Petoussi-Henss et al., 2012) and the emission was assumed to be isotropic with both direct and backscattered components. In a first simplified approach, the retrospective dosimeters were modelled as thin cylinders of pure aluminum oxide with a density of 3.72 g/cm^3, a radius of 0.564 cm and a thickness of 0.05 cm. Although the thickness is comparable with the height of a typical resistor inside a mobile phone, the radius (effective area of ~1 cm^2) was arbitrarily chosen with the intention of reducing the computation time. As a comparison, simulations for the same set of radionuclides and configurations (“chest”, ”leg”, ”back” and “hip”) were repeated with a fully realistic model of a complete mobile phone geometry. In particular, the voxel phantom was equipped with the NOKIA1 model described in paragraph 5.3, with the resistor modelled as a rectangular layer of Al_2O_3 with a mass fraction of 4% of Chromium, covering the entire area of the PCB. Once again, the choice of enlarging the simulated target volumes allowed to improve the efficiency of the calculations thus reducing the required simulation time.

The Monte Carlo calculations were run assuming the kerma approximation conditions, thus considering the transport of only photons (mode p). As for the simulations described in section 5.2 and 5.3, the discrepancy observed between *F8 and F6 tallies motivated to choose the more accurate one (*F8). However, in order to enhance the efficiency of the calculations given the large spatial extent of the voxel geometry, the choice fell on the F6:p photon kerma tally.

Thus, the secondary charged particle equilibrium condition was assumed at all target points. The reason behind, is that the secondary electrons are expected to have maximum ranges included the dimensions of the geometry (ICRU, 1984). F6 was used to target doses to the aluminium oxide cylinders, the layer of interest within the phone, as well as to the organs within the body. As stated in the CONFIDENCE Deliverable 9.10: "for the dose to the red bone marrow (RBM), fluence tallies were used in conjunction with energy-dependent weighting factors that take into account the dose enhancement within the bone according to ICRP Publication 116. (ICRP, 2010)" (Mafodda et al., 2019b). Dose conversion factors $C_{P\to O}^{L}$, from phone ("P") to organ doses ("O"), were derived for each location L by the ratio:

$$C_{P\to O}^{L} = \frac{D_O}{D_P^L}$$

Where D_O represents the organ dose and D_P^L the absorbed doses to the dosimeter. In this way, the measured dose to a phone of which the location is taken as a variable in the MCNP input file, may be multiplied by the conversion factors to provide the concurrent doses to the organs of interest. Such conversion factors are dimensionless, since their formal unit would be calculated as the ratio (Gy/Gy).

Values of $C_{P\to O}^{L}$ are provided for ^{137}Cs, ^{131}I and ^{147}Nd, and for those organs that are critically important in radiation risk assessments following nuclear accident scenarios: RBM, colon, breast and thyroid. Tables 5.3, 5.4 and 5.5 summarize the results for the simplified target of cylinder of aluminium oxide. The uncertainties shown refer to one standard deviation, and are referred to statistical uncertainties from the Monte Carlo stochastic modelling process.

	Conversion Factor, $C_{P\to O}^{L}$ (Gy/Gy) for ^{137}Cs			
Location, L	*Colon*	*Thyroid*	*Breast*	*RBM*
Chest	0.99 (0.03)	0.84 (0.03)	1.03 (0.03)	0.90 (0.02)
Leg	0.74 (0.02)	0.63 (0.02)	0.77 (0.02)	0.68 (0.02)
Back	0.81 (0.02)	0.68 (0.02)	0.84 (0.02)	0.74 (0.02)
Hip	0.82 (0.02)	0.70 (0.02)	0.86 (0.03)	0.75 (0.02)

Table 5.3: Conversion factors, $C_{P\to O}^{L}$, for ^{137}Cs ground contamination for four organs: colon, thyroid, breast and RBM. Bracketed values denote one standard uncertainty. (CONFIDENCE Deliverable 9.10, Mafodda et al., 2019b).

Conversion Factor, $C_{P\to O}^{L}$ (Gy/Gy) for ^{131}I				
Location, L	*Colon*	*Thyroid*	*Breast*	*RBM*
Chest	0.93 (0.03)	0.78 (0.02)	0.98 (0.03)	0.84 (0.02)
Leg	0.71 (0.02)	0.60 (0.02)	0.75 (0.02)	0.64 (0.02)
Back	0.76 (0.02)	0.64 (0.02)	0.80 (0.02)	0.69 (0.02)
Hip	0.78 (0.02)	0.66 (0.02)	0.82 (0.02)	0.70 (0.02)

Table 5.4: Conversion factors, $C_{P\to O}^{L}$, for ^{131}I ground contamination for four organs: colon, thyroid, breast and RBM. Bracketed values denote one standard uncertainty (CONFIDENCE Deliverable 9.10, Mafodda et al., 2019b).

Conversion Factor, $C_{P\to O}^{L}$ (Gy/Gy) for ^{147}Nd				
Location, L	*Colon*	*Thyroid*	*Breast*	*RBM*
Chest	0.86 (0.03)	0.73 (0.02)	0.88 (0.03)	0.75 (0.02)
Leg	0.62 (0.02)	0.53 (0.01)	0.64 (0.02)	0.55 (0.02)
Back	0.70 (0.02)	0.60 (0.02)	0.72 (0.02)	0.62 (0.02)
Hip	0.69 (0.02)	0.58 (0.02)	0.71 (0.02)	0.60 (0.02)

Table 5.5: Conversion factors, $C_{P\to O}^{L}$, for ^{147}Nd ground contamination for four organs: colon, thyroid, breast and RBM. Bracketed values denote one standard uncertainty.

The trends observed from the above tables can be explained by the exposure conditions and the distributed positioning of the various dosimeters and organs around the geometry. For instance, within each table, it is possible to notice that conversion factors for the "chest" are closer to unity than conversion factors for other locations. In fact, the dosimeter in that position is slightly in closer proximity to the investigated organs within the body. On the contrary, the values of $C_{P\to O}^{L}$ tend to reduce with decreasing distance of the dosimeter to the ground, thus being increasingly close to the radionuclide source. In particular, the cylinders of Al_2O_3 located on the leg exhibit the largest relative dose, which leads to the smallest conversion factors. Moreover, all the conversion factors for ^{131}I and ^{147}Nd are lower than their counterparts for ^{137}Cs, because the mean energy of the photons emitted by the former radionuclides is significantly lower than that of the 662 keV photons of the latter. For both lower energetic radionuclides, a combination of two effects must be considered. First, the radiation field gets attenuated even before reaching the target organ.

Second, as from the energy dependence study on both extracted resistors (see Fig. 5.3) and resistors inside the phone (see Fig. 5.5), the dosimeter absorbs more than human tissues for energies below 660 keV. The statistical uncertainties given in tables 5.3, 5.4 and 5.5 are considered reasonably low for the purposes of the present work (< few %, at one standard deviation), but could be further improved (lowered) by running the simulations for longer periods of time (more than the ~ 12 hours used). In fact, Monte Carlo precision scales with the square-root of the computational time. The following tables 5.6, 5.7 and 5.8 summarize the $C_{P\to O}^{L}$ values for the same configurations but with the complete geometry of the phone and the resistor of the same size of the PCB as target volume.

	Conversion Factor, $C_{P\to O}^{L}$ (Gy/Gy) for ^{137}Cs			
Location, L	*Colon*	*Thyroid*	*Breast*	*RBM*
Chest	0.98 (0.02)	0.83 (0.03)	1.01 (0.03)	0.89 (0.02)
Leg	0.72 (0.03)	0.61 (0.02)	0.75 (0.02)	0.66 (0.02)
Back	0.83 (0.02)	0.70 (0.02)	0.86 (0.02)	0.75 (0.03)
Hip	0.80 (0.02)	0.69 (0.03)	0.85 (0.02)	0.73 (0.02)

Table 5.6: Conversion factors, $C_{P\to O}^{L}$, for ^{137}Cs ground contamination for four organs: colon, thyroid, breast and RBM. Bracketed values denote one standard uncertainty (CONFIDENCE Deliverable 9.10, Mafodda et al., 2019b).

	Conversion Factor, $C_{P\to O}^{L}$ (Gy/Gy) for ^{131}I			
Location, L	*Colon*	*Thyroid*	*Breast*	*RBM*
Chest	0.91 (0.02)	0.76 (0.02)	0.94 (0.02)	0.82 (0.02)
Leg	0.68 (0.02)	0.57 (0.03)	0.71 (0.02)	0.61 (0.02)
Back	0.77 (0.03)	0.65 (0.02)	0.80 (0.02)	0.69 (0.02)
Hip	0.77 (0.02)	0.59 (0.02)	0.81 (0.02)	0.68 (0.03)

Table 5.7: Conversion factors, $C_{P\to O}^{L}$, for ^{131}I ground contamination for four organs: colon, thyroid, breast and RBM. Bracketed values denote one standard uncertainty (CONFIDENCE Deliverable 9.10, Mafodda et al., 2019b).

	Conversion Factor, $C_{P\rightarrow O}^{L}$ (Gy/Gy) for ^{147}Nd			
Location, L	*Colon*	*Thyroid*	*Breast*	*RBM*
Chest	0.80 (0.02)	0.67 (0.03)	0.80 (0.02)	0.70 (0.02)
Leg	0.60 (0.03)	0.51 (0.02)	0.61 (0.02)	0.53 (0.02)
Back	0.69 (0.02)	0.58 (0.03)	0.70 (0.02)	0.61 (0.02)
Hip	0.65 (0.02)	0.57 (0.02)	0.69 (0.02)	0.59 (0.02)

Table 5.8: Conversion factors, $C_{P\rightarrow O}^{L}$, for ^{147}Nd ground contamination for four organs: colon, thyroid, breast and RBM. Bracketed values denote one standard uncertainty.

As observed in previous work in which a sophisticated model of a real mobile phone was used (Eakins, 2015), the results confirmed that they were relatively insensitive to the location of the phone. Different attenuations of the photon fields by phone layers (e.g. display glass) do not greatly affect the dosimetry, in cases of radionuclides emitting photons at both high and low energies. Therefore, a simplified geometry to represent the dosimeter seems to be sufficient for the purpose of optimizing the efficiency of the calculations. In this respect, modelling an entire phone with an enlarged target volume as already reported in section 5.3, would already be enough.

6. Conclusions and Outlook

The study presented here, carried out in the framework of the European Project CONFIDENCE, aimed to scientifically contribute to two main research activities related to accidental radiation exposures. The first of these activities deals with the necessity to improve the assessment of the radiological situation following an emergency, by involving the general population in environmental monitoring. Thus, "citizen measurements" might be helpful in reconstructing individualized exposure histories. On the other hand, the reliability of such kind of measurements represents still an open issue, addressed in the present work by exploring one of the most attractive technology for dose rate detection: smartphone applications. In particular, investigations focused on evaluating the performances of two applications, "GammaPix" and "RadioactivityCounter" which allow dose-rate detection with CMOS camera sensors of mobile phones. Within the context of a large-scale accident, other more conventional environmental monitoring strategies are put in place next to citizen measurements. These can be used to identify critically exposed sub-groups of the population, for which a more accurate dose assessment is carried out.
Specifically for such individual dose assessments, the second research activity of this study focused on developing a retrospective dosimetry method.
Considering that people are not equipped with proper devices for ionising radiation monitoring, the method dealt with using personal items, such as mobile phone, as fortuitous dosimeters. In this sense, not only large-scale accidents scenarios are addressed, but measurements might also be applied in case of any type of unplanned exposures involving people carrying a mobile phone. The usability of mobile phones as dosimeter is based on the fact that electronic components placed on the circuit boards contain alumina substrates sensitive to ionising radiation. Hence, the new measurement protocol developed in this thesis targeted Surface Mount Resistors (SMRs) as dosimeters using for the first time the red Thermoluminescence emission. As a last step, the measured doses in these resistors were correlated to organ absorbed doses by simulating sets of conversion factors with the general purpose Monte Carlo radiation transport code MCNP6.2. The following sections summarize the conclusions and future perspectives for both research tasks of the thesis.

6.1 Environmental monitoring with smartphone applications

Two applications were tested, “GammaPix” and “RadioactivityCounter”, which enable the CMOS camera sensors of smartphones to detect ionising radiation when shielded with adhesive black tape. Both of the apps were downloaded and installed on 14 different smartphone models chosen among the most common brands sold in 2017 covering the low, medium and high price range. Such approach allowed to explore any variability in sensitivity of the CMOS sensor of the devices. Irradiations of the smartphones were performed with calibrated gamma and X-ray sources. Investigations regarded the assessment of the dose-rate responses, energy dependence and angular response of the CMOS camera sensors. As regarded “GammaPix” application, the missing appropriate calibration values for all the smartphones tested resulted to unreliable dose rate assessments. Therefore, the present work focused on “RadioactivityCounter”. During the investigations on this app, it was quantified how the noise level of the sensors affected the detection at low dose-rates. For smartphones characterized by cameras with noise value less than 10, the trend between measured and given dose-rates was observed to be linear down to 2 μGy h^{-1} when measurement time was increased up to 60 minutes. On such devices, the algorithm for image corrections played a key role on the data processing: if, on one hand, it maintained the proportionality between dose-rates and number of counts, on the other, it affected the values of counts recorded. In particular, the true radiation events were replaced with zero values leading to skewed distribution of counts. Smartphones characterized by a *n* value above ten, resulted to be blind below the threshold of 20–50 μGy h^{-1}. For this category of devices, increasing the integration time up to one hour did not improve their performance at low dose rates. The investigation on the background assessment in a shielded environment lead to the conclusion that, regardless of the models, “RadioactivityCounter” did not improve its performance at measuring low dose rates.

The energy dependence study showed that models involving the same kind of sensor show a similar energy dependence and that an over response of a factor between 7 and 12 at photon energies of around 60 keV was generally observed. Fluctuations in the counts detected at different photon incident angles were found to be at most 10%, in line with previous studies.

Based on the results presented in this work, reliable measurements at level of natural radioactivity are difficult to detect with most of the smartphones tested, whereas higher levels of contamination can potentially be assessed. Future investigations on how the environmental temperature might affect the sensor sensitivity are required. People not professionally involved in any official activity of ionising radiation monitoring could follow some minimum criteria for improve the reliability of the measurements, such as: inserting calibration values when they are available (see table 4.1 of the present work), performing a background assessment with a one-hour long detection that may also help to recognize unusual counts (e.g. increasing counts with temperature), and using a minimum integration time of preferably 60 minutes. This study concerned mostly back cameras, since for some of the tested models, the sensors of front cameras showed lower sensitivity in counts. However, this cannot be taken as a general assessment for all the models of smartphones present in the market. In some cases, front cameras might be often associated to sensors larger in sizes and with a lower noise suppression, characteristics that remain to be further investigated. However, more recent models of smartphones are characterized by frontal sides completely covered by glass display. Therefore, future investigations on frontal CMOS sensors should take into account eventual contributions from stray light and multiple reflections.

6.2 Retrospective dosimetry with RTL for lower doses measurements

The present work also aimed to develop a new retrospective dosimetry method based on Red Thermoluminescence (RTL) from surface-mounted resistors of mobile phones. Such electronic components are characterized by a strong luminescence emission due to Cr^{3+} that allowed to carry out dose measurements at a single resistor level. The new measurement protocol was established starting from the sample preparation. Resistors were cleaned with propanol for twenty minutes to remove any residuals of soldering mask, then the signals were read out with a maximum temperature of 350°C to reduce sensitivity changes of the material. The whole procedure was assessed in subdued red light conditions to avoid phototransfer from deeper traps. Dose assessment was optimized in the low dose (<100 mGy) range to evaluate the usability of the method in case of a nuclear emergency accident. In fact, during the latter, most of the individuals would be externally exposed to approximately low doses. The approach of using a single resistor with the goal of reconstructing low doses required the investigation of possible sources of uncertainties

affecting the precision of the method. One type of uncertainty is introduced by the existence of a native signal in unexposed samples which is translated into an apparent dose, the so-called zero dose, by the calibration procedure. Native signals had also been identified in previous studies using the blue TL from alumina substrates. Thus, a systematic evaluation of zero doses was performed on a total of 38 samples extracted from circuit boards of different mobile phones: three samples showed a strong signal (up to hundreds of mGy), whereas all others were statistically not distinguishable from the detection limit, assessed at ~10 mGy. The offset time of the built-in beta source of the luminescence reader introduced an additional dose, estimated as an average value of (5.4±2.3) mGy.
The fading rates of the red emission in different samples were calculated from measurements performed on samples stored for different periods of time after irradiation. This resulted in a value for g of 17.54±2.74 which agrees within the given uncertainty with the value obtained from similar experiments using blue TL. The effect of a positive bias on the dose measurement, observed from the non-constant baseline of the PMT of the luminescence reader was reduced by correcting the RTL signals based on a new background assessment. The dose assessment was finally tested in a real case scenario, with intact mobile phones frontally irradiated with a ^{137}Cs gamma source. The RTL retrospective dosimetry method developed here allowed to assess unknown low doses with an uncertainty of 10% few hours after irradiation, and with an uncertainty of 25% one month after irradiation. Limitations of the method arose for recovering the lowest dose of 20 mGy, the signal of which could not be distinguished from the detection limit of the instrument one month after irradiation. Overall the RTL can be considered useful to be part of a multi-technique approach for individual dose assessments in case of unplanned exposures. The experimental work was combined with MCNP simulations in order to develop a method to convert the measured doses in the resistor into organ absorbed doses for real case scenarios of ground contaminated by ^{137}Cs, ^{131}I and ^{147}Nd. A preliminary investigation on the energy dependence of the resistor extracted and of that within the mobile phone aimed to benchmark the experimental results (subsection 4.2.7) and to provide a preliminary background knowledge on possible shielding effects to the results of the subsequent conversion factors calculations. The data in Tables 5.6, 5.7, 5.8 might be applied to translate the absorbed doses in resistors to the absorbed doses to the four most relevant organs of an individual wearing a mobile phone. Thereby an improved dosimetry compared to dose calculations from environmental measurements is provided, which can

be used for more accurate estimates of radiation risk of individuals. As the data in the tables show, lack of knowledge of the exact location of the mobile phone on the individual during exposure would lead to uncertainties of up to several tens of percent in the organ dose estimate, which is small compared to the sometimes order of magnitude uncertainty that was assumed in the dose reconstruction of the population after the Fukushima accident (WHO report, 2012).

References

4037-1, I. (1996). *X and gamma reference radiation for calibrating dosementers and doserate meters and for determining their response as a function of photon energy - Part 1:Radiation characteristics and production method.* International Organization for Standardization (ISO).

4037-3. (1999). *X and gamma reference radiation for calibrating dosemeters and doserate meters and for determining their response as a function of photon energy - Part3.* International Organization for Standardization .

Ademola, J. A., & Woda, C. (2017). Thermoluminescence of electronic components from mobile phones. *Radiation Measurements*, 13-21.

Ainsbury, E. A., Bakhanova, E., Barquinero, J. F., Brai, M., Chumak, V., Correcher, V., . . . Rothkamm, K. (2011). Review of retrospective dosimetry techniques for external ionising radiation exposure. *Radiation Protection Dosimetry*, 573–592.

Ainsbury, L., Samaga, D., Della Monaca, S., Marrale, M., Bassinet, C., Burbudge, C., . . . Trompier, F. (2017). Uncertainty on radiation doses estimated by biological and retrospective physical methods. *Radiation Protection Dosimetry*, 1-23.

Alessandri, S. (2017). In the Field Feasibility of a Simple Method to Check for Radioactivity in Commodities and in the Environment. *PLOS Curr. Disasters.*

Bailiff, I., Sholom, S., & McKeever, S. (2016). Retrospective and Emergency Dosimetry in Response to Radiological Incidents and Nuclear Mass-Casualty Events: A Review. *Radiation measurements*, 83-139.

Bassinet, C., Trompier, F., & Clairand, I. (2010). Radiation accident dosimetry on electronic components by OSL. *Health Physics, 98*, 440–445.

Bassinet, C., Woda, C., Bortolin, E., Della Monaca, S., Fattibene, P., Quattrini, M., . . . Martini, M. (2014). Retrospective radiation dosimetry using OSL of electronic. *Radiation Measurements*, 475-479.

Bassinet, C., Woda, C., Bortolin, E., Della Monaca, S., Fattibene, P., Quattrini, M., . . . McKeever, S. (2014). Radiation accident dosimetry: TL properties of mobile phone screen glass. *Radiation Measurements*, 461-465.

Beerten, K., Woda, C., & Vanhavere, F. (2009). Thermoluminescence dosimetry of electronic components from personal objects. *Radiation Measurements*, 620-625.

Bos, A. (2007). Theory of Thermoluminescence. *Radiation Measurements*, 45-56.

Bossin, L. (2019). New fortuitous materials for luminescence materials dosimetry following radiological emergencies.

Bøtter-Jensen, L., & McKeever, S. W. (1996). Optically stimulated luminescence dosimetry using natural and synthetic materials. *Radiation Protection Dosimetry*, 273-280.

Brown, A., Franken, P., Bonner, S., Dolezal, N., & Moross, J. (2016). Safecast: successful citizen-science for radiation measurement and communication after Fukushima. *Journal of Radiological Protection*, 82-101.

Carter, L., & Cashwell, E. (1975). Particle-Transport simulation with Monte Carlo method . *Technical information center - U.S. Energy Research and Development Administration*.

Cervone, G., & Hultquist, C. (2018). Calibration of Safecast dose rate measurements. . *Environ. Radioact.*, 51-65.

Chouinard, J. (2015). *The Fundamentals of Camera and Image Sensor Technology*. Tratto da Baumer Ltd.

Cogliati, J., Derr, K., & Wharton, J. (2014). Using CMOS Sensors in a Cellphone for Gamma Detection and Classification. *arXiv:1401.0766*.

Coletti, M., Hultquist, C., & Kennedy, W. G. (2017). Validating Safecast data by comparisons to a U. S. Department of Energy Fukushima Prefecture aerial survey. *J. Environ. Radioact.*, 9-20.

Colin, J. (2017). *Listing of Available ACE Data Tables-Formerly Appendix G of the MCNP Manual* . Los Alamos National Laboratory.

Daniels, F., Boyd, C., & Saunders, D. (1953). Thermoluminescence as a research tool. *Science*, 343-349.

Discher, M., Greiter, M., & Woda, C. (2014). Photon energy dependence and angular response of glass display used in mobile phones for accident dosimetry. *Radiation Measurements* , 471-474.

Discher, M., Hiller, M., & Woda, C. (2015). MCNP simulations of a glass display used in a mobile phone as an accident dosimeter. *Radiation Measurements*, 21-28.

Drukier, G., Rubenstein, E., Solomon, P., Wójtowicz, M., & Serio, M. (2011). Low cost, pervasive detection of radiation threats. *IEEE International Conference on Technologies for Homeland Security (HST)*, (p. 365-371).

Dürr, C. (2011). *Charakterisierung der Photonenenergieabhängigkeit elektronischer Bauteile in Mobiltelefonen hinsichtlich deren Nutzung als Notfalldosimeter.* Bachelor thesis.

Eakins, J., & Koroukla, E. (2015). Luminescence-based retrospective dosimetry using Al2O3 from mobile phones: a simulation approach to determine the effects of position. *J.Radiol.Prot.*, 343-381.

Eckerman, K. (1993). *External exposure to radionuclides in air, water, and soil.* ORNL Report EPA-402-R-93-081.

Ekendahl, D., & Judas, L. (2012). Retrospective dosimetry with alumina substrate from electronic components. *Radiation Protection Dosimetry*, 134-141.

Enterprises, E. (2014). *Photomultiplier 9235B series data sheet*. Tratto da http://my.et-enterprises.com/pdf/9235B.pdf; abgerufen am 12.11.2014.

Fiedler, I., & Woda, C. (2011). Thermoluminescence of chip inductors from mobile phones for retrospective and. *Radiation Measurements*, 1862-1865.

Gasparian, J., Vanavhere, F., & Yukihara, E. (2012). Evaluating the influence of experimental conditions on the photon energy response of Al2O3:C optically stimulated luminescence detectors. *Radiation Measurements*, 243-249.

Godfrey-Smith, D. I., & Haskell, E. H. (1993). Application of optically stimulated luminescence to the dosimetry of recent radiation events monitoring low total absorbed dose. *Health Physics*, 396-404.

Greiter, M. B., Denk, J., & Hoedlmoser, H. (2016). Secondary standard calibration, measurement and irradiation capabilities of the individual monitoring service at the Helmholtz Zentrum Munchen: aspects of uncertainty and automation. *Radiation Protection Dosimetry*, 1-5.

Gröber, S., & al., e. (2014). Using smartphones and tablet PCs for β-spectroscopy in an educational experimental setup. *European Journal of Physics*.

Guidance, R. S. (2018). *Iodine-131.* University of Michigan.

Hashizume, T., Maruyama, T., Shiragai, A., Tanaka, E., Izawa, M., Kawamura, S., & Nagaoka, S. (1967). Estimation of the air dose from the atomic bombs in Hiroshima and Nagasaki. *Hlth Phys*, 149-161.

Haskell, E. (1993). Accident dosimetry using environmental materials: the role of Thermoluminescence. *Radiation Measurements*, 87-93.

Higashimura, T., Ichikawa, Y., & Tunahiko, S. (1963). Dosimetry of Atomic Bomb Radiation in Hiroshima by Thermoluminescence of Roof Tiles. *Science*, 1284-1285.

Hiller, M., Woda, C., Bougrov, N., Degteva, M., Ivanov, O., & Ulanovsky, A. (2017). External dose reconstruction for the former village of Metlino (Techa River, Russia) based on environmental surveys, luminescence measurements and radiation transport modelling. . *Radiat. Environ. Biophys.*, 139-159.

Holgersson, S., Steenari, B., Björkman, M., & Cullbrand, K. (2017). Analysis of the metal content of small-size Waste Electric and Electronic Equipment (WEEE) printed circuit boards—part 1: Internet Internetrouters, mobile phones and smartphones. *Resources, Conservation and Recycling*.

Huntley, D., & Lamothe, M. (2001). Ubiquity of anomalous fading in K feldspars and the measurement and correction for it in optical dating. *Canadian Journal of Earth Sciences*, 1093-1106.

IAEA. (2017). *Operational intervention levels for reactor emergencies and methodology for their derivation.* IAEA Report - EPR-NPP-OILs.

Ichikawa, Y., Higashimura, T., & Shidei, T. (1966). Thermoluminescence dosimetry of gamma rays from atomic bombs in Hiroshima and Nagasaki. *Hlth Phys.*, 395-405.

ICRP. (2010). *Conversion Coefficients for Radiological Protection Quantities for External Radiation Exposures.* International Commission on Radiological Protection.

ICRU. (1984). *Stopping powers for electrons and positrons - Report 37.* International Commission on Radiation Units and Measurements.

ICRU. (2002). *Retrospective assessment of exposure to ionising radiation-Report 68.* International Commission on Radiation Units and Measurements.

ICRU. (2019). *Methods for Initial-Phase Assessment of Individual Doses Following Acute Exposures to Ionizing Radiation - Report 94.* International Commission on Radiation Units and Measurements.

Inrig, E., Godfrey-Smith, D., & Khannaa, S. (2008). Optically stimulated luminescence of electronic components for forensic,. *Radiation Measurements*, 726 – 730.

Jacob, P., Goksu, Y., Taranenko, V., Meckbach, R., Bougrov, N., Degteva, M., & Vorobiova, M. (2003). On an evaluation of external dose values in the Techa River Dosimetry System (TRDS) 2000. . *Radiat. Environ. Biophys.*, 169–174.

Jain, M., Bøtter-Jensen, L., & Thomsen, K. (2007). High local ionization density effects in X-ray excitations deduced from optical stimulation of trapped charge in Al2O3. *J. Phys.: Condens. Matter.*

Kalchgruber, R., Göksu, H., Hochhäuser, E., & Wagner, G. (2002). Monitoring environmental dose rate using Risø TL/OSL readers with built-in sources: recommendations for users. *Radiation Measurements 35*, 585-590.

Kim, M., Kim, H., Han, H., Lee, J., Lee, S., Chang, I., . . . Kim, C. (2019). A study on dose conversion from a material to human body using mesh phantom for retrospective dosimetry. *Radiation Measurements*, 106-126.

Kittel, C. (2013). *Introduction to Solid State Physics. 8th Edition.* Hoboken, New Jersey: John Wiley & Sons.

Koroukla, E. (2015). *Luminescence dosimetry with ceramic materials for application to radiological emergencies and other incidents.* Doctoral Thesis, Durham University.

Kusuma, H. H., Astuti, B., & Ibrahim, Z. (2019). Absorption and emission properties of ruby (Cr:Al2O3) single crystal. *J. Phys.: Conf. Ser. 1170 012054*.

Lee, J., Chang, I., Kim, J., Pradhan, A., Kim, B., & Chung, K. (2016). Dose re-estimation using thermoluminescence of chip inductors and resistors following the dose estimation by using optically stimulated luminescence readout for retrospective accident dosimetry. *Radiation Measurements*, 257-261.

Lee, J., Kim, H., Kim, J., Pradhan, A., Kim, M., Chang, I., . . . Chung, K. (2017). Thermoluminescence of chip inductors and resistors in new generation mobile phones for retrospective accident dosimetry. *Radiation Measurements*, 1-7.

Li, S. (1993). *Energy Band Theory in Semiconductor Physical Electronics.* Boston: Springer.

Mafodda, A., & Woda, C. (2020). External dose-rate measurements based on smartphone CMOS sensors. *Radiation Measurements 137*.

Mafodda, A., Woda, C., & Eakins, J. (2019b). *Deliverable 9.10 - Paper on external dosimetry using personal objects.*

Mafodda, A., Woda, C., & Rühm, W. (2019a). *Deliverable 9.8 - Database of smartphone app / dosimeter evaluation.*

Maruyama, T., Kumamoto, Y., Y., I., Nagatomo, T., Hoshi, M., E., H., & P., K. (1987). Thermolu-minescence measurements of gamma rays (Edited by Roesch W.). U.S.-Japan Joint Reassessment of Atomic Bomb Radiation Dosimetry in Hiroshima and Nagasaki, Final Report. *Radiation Effects Research Foundation,*.

McKeever, S. &. (1997). Luminescence Models. *Radiation Measurements*, 625-661.

McKeever, S. (1985). *Thermoluminescence of solids.* Cambridge: Cambridge University Press.

McKeever, S., & Moscovitch, M. (2003). On the advantages and disadvantages of optically stimulated luminescence dosimetry and thermoluminescence dosimetry. *Radiation Protection Dosimetry*, 263-270.

McKeever, S., Moscovitch, M., & Townsend, P. (1995). *Thermoluminescence dosimetry materials: properties and uses.* Kent (England): Nuclear technology Publishing.

Michelsburg, M., Fehrenbach, T., & Leòn, F. (2012). Measuring ionizing radiation with a mobile device. *SPIE 8304, Multimedia on Mobile Devices and Multimedia Content Access: Algorithms and Systems VI*.

Murty, R. (1965). Effective Atomic Numbers of Heterogeneous Materials. *Nature*, 398–399.

Petoussi-Henss, N., Schlattl, H., Zankl, M., Endo, A., & Saito, K. (2012). Organ doses from environmental exposures calculated using voxel phantoms of adults and children. *Phys. Med. Biol. 57*, 5679-5713.

Poludniowski, G. L. (2009). SpekCalc: a program to calculate photon spectra from tungsten anode x-ray tubes. *Phys. Med. Biol. 54*, 433-438.

Pradhan, A. S., Lee, J. I., & Kim, J. L. (2008). Recent developments of optically stimulated luminescence materials and techniques for radiation dosimetry and clinical applications. *Journal of Medical Physics*, 85-99.

Press, W., Teukolsky, S., Vetterling, W., & Flannery, B. (2002). *Numerical Recipes in C.* Cambridge Univeristy Press.

RadiologicalSafetyGuidance. (2018). *Iodine-131.* Department of Environment, Health and Safety, Univerity of Michigan.

Randall, J., & Wilkins, M. H. (1945). Phosphorescence and electron traps - The study of trap distributions. *Proc.Roy.Soc.Lond.*, 365-389.

Richter, D., & al., e. (2012). A novel beta source design for uniform irradiation in dosimetric applications. *Ancient TL*, 57-64.

Richter, D., Richter, A., & Dornich, K. (2013). Lexsyg - A new system for luminescence research. *Geochronometria*, 220-228.

Salvat, F., Fernández-Varea, J., Acosta, E., & Sempau, J. (2001). *PENELOPE A Code System for Monte Carlo Simulation of Electron and Photon Transport.* Issy-les-Moulineaux - France: NUCLEAR ENERGY AGENCY ORGANISATION FOR ECONOMIC CO-OPERATION AND DEVELOPMENT.

Tith, S., & Chankow, N. (2016). Measurement of Gamma-Rays Using Smartphones. *Open Journal of Applied Sciences*, 31-37.

Van Hoey, O., Salavrakos, A., Marques, A., Nagao, A., Willems, R., & Vanhavere, F. (2016). Radiation dosimetry properties of smartphone CMOS sensors. *Radiation Protection Dosimetry*, 314–321.

Wagner, E., Sorom, R., & Wiles, L. (2016). Radiation monitoring for the masses. *Health Physics*, 37-44.

Waller, E., & Van Maanen, J. (2015). The role of the Health Physicist in nuclear safety. *Health. Phys.*, 468-476.

Werner, C. (2017). *MCNP's user manual - version 6.2.* Los Alamos National Laboratory (LANL): LA-UR-17-29981.

Werner, C. J. (2017). *MCNP® USER'S MANUAL.* Los Alamos.

WHO. (2012). *Preliminary dose estimation from the nuclear accident after the 2011 Great East Japan earthquake and tsunami.* World Health Organization.

Woda, C., & al., e. (2009). On the use of OSL of wire-bond chip card modules for retrospective and accident dosimetry. *Radiation Measurements*, 548-553.

Woda, C., & Spöttl, T. (2009). On the use of OSL of wire-bond chip card modules for treatment of electronic components from electronic devices. *Radiation Measurement 44*, 548-553.

Woda, C., Fiedler, I., & Spöttl, T. (2012). On the use of OSL on chip cards modules with molding for retrospective and accident dosimetry. *Radiation Measurement*, 1068-1073.

Woda, C., Fiedler, I., Urso, L., & Kaiser, J. (2011). *Retrospective Dosimetry for the population in emergency situation-final report.* Helmholtz Zentrum München - Deutsches Forschungszentrum für Gesundheit und Umwelt, Institut für Strahlenschutz, Arbeitsgruppe Radioökologische Modellierung und Retrospektive Dosimetrie.

Woda, C., Hiller, M., Ulanowski, A., Bugrov, N., Degteva, M., Ivanov, O., . . . Shinonaga, T. (2020). Luminescence dosimetry for evaluation of the external exposure in Metlino, upper Techa River valley, due to the shore of the Metlinsky Pond: A feasibility study. *Journal of Environmental Radioactivity*, 214-215.

Yamane, L., Tavares de Moraes, V., Crocce Romano Espinosa, D., & Tenório, J. (2011). Recycling of WEEE: Characterization of spent printed circuit boards. *Waste Management*, 2553-2558.

Yukihara, E., & McKeever, S. (2011). *Optically Stimulated Luminescence. Fundamentals and Applications.* Chischester: John Wiley & Sons Ltd.

Zhi-Young, H., Sheng-Hua, L., & Man-Yin, W. (2000). Effects of annealing on TL sensitivity of granitic quartz. *Radiation Measurements*, 227-231.

Appendix A

List of Materials used in MCNP simulations

Volume N.	Material	Density (g/cm^3)	Reference
1	Ceramic core: Al2O3 (96%), SiO2 (3%), MgO (1%)	3.75	Bourns data sheet chip resistor CRT0402 (2006)
2	Nickel cap	8.9	
3	Tin cap	7.310	
4	Resistive layer: Nichrome Ni (80%) and Cr (20%)	8.4	https://www.chemistrylearner.com/ni-chrome.html
5	Epoxy Resin type 29690-82-2 (C7H8O.C3H5ClO.CH2O)	0.97	https://www.chemsrc.com/en/cas/29690-82-2_585908.html
6	Dry air	0.001205	Hubbel and Seltzer (2004)

Table A.1: Description of the materials, their densities and corresponding references, used in the simulation of the extracted chip resistor. The numbering of the volumes refers to Figure 5.2.

Volume N.	Material	Density (g/cm^3)	Reference
1	Display Glass	2.54	Valleydesign data sheet 1737F (2013)
2 and 9	Plastic case: Polyamide (PA6)	1.13	Flemming et al. (1995)
3, 6 and 8	Aluminum layer	2.699	
4	Printed Circuit Board (PCB): Glasfibers (45%), Resin (45%), Copper Foil (10%)	1.8	ISOLA Datasheet IS410 laminate (2010)
7	Battery: LiCoO2	4.9	Umicore data sheet LiCoO2 (2012)
5	Ceramic core: Al2O3 (92%), SiO2(3%), MgO (1%), Cr (4%)	3.75	Bourns data sheet chip resistor CRT0402 (2006) enriched with Cr 4%
5	Nickel cap	8.9	

	Tin cap	7.310	
	Resistive layer: Nichrome Ni(80%) and Cr (20%)	8.4	https://www.chemistrylearner.com/ni-chrome.html
	Epoxy Resin type 29690-82-2 (C7H8O.C3H5ClO.CH2O)	0.97	https://www.chemsrc.com/en/cas/29690-82-2_585908.html

Table A.2: Description of the materials, their densities and the corresponding references, used in the simulation of the NOKIA 6300. The numbering of the volumes refers to Figure 5.4.

Volume N.	Material	Density (g/cm^3)	Reference
1	Outer touch screen plexiglass	1.19	Discher et al. (2015)
2	Inner display glass	2.54	Valleydesign data sheet 1737F (2013)
3	Indium-Tin-Oxide ITO: In2O3 (90%) SnO2 (10%)	7.14	Park et al. (2001); Umicore data sheet indium tin oxide ITO (2011)
4	Printed Circuit Board (PCB)	4.7	Holgersson et al. (2017)
5	TLD-500: Al2O3	3.72	Eakins et al. (2015)
6	Battery: LiCoO2	4.9	Umicore data sheet LiCoO2 (2012)
7	Plastic case: Polyamide (PA6)	1.13	Flemming et al. (1995)

Table A.3: Description of the materials, their densities and the corresponding references, used in the simulation of the NOKIA1. The numbering of the volumes refers to Figure 5.9.

Appendix B

Electron Probe Microanalysis (EPMA)

EPMA analysis is based on bombarding a micro-volume (typically 10-30 μm^3 or less) of a sample with a focused electron beam, which for this work was set at an accelerating voltage of 15 kV. Then the characteristic X-ray photons thereby emitted by the various elements in the sample are detected, and the sample composition can be identified with a Wavelength Dispersive Spectrometer (WDS). The EPMA technique was chosen because it allows qualitative and quantitative elemental analysis, in a non-destructive way and with sensitivity at the level of ppm. For the present work, resistors were embedded in epoxy with the ceramic bulk facing upwards, and EPMA measurements were performed on sample volumes of ~10 μm^3 size. Next to the results presented in chapter 5, the following trace elements were measured (further information in brackets: X-ray line, standard, diffraction crystal): Ca (Kα, wollastonite, LPET), Mg (Kα, periclase, TAP), Si (Kα, wollastonite, TAP), Cr (Kα, synthetic Cr_2O_3, LIF and LLIF).

Uncertainties analysis for RTL measurements

In Thermoluminescence, the TL intensity used to estimate the corresponding dose is determined by measuring the number of photons emitted from a sample with a photomultiplier tube (PM tube) operating in photon-counting mode. When sufficient counts are registered, the distribution of luminescence signals are assumed to follow the Poisson distribution for uncorrelated random events. A characteristic of the Poisson distribution is that the standard deviation of the distribution, σ, is equal to the square root of the number of observations $\sqrt{N}$ within a given time interval. In the case of a routine luminescence measurement N is the number of photon counts per detection channel. Therefore the uncertainty attributed to the TL intensity from a single measurement is given by:

$$I_{err} = \sqrt{N + \sigma_{DC}^2} = \sqrt{I_{TL} + \sigma_{DC}^2}$$

Where N is calculated from the luminescent signal counts and equals the TL intensity, while σ_{DC} is the standard deviation of the distribution of the dark counts of the PMT, which approximately follows a Gaussian distribution. The dark counts are the intrinsic detector background in absence of any light sources. The unknown dose from a sample is then measured using a calibration curve that correlates the TL signal (on y-axis) and dose (on x-axis).

For the present work, the dose responses is linear, thus the unknown dose D_{TL} associated to the TL intensity is given by:

$$D_{TL} = \frac{I_{TL} - a}{b}$$

Where a is the slope and b represents the y-axis intercept of the calibration curve. The uncertainty on the recovered dose is assessed from the error propagation of the uncertainty in the TL signal (I_{err}), of the linear fit parameters (σ_a, σ_b) and on their covariance ($\mathrm{cov}_{a,b}$):

$$D_{TL,err} = \sqrt{\left(\frac{I_{err}}{b}\right)^2 + \left(\frac{\sigma_a}{b}\right)^2 + \left(\frac{(I_{TL} - a) \cdot \sigma_b}{b^2}\right)^2 + 2 \cdot \left(\frac{I_{TL} - a}{b^3}\right)^2 cov_{a,b}}$$

The linear fit can be weighted or unweighted. Weighted fits are calculated by minimizing the chi-square merit function (Press et al., 2002):

$$\chi^2(a,b) = \sum_{i=1}^{N} \left(\frac{y_i - a - bx_i}{\sigma_i}\right)^2$$

Where the uncertainty σ_i associated to each measurement y_i is known as weight. In this case, $\sigma_i = I_{err}$ calculated as above, are assumed to be normally distributed and the degree of scatter of data points around the fitted straight line is explained by the individual errors. Sometimes this is not the case in retrospective dosimetry and the scatter is larger than the errors indicate. Thus, the uncertainty in the parameters of the calibration curve might be underestimated. As an alternative, an unweighted linear fit can be carried out. The individual errors are not considered but an error common to all data points is used. The latter is calculated from the scatter of the data points according to:

$$\sigma_i = \sqrt{\frac{\chi^2}{N-2}}$$

This uncertainty is then used to calculate the uncertainty in the obtained fit parameters. To be conservative, the data analysis employed in this work relied on always considering the larger of the two.

The final corrected dose $D_{TL,C}$ assessed is then given by:

$$D_{TL,C} = \frac{D_{TL}}{F} + D_{offset}$$

Where:

- D_{TL} is characterized by the error calculated as above;
- D_{offset} is the dose due to the offset time of the beta source assessed in section 4.2.1 and for which the standard deviation was assessed as 2.4 mGy;
- the fading factor F, calculated as in section 4.2.4 , is characterized by the following uncertainty: if we assume normally distributed uncertainties in κ, t_{acc} and t_{cal}, then:

$$\sigma_f^2 = \frac{1}{\left(1 - \kappa \ln\left(\frac{t_{cal}}{t_C}\right)\right)^4}\left[\left(\ln\left(\frac{t_{acc}}{t_{cal}}\right)\right)^2 \sigma_\kappa^2 + \left(\frac{\kappa}{t_{acc}}\left(1 - \kappa \ln\left(\frac{t_{cal}}{t_C}\right)\right)\right)^2 \sigma_{t_{acc}}^2 + \left(\frac{\kappa}{t_{cal}}\left(1 - \kappa \ln\left(\frac{t_{acc}}{t_C}\right)\right)\right)^2 \sigma_{t_{cal}}^2\right]$$

If $\sigma_{t_{acc}}$ and $\sigma_{t_{cal}}$ are equal to 0, then:

$$\sigma_F^2 = \left(1 - \kappa \ln\left(\frac{t_{cal}}{t_C}\right)\right)^{-4}\left[\left(ln\left(\frac{t_{acc}}{t_{cal}}\right)\right)^2 \sigma_\kappa^2\right]$$

Then, the uncertainty calculated in the final corrected dose is given by the error propagation:

$$D_{TL,C,err} = \sqrt{\left(\frac{1}{F}\right)^2 {D_{TL,err}}^2 + \left(\frac{D_{TL}}{F^2}\right)^2 2\sigma_f^2 + \sigma_{offset}^2}$$

List of own publications

- **Mafodda, A**., Woda, C., External dose-rate measurements based on smartphone CMOS sensors, Radiation Measurements 137, 2020.

- Bleher, M., Gering, F., Stöhlker, U., Karhunen, T., Nalbandyan-Schwarz, A., Woda, C., **Mafodda, A.**, Reduction of uncertainties in exposure assessment based on environmental monitoring data, Radioprotection 55,81-88, 2020.

- López, M.A., Berkovskyy, V., Ratia, G., Challeton-de-Vathaire, C., Davesne, E., Eakins, J., Franck, D., Giussani, A., Gregoratto, D., Hernandez, C., Kulka, U., **Mafodda, A**., Marsh, J.W., Navarro, J.F., Oestreicher, U., Pérez, B., Sierraand, I., Woda, C. Improvements in individual dose measurement techniques following nuclear emergencies, Radioprotection 55, 89-93, 2020

- Lead Author of CONFIDENCE Deliverable 9.8 „Database of smartphone app / dosimeter evaluation", 2019

- Lead Author of CONFIDENCE Deliverable 9.10 „ Paper on external dosimetry using personal objects", 2019

List of scientific contributions

- Oct. 2018. Oral presentation at the Young Scientists Session in ERPW 2018 - Rovinji (Croatia)
- Nov. 2018. Oral presentation at the CONFIDENCE Work Package 2 Meeting in München (Germany)
- Feb. 2019. Oral report at EURADOS AM2019 - Łódź (Poland)
- Sep. 2019. Oral presentation awarded with the ***"Young Scientist Award"*** at the 19th International Conference on Solid State Dosimetry (SSD19) - Hiroshima (Japan)
- Dic. 2019. Poster session with two posters ("Evaluation of apps for dose-rate measurements using the camera sensor of the smartphone" and "External dosimetry using personal items") at the CONFIDENCE Final Dissemination Workshop – Bratislava (Slovak Republic)
- Next May 2022. Cited as first author in a poster that will be presented at the 17th European Workshop on Modern Developments and Applications in Microbeam analysis (EMAS 2022)

Acknowledgements

The professional and personal achievement enclosed in these hundred (and more) pages would have not been possible without the precious support of several people.

First of all, thanks to my Doktorvater Prof.Dr. Rühm for the scientific hints, the endless availability, the remarkable commitment to students, and the much-appreciated encouragements.

A special thanks to Clemens, in these past three years more than just a direct advisor: Physics teacher in the lab, English teacher outside the lab, great companion when travelling together, motivator in the toughest times (approaching deadlines!), dispenser of advices and suggestions. The milestone I reach today is mainly due to your special support.

Thanks to Paola Fattibene, my external supervisor, role model as a successful (Italian!) woman in science. Grazie di cuore.

A big thanks to Jon Eakins (PHE) and his kind help for the MCNP simulations section and the voxel phantom geometry.

I am thankful to Dr. Dirk Müller from the Department for Earth and Environmental Sciences - Section for Mineralogy, Petrology and Geochemistry (LMU München) for his accurate work on the EPMA analysis on the resistors.

Despite all the institutional changes of the last couple of years, my PhD will always be linked to the Arbeitsgruppe ISAR. I am thankful I had the chance to share my "journey" with you Liebe Kollege und Liebe Kollegin, building good memories and collecting unforgettable experiences, from the Christmas Choir to the Betriebsausflug up to the Herzogstand!

Thanks to the colleagues become more than just colleagues, who showed sincere friendship especially during the toughest times of the scientific research: Noemi and Marco.

Thanks to all the researchers, students, professors, met during the all the conferences and workshops I had the honor to attend within the CONFIDENCE framework.

You all made me grow up both as a person and as a scientist.

All the trips around Europe, as well as the amazing one to Japan in 2019, will always be remembered as the best times of my PhD!

Huge thank to my group of friends here in Munich, who made/keep making my life as expat much easier and enjoyable: Mari, Frau Bechi, Annalina, Klemens, Lorenza, Matteo.

To my amazing sister Roberta, being there for me since more than 20 years.

No distance can keep us apart, and no life goals would be the same without your precious friendship. Ti voglio bene!

Getting a PhD title is nothing compared to my biggest success in life: my family.
The bonding with my father, mother and brother knows no kilometers, no boundaries, no different countries or habits, and will always be the reason why I hold on. No matter what. Hope I made you proud. Vi voglio bene!
To my love and future husband, who holds my hand every time we jump into a new adventure, as we did three years ago. Our brightest one is still yet to come.

The research leading to these results was carried out within CONFIDENCE project that is part of the umbrella structure of CONCERT. This project has received funding from the Euratom research and training programme 2014–2018 under grant agreement No. 662287.

Affidavit

Affidavit

Mafodda, Alessia

Surname, first name

I hereby declare, that the submitted thesis entitled:

„Retrospective dosimetry with luminescence measurements on personal items for unplanned exposures“

……

is my own work. I have only used the sources indicated and have not made unauthorized use of services of a third party. Where the work of others has been quoted or reproduced, the source is always given.

I further declare that the submitted thesis or parts thereof have not been presented as part of an examination degree to any other university.

München, 11.07.2022

place, date

Alessia Mafodda

Signature doctoral candidate